Predictive Sensor Analytics for Power Side-Channel Monitoring of Security Applications in Fused Deposition Modeling

by

Md Shahriar Aziz

A Dissertation submitted to the Graduate Faculty of
Auburn University
in partial fulfillment of the
requirements for the Degree of
Doctor of Philosophy

Auburn, Alabama
August 3, 2024

Keywords: Additive manufacturing, Side-channel monitoring, Fused Deposition Modeling

Approved by

Dr. Gregory Purdy, Chair, Assistant Professor of Industrial and Systems Engineering
Dr. Jia (Peter) Liu, Assistant Professor of Industrial and Systems Engineering
Dr. Yadrianna Acosta-Sojo, Assistant Professor of Industrial and Systems Engineering
Dr. Mehdi Sadi, Assistant Professor of Electrical and Computer Engineering
Dr. Mark Hoffman, Associate Professor of Mechanical Engineering

Abstract

The advent of Additive Manufacturing (AM) changed the landscape of the manufacturing industry resulting in new possible designs and products. Around the same time, Industry 4.0 got great attention from the industrial community. Industry 4.0 works across systems connecting machines and different sub-systems and collects and analyzes data to make decisions. This type of interconnected system is considered to be the direction in which the manufacturing world is moving. Thus, it is safe to say that AM will be incorporated into Cyber-Physical Systems (CPS) in some capacity. A CPS consists of three components: a cyber component, a physical component, and a combination of these two components. An increased number of interaction points in the CPS leaves the system vulnerable to attacks, either in terms of intellectual property theft or the system can be sabotaged. Traditional cybersecurity protocols may mitigate the attacks to some extent, but they can not handle the physical component of the system, keeping space for some attacks. In such scenarios, side channels like sound, vibration, and heat may provide certain information regarding the process, irrespective of whether the system is compromised or not.

This work is aimed at analyzing the power side-channel signal in a Fused Deposition Modeling (FDM) process, a type of AM process. The main similarities and differences between a cyber system and CPS and their different strategies are discussed. A method is designed to predict the power signature based on the CAD design. A comparative study of the predicted and actual power signature can provide certain information about the machine and process, including anomaly or sabotage detection.

Acknowledgments

I want to express my sincere gratitude to my advisor, Dr. Gregory Purdy, for his invaluable guidance and support throughout my journey. I could not have come this far without his timely supervision, insightful suggestions, and unwavering assistance. Dr. Purdy's mentorship has not only shaped my academic endeavors but has also contributed significantly to my personal and professional growth. His dedication and expertise have played a critical role in helping me navigate challenges and achieve milestones.

I sincerely thank Dr. Jia (Peter) Liu for his guidance regarding process monitoring with sensors and different analytical approaches. I express my gratitude to Dr. Yadriana Acosta-Sojo for providing feedback on the general research idea. I am thankful to Dr. Mehdi Sadi from the Electrical Engineering department for guiding me with various things related to electrical components. I extend my deepest thanks to Dr. Mark Hoffman for his effort in reading and refining the dissertation manuscript.

I would like to express my sincere gratitude to Dr. Gregory Harris, Chair of the Department of Industrial and System Engineering, Auburn University, and Director of ICAMS, for supporting and funding to conduct the research case studies. I would like to express my gratitude to my research group, which includes Enkai Bi, Madison Evans, Mohammad Mydanchi, and Monir Hossain. They are responsible for promoting a healthy and collaborative work environment in our group.

I express my deepest gratitude to my wife, Mirza Shuhie, for her unwavering support and sacrifices for me throughout my doctoral studies.

Finally, I am grateful to God for sustaining me throughout this study.

Table of Contents

List of Figures

List of Tables

Chapter 1

Introduction

Throughout early human civilization, there was a need to manufacture things for daily use. However, early manufacturing systems were based on craftsmanship and were not focused on interchangeable components. The “American System of Manufacturing” introduced part interchangeability, gradually leading to the assembly line and eventually to the second industrial revolution [1]. The third industrial revolution was marked by semi-automation and made it possible to have an entire production line function without human intervention [2].

The advent and availability of the internet made things even more promising. Eventually, the physical world of manufacturing incorporated cyber components to give rise to cyber-physical systems (CPS) and Industry 4.0. As the name suggests, a cyber-physical system comprises cyber and physical components along with their interaction. Industry 4.0 has become a defining term in various industries over the last few years. High efficiency, optimized logistics, and flexible production are a few driving factors behind the emerging popularity of Industry 4.0. In this case, the whole system is a massive CPS network. Different machines and sub-systems communicate within a network to carry out the required tasks. From ordering to delivery of a finished product, entire supply chain operations can be fulfilled. These interconnected systems can provide higher productivity, better product customization, improved logistics, and more [3].

While traditional manufacturing removes material to obtain the final product, AM does the opposite. This layer-by-layer manufacturing process made designs simple while adding some preferred features. Complex airplane fuel nozzles, human prosthetics, and product prototyping are made much simpler with the help of various AM processes [4]. The ability to make intricate shapes with complex designs gives AM a clear advantage over the conventional subtractive manufacturing processes. As a result, the application of AM expanded manyfold. AM processes are now good enough for a wide selection of materials, including metals and non-metals like plastic and resin. While AM is typically slower compared to traditional manufacturing, it can be quicker and more efficient in prototyping and low-volume production. This ability to cope with design variations makes AM suitable for incorporation with Industry 4.0.

Since additive manufacturing can comply with more custom design options, it is getting elevated exposure. Like any other connected system, additive manufacturing is an interconnected system that is prone to attack from malicious actors. Unlike financial organizations, the security of a CPS system was not prioritized until the event of Stuxnet in 2010 [5]. Often people are unaware of the possibility of being sabotaged by their adversaries. According to former Cisco CEO John Chambers, "There are two types of companies: those who have been hacked, and those who do not yet know they have been hacked" [6]. Thus, it takes a lot of time and resources even to detect that there has been an attack. The compromised system can result in the loss of intellectual property, low-quality products, financial losses, or potentially impact the infrastructure or people involved with the production system.

1.1 Significance

Attacks on a connected system have been there for a long time. A few possible reasons for such attacks are financial, political, goodwill, or maybe actions of disgruntled employees towards the organization [7]. For an extended period, attacks on such a connected system were mainly cyber-attacks. As a result, organizations are aware of cyber attacks and possible attack strategies and are more or less capable of fighting such threats [8]. However, the same can not be said about attacks targeting CPS. A CPS consists of an additional physical component, and there's an interaction between the cyber and physical components. Thus, a general cyber-attack defense system is not directly transferable to the defense of a CPS. Thus, there remain vulnerabilities in the system. The impact of cyber-physical system (CPS) attacks can be significant, often going undetected for a considerable amount of time, which can lead to theft of intellectual property, decreased performance, and various other negative consequences [9]. Users typically rely on process monitoring systems to assess the health of their systems; however, incidents such as Stuxnet have demonstrated that these monitoring systems can also be compromised [5]. As a result, it becomes crucial to implement monitoring techniques that are impervious to compromise. Even if adversaries can infiltrate a system, it is unlikely that they would be able to manipulate side-channel data, such as sound, heat, or the current drawn by actuators.

1.2 Motivation

The event of the Stuxnet malware attack on the Iranian nuclear program alarmed the world about the potential dangers of a cyber-physical attack and is a motivation for this study. The incident of Stuxnet malware surfaced in 2010. The 500-kilobyte virus infected several industrial sites, including a uranium enrichment plant in Iran. The virus gets into the system running the Microsoft Windows operating system through a USB stick and avoids the auto-detect system. Afterward, it checks for particular Siemens hardware. If a suitable host is present, the virus updates through the internet and compromises the system's logic controller. Eventually, it controls the hardware system while providing false feedback to the outside system. The malware was finally detected when the centrifuges had already lost a significant capability [10]. The victim, in this case, is an industrial setup. In 2017, a ransomware named NotPetya alone resulted in a global loss of $10 billion by infecting industrial control systems [11]. The organizations in these cases had some traditional cyber-security measures in their system, but they were not prepared for CPS attacks. In the case of Stuxnet, the malware bypassed the conventional cybersecurity protocol and was activated by the particular hardware. This event indicates that traditional cybersecurity protocol may not be applied with the more complex CPS. Again, in most cases in an industrial setup, people rely heavily on the Supervisory Control and Data Acquisition (SCADA) system. However, it is almost impossible for the attacker to change the sound, vibration, temperature, or other side channels. Thus, side-channel analysis can be a great option in detecting potential CPS attacks. A common system anomaly detection technique usually compares the sample data with known good data. This research aims at using the current side channel to detect a potential attack on the system. The first step in attaining the goal is to be able to simulate a current profile based on the provided G-code, and the resulting profile can be compared to an actual current profile to detect sabotage attacks on the system. G-code is a type of programming language used in additive and subtractive manufacturing to carry out different tasks like tool movement, extruding, bed leveling, etc.

1.3 Research Contributions

The proposed work aims to detect anomalies in FDM manufacturing using the power signal side channel. Unlike previous works, this dissertation aims to detect anomalies based on a predicted base signal rather than an actual signal. Thus, the potential research contributions include:

(1) *Analyzing and characterizing current profiles for straight lines and curves*: This section is dedicated to understanding and simulating current profiles for straight lines and curves based on the G-code of a part.

(2) *Creating a general framework for the current signal generation*: This work is dedicated to simulating how a complete G-code works for the 3-D printer. This section's outcome is to be able to simulate the current profile for any G-code of a part. The case studies for this research are performed on a Lulzbot Taz 6 printer, but the ideas can be transferred to other systems.

(3) *Study of the deviation in current signal based on part complexity*: This contribution is dedicated towards the study of deviation in current signal based on part complexity. Both the number of features and feature complexity are addressed in this section.

1.4 Dissertation Outline

The dissertation is structured as follows. Chapter 2 provides background information on CPS, AM, the FDM process, process monitoring in the FDM process, and security-related works. Chapter 3 discusses the test bed, including the working principles of the particular 3D printer used, along with some properties of the components. Chapter 4 discusses and simulates current profiles for straight lines and curvatures. Chapter 5 builds on the previous chapter to create a framework to simulate current profiles for objects with complex geometries and includes a case study. Chapter 6 is dedicated to studying the deviation of the signal based on part complexity. Finally, Chapter 7 includes the conclusions and future work.

Chapter 2

Background and Literature Review

A cyber-physical system consists of a cyber component, a physical component, and the interaction between them. In the context of Industry 4.0, AM can be a significant part of a CPS. This section discusses background information regarding CPS, Additive Manufacturing, the FDM process, and the security perspective of all these areas.

2.1 Cyber-Physical System

CPS enables the communication between physical reality and the cyber world [12]. One such system usually consists of multiple components. In recent times, more CPSs have been integrated into industries due to their ability to make systems more responsive and interconnected. CPS allows the equipment to communicate with themselves, carrying out the burden from the operator while providing the required information. While discussing the status of cyber-physical systems, Wang et al. marked security as one subfield that can make or break CPS [13].

2.1.1 Cyber-Physical Security

CPS consists of three components, unlike the cyber system, thus providing potential risk in three different frontiers: cyber, physical, and interaction. Therefore, traditional cybersecurity can deal with only a portion of CPS security. In his study, Wang differentiated CPS security from conventional internet security [14].

Previously, in many cases, the cyber portion of security got the sole attention. Most of the time, the physical component was either not prioritized or treated in an approach similar to that of a cyber-attack. The first major security breach that impacted the cyber-physical world was the 2010 case of "Stuxnet." A specific type of malware targeted Siemens hardware, causing the nuclear centrifuges of the Iranian nuclear plant to behave erratically and inefficiently. While doing so, the malware could display seemingly ordinary numbers in SCADA and go undetected for a long time. Later, many other instances of Stuxnet malware worldwide went undetected for a longer time [15]. The Stuxnet malware attack initialized more studies into the cyber-physical security domain. Studies have shown that such attacks have taken place for a long time. Hemsley chronologically listed major attacks on different control systems from the early 2000s to recent 2018 [15]. In his study, the author pointed out that CPS attacks surfaced from the first decade of the 21st century.

Cardenas et al. discussed cyber-physical security from a higher level. The authors thoroughly reviewed potential attacks, attack modes, and prevention strategies [7]. In a similar study, Chhetri et al. discussed the cross-domain aspects of a CPS system [16]. The authors divided such attacks into cyber-to-physical attacks and physical-to-cyber attacks. In one survey to analyze CPS security, Wu studied attacks on CPS in mainly three frontiers, attack detection, attack design, and control [17]. Genge et al. proposed a hybrid approach to analyze cyber-physical attacks on a networked control system, emulating the protocols and components and simulating the physical systems [18]. The authors analyzed physical energy and cyber signal flow to analyze how various attacks can occur that can potentially impact the other domains. Candell prepared a testbed to measure the performance of ICS against cyber attacks after following the standards and guidelines to analyze how prepared the industry is to defend against such attacks [19]. Kosturko discussed security vulnerabilities in a continuous flow reactor [20].

Studies showed that it was possible to deny access, gain full access, and rewrite the firmware to cause desired defects in the system. Lichte did one such study on using robots in Industry 4.0 that can cause potential failure or underperformance of the system [21]. Bracho used a simulation technique to assess the performance of a cyber-physical system in the event of a cyber attack. The authors divided the system into three parts: game, cyber, and physical. Multiple scenarios were simulated with different factors involved in production [22]. Orojloo analyzed various attack matrices and proposed a method to evaluate the attack's aftermath [23].

2.2 Cyber-Physical Security in Manufacturing

Security issues in manufacturing have been a significant player since the early days. From 2002 to 2012 alone, there was an estimated loss of $239.9 billion in the USA. However, often the event of an attack remains undetected. In one study, Turner et al. asked a group to investigate the reason behind the faulty product. Only a handful of people pointed toward a cyber-attack. However, no one could point out the actual reason, which was a compromised CAD file. This suggests that attacks can be treated as operational anomalies in different scenarios [24].

There have been a few studies to analyze such attacks and their impacts on manufacturing systems. Giehl et al. proposed a framework to analyze different types of attacks in a manufacturing system and their potential impact [25]. Chattopadhyay discussed the impacts of cyber-security in the manufacturing sector based on a simulation [26]. A study conducted by Elhabasy analyzed such attacks from the quality perspective and developed attack taxonomy from the attacker's point of view [27]. Ani provided an in-depth review of cybersecurity in the manufacturing domain. The authors discussed cybersecurity trends and fitted them into Industrial Control Systems (ICS). The authors suggested multi-dimensional security measures over a single-dimensional security measure for ICS [28].

2.3 Additive Manufacturing

Additive manufacturing as an idea originated at the beginning of the 20th century. With the updates of technology, it was introduced for rapid prototyping in the 1980s [29]. The product to be printed is generated using a Computer-Aided Design (CAD) model. The next step involves slicing the CAD model into a suitable format (.STL, .AMF, .3MF, or something similar). The sliced file is then converted into a suitable machine language (mostly G-code). The principal process involves printing a product by layers, extruding one layer of a material at a time on a build surface, using a method to stick the materials together, and repeating the process until the desired object is obtained. AM came a long way from the beginning to support metals and non-metals like polymers, photosensitive resin, and a few others. The adhesion process and material delivery can be different based on the requirement. Currently, there are seven major divisions of AM concerning the operating procedure. One of the most common is Fused Deposition Modeling (FDM).

2.3.1 Fused Deposition Modeling

Fused Deposition Modeling (FDM) is one of the most popular AM processes. It garnered a massive following among hobbyists and professionals alike. In this process, the material of choice is plastic, and the delivery method is through filaments. The filament is melted and fed through the extruder nozzle onto a build surface. Due to the use of fused filament, the process is also known as Fused Filament Fabrication (FFF). Printers used in the FDM process can be of different configurations. In general, the relative movement between the extruder head and the print bed results in the final print. In most cases, stepper motors are used to ensure precise movements.

2.3.2 Security in Additive Manufacturing Systems

Traditional subtractive manufacturing has existed for a long time, but the security system has not been developed yet. Whatever security protocol is available for SM security may not be replicated in the case of AM security due to their inherent differences, working principles, and many more [30]. Campbell discussed some aftermaths of counterfeiting an AM part [31].

The interconnected nature of a CPS necessitates a good understanding of the process to analyze the security aspects. An affected AM can seriously affect product quality and the supply chain. The AM process starts at the design phase. Often, third-party designers are called upon to design the product. Specialist process parameter tuners are required for complex design and equipment. These additional data movements can be a target of cyber-attacks. Suppliers often provide materials needed for the procedure. Any mild tampering with the material during the process can hamper product quality [32]. Even by sabotaging the printer's peripherals, it is possible to produce a poor-quality product. Slaughter et al. sabotaged a Powder Bed AM system by hacking in-situ IR thermography. The authors studied various ways to manipulate the reading of the thermography system. The attack targeted a closed-loop system and resulted in the delivery of an underpowered or overpowered laser beam, affecting the product quality

[33]. In this case, the antagonist did not try to attack a more secure system; instead, they targeted a related system and were able to cause damage.

Gupta discussed the AM supply chain from a security perspective, mainly focused on raw materials, 3D printers, and design files compared with conventional supply chains [34]. Yampolskiy reviewed AM security based on the industrial Powder Bed Fusion process. The authors tried to figure out possible attacks on the system at various points of the supply chain. They divided AM security attacks into IP theft and AM sabotage and discussed potential attack targets and methods [35]. Yampolskiy proposed a new framework for additive manufacturing involving tuning experts and discussed possible attacks, prevention, and detection techniques involving the communication between designers, design tuning experts, and AM manufacturers. Though additional tuning experts in the system improve cost and other benefits, they add additional attack possibilities. However, the attack methods, prevention, and detection schemes can also be applied to the traditional AM framework [36].

Moore analyzed the CPS security of AM at the first end, that is, at the design phase [37]. He studied a few popular software used on a computer and FDM 3D printers. All the analyzed software was open source, so there was enough opportunity to explore it in detail. Each software was analyzed based on its code base and performance while connected to a USB. The study showed that some software had inadequate security measures and even the software package with the most rigid security protocol could still be breached [37]. Pope et al. used Systemic Theoretic Process Analysis (STPA) to investigate the risks involved in AM. Using STPA, software analysis, and expert questioning, the authors found some risks that were not addressed in earlier literature. The authors also outlined some mitigation approaches to reduce risk or potential hazards in the system [38]. DeSmit proposed a general vulnerability assessment for any cyber-physical system, including advanced manufacturing. The overall assessment is based on the idea that the problems occur at the intersection of different system components. Process mapping is required to identify the intersection points involving cyber, physical, cyber-physical, and human components, followed by a detailed analysis of each intersection point [39]. Do et al. showed how a system could be compromised by only having access to the network [40]. It was possible to retrieve essential design data from the printer. The authors pointed to a lack of encryption for the project's success [40].

A few models have been proposed to analyze the security of a system. Zhiheng Xu used various game theory-based models to analyze cyber-physical vulnerabilities in manufacturing [41]. The author divided the whole process into the cyber-layer, physical layer, and communication layer and modeled each layer to find the system's overall equilibrium. Zarreh used a game theory-based model to assess the cybersecurity of a system. The authors analyzed some actions of both attackers and defenders with some predefined cost matrix. It was found that the cost of maintaining the defense system, loss due to attack, and cost of recovery is the main decision concerns from the security ground [42].

Wu and Moon analyzed Cyber-Manufacturing security in terms of attack vector, impact, target, and consequences. The authors also divided each into two subdivisions: cyber and physical components. It was possible to describe a few real-life attack scenarios based on the proposed taxonomy [43]. Yu used Petri nets and generalized stochastic Petri nets to analyze cyber-physical manufacturing systems. The authors proposed theoretical models to analyze the trustworthiness of the system based on reliability, availability, and security [44]. In the future, the threats to manufacturing can be far more complicated. There have been efforts to predict the future of AM security. In one such study, Johnston tried to predict AM for 2040, in which he discussed potential cyberwarfare by breaching the security system [45].

Gatlin et al. [46] used the current signature to extract the G-code information from an actual print. Gatlin's study used similar equipment and the same side channel as the one used in this research. However, the difference lies in their objectives and how the information is used. Gatlin's study was done from the perspective of IP theft, showing that even an encrypted G-code file can be reconstructed based on the power signature of the print. On the other hand, the current work uses the current signature to simulate the signatures of objects that are yet to be printed.

2.3.3 Process Monitoring for AM

In conventional manufacturing, product counterfeiting can often be traced based on some visual signs. However, in AM, things are not that simple. In AM, the infill density, structure, and manufacturing process significantly impact the physical properties of the printed object [47]. Thus, multiple things with the same external design can have different properties even though they are manufactured through the same printer. Real-time process monitoring can tell what is going on inside. There have been some studies for process monitoring in subtractive manufacturing, however only a handful were related to cyber-physical security. In one such study, Zhu proposed a smart monitoring system for CNC machines based on the CPPS (Cyber-Physical Production System) framework [48]. The authors combined various data streams like chatter, vibration, and cutting force to monitor the health of the system.

Van Elsen listed more than process parameters that can impact AM quality, and the most important of them was found to be temperature profile [49]. As a result, there have been many studies related to temperature sensing, primarily using imaging or pyrometry. Zalameda et al. used a NIR (Near Infra-Red) camera to study weld integrity during the wire-directed Energy Deposition(DED) system [50]. Hua used pyrometry to correlate melt pool size and layer thickness. The authors suggested a potential closed-loop application of the data [51]. Liu used an optical emission spectrometer to detect plasma plume emission over the melt pool during wire-DED [52]. Carl discussed monitoring an AM system for quality purposes [53]. The authors explained the quality monitoring on MTU aero engines with the help of a CMOS camera in an EOS PBF printer. This camera detects radiation, and after some data pre-processing, it checks online for quality control. Berumen used an in-line camera to monitor the melt pool and measure the melt pool radiation [54]. Rodriguez used IR cameras to investigate the building temperature on each individual layer [55]. Clijsters used a photodiode a near-infrared thermal CMOS camera, and the data capturing and processing system to monitor the melt pool in the laser powder bed fusion(PBF) process [56]. Schwerdtfeger placed an IR camera at a 15° angle to the bed, shielded by a zinc–senenide (ZnSe) window to protect the equipment from metallization in the electron beam Powder Bed Fusion (PBF) process. Like previous cases, it was designed to monitor the meltpool [57]. Price designed a system to test the repeatability of temperature measurements, build height effect on temperature, melt pool emissivity, melt pool dimensions, and thermal effects on overhanging structure [58].

Side channels can also play an important role in determining what is happening in the manufacturing space. Chhetri discussed how various emissions from 3D printers could act as side-channel and leak various information. The authors studied the FDM printer and analyzed how acoustics, vibration, magnetic, and power draws can act as a side-channel and reveal information [59]. Based on the findings of [60], Belikovetsky et al. used an audio signal to detect an anomaly in the system [61]. They recorded audio from the system using FFT and PCA to transform and reduce the data, then converted them to simple numeric outputs and appended to the G-code. In the next product of the line, the signatures were matched to detect the anomaly. The approach was successful in most cases, including addition, deletion, reordering of code, and extrusion. However, in places with length modification of less than 0.5 cm, they failed to work as planned.

Wu et al. used auditory signals to determine the condition of an FDM machine. They tried to classify the nozzle condition into either normal or normal states under different scenarios. At around 92% of the time, they were able to classify them in those two groups successfully; they were not viable to determine the machine condition in any intermediate stage [62]. However, the hidden semi-Markov model is a modified version of the SVM approach with similar accuracy, lesser data, and the ability to detect multi-stage quality [63]. As in previous cases, Chhetri used the audio signal. The authors used acoustic emissions from a two-phase stepper motor to predict the object's geometry [64], and they were able to reproduce object geometry using audio superposition. Moore et al. had a similar approach to Faruque et al. [65]. Like acoustic signals, electric power drawn by motors can be related to the load on them. Using the same principle, they collected current drawn by each motor and compared it to a known good sample to figure out if an attack occurred. In a few scenarios, they were pretty good at detecting the attack, but they were almost ineffective in some scenarios. However, combining this data may be useful to determine if there's any attack or not [66]. Al Faruque et al. used acoustic signals to generate the G-code of a printed object. The main idea is that the load carried by different motors (four in the case of single extruder FDM printers) produces different acoustic signals. After training the acoustic data with respect to the G-code data and some post-processing, they were able to reconstruct the G-code data to successfully get the outline of the geometry of the printed object [67].

2.3.4 Attack Detection

Faruque proposed an idea and algorithms required to get detailed information about the product through thermal imaging of the operation. The authors suggested that enough information about the product can be acquired by capturing the thermal image and using machine learning techniques. However, due to the camera's low resolution, it is impossible to get this done right now. The authors believe that using multiple cameras to gather data may be helpful [68]. Bayens et al. proposed three layers of verification to ensure target product quality. The authors used acoustic side channels, spatial sensing, and material verification techniques to verify product integrity. For acoustic verification, the obtained sound data was compared to a known good sample; for spatial sensing, a gyroscope was coupled with a potentiometer; for material, verification nanoparticles were used to make a unique signature known to the manufacturers only [69].

Sturm used impedance-based monitoring for AM quality [70]. It was found that PZT (Piezoelectric Transducer) sensors can be successfully employed to detect defects in AM parts in real-time. The authors could justify the repeatability of reading in the same layer, changes between layers, and changes between parts. Vincent also used PZT in their research [71]. The author proposed adding a bracket for an antenna that would attach a PZT to the manufactured part. The signal obtained from the PZT can be compared to a base signal to detect any anomaly. The approach was mainly designed to detect Trojans in IC (Integrated Circuits).

Wu et al. used a machine learning technique to detect any malicious infill structure in 3D printing. The authors used both simulated, static, and moving camera images of 3D printed objects at 3-5 layer intervals. The images are categorized into classes defective and non-defective. The authors used machine learning to classify the images in the two classes. Their study showed that moving camera images are not a good fit for the study. Their study's anomaly detection method was better than random forest, and KNN algorithms [72]. Straub applied Quality assurance techniques based on light sensing to detect AM process sabotage [73]. Belikovetsky used audio signing to detect any anomaly in the system [61]. The approach was successful in most cases, including addition, deletion, reordering of code, and extrusion. However, in places with length modification of less than .5 cm, they failed to work as planned.

Recently some modern technologies have been used or proposed to detect or prevent attacks. Many of them are either data-driven or blockchain-based. Wang suggested gathering data while manufacturing can provide sufficient information to deal with CPS attacks [14]. Babiceanu suggested that Big data can lead to virtualization and cloud-based manufacturing and help control the system [74]. Cambou discussed the usage and modification of blockchain technology to make the data more secure that can be used to analyze a system [75]. In one such case, Balta used a digital twin on an FDM process to detect anomalies and measure performance [76]. Like Cambou, Kurpjuweit also used Blockchain technology to secure a system [77]. The author discussed using Blockchain Technology in the AM supply chain. The authors used the Delphi method to find the pros and cons of blockchain in the AM supply chain. Among the potentials mentioned in this technique, IP management and data security are strongly related to CPS security. Mandolla studied adopting blockchain technology to create a digital twin of additively manufactured parts in the aviation industry. The authors discussed how Blockchain can make AM processes secure throughout the different stages of the life cycle [78]. Zhu et al. proposed a blockchain-based framework for cloud-based additive manufacturing [79]. In this framework, there is a provision for privacy protection and transaction protection, and it securely offers resource sharing. Holland discussed IP protection via signatures like visible or invisible labeling, applying RFID, and selective deposition of foreign particles [80]. The authors also proposed incorporating blockchain technology to protect IP.

Faruque proposed an idea and algorithms required to get detailed information about the product through thermal imaging of the operation [68]. The authors suggested that enough information about the product can be acquired by capturing thermal images and using machine learning techniques on them. However, it was suggested that due to the low resolution of the camera, it is not possible right now to get this done. The authors believe that using multiple cameras to gather data may be useful in this regard.

Belikovetsky Used audio signing to detect any anomaly in the system [61]. They recorded audio from the system using FFT and PCA to transform and reduce the data, then converted them to simple numeric outputs and appended to G-code. In the next product of the line, the signatures were matched to detect anomalies. The approach was successful in most cases, including addition, deletion, reordering of code, and extrusion. However, in places with length modification of less than .5 cm, they failed to work as planned. The authors came to the conclusion that the Modifications that cause a momentary mismatch but do not break the overall synchronization might show false positive results.

Bayens et al proposed three layers of verification for ensuring target product quality [69]. The authors used the acoustic side channel, spatial sensing, and material verification techniques to verify product integrity. For acoustic verification, the obtained sound data was compared to a known good sample, for spatial sensing a gyroscope was coupled with potentiometer and for material verification nanoparticles was used to make a unique signature known to the manufacturers only.

Wu et al. used machine learning techniques to detect any malicious infill structure in 3D printing [72]. The authors used both simulated, static, and moving camera images of 3D printed objects at the intervals of 3-5 layers. They had 5 different types of infill structures. The images are categorized into classes defective and non-defective. The authors used machine learning to classify the images in the two classes. The study showed that moving camera images is not a good fit for the study. Though the accuracy of analyzing the remaining two sets of images is in the range of 80-100%, there was not any mention of sensitivity or specificity, which are very important for this type of analysis. In their study, the anomaly detection method was better than random forest and KNN algorithms [63]. Straub applied Quality assurance techniques based on light sensing to detect AM process sabotage [73].

2.3.5 Attack Defense and Prevention

There have been a few approaches aimed at preventing attacks in the first place. Lee proposed a five-level guidance to implement CPS security in the manufacturing environment [81]. The authors analyzed aspects of CPS and linked them with Industry 4.0. Linares presented a risk assessment focused on IP protection [82]. They provided a recommendation to minimize the risks of this model Ivanova used physical cryptography to make the system unclonable [83]. The authors created an optical Physical unclonable function (PUF) with quantum dots(QD). The QD materials are mixed with photopolymers in VAT photopolymerization to print the product additively. QDs entrapped in the product result in an unclonable signature for the product. With a similar goal in mind, Binard proposed a technique to watermark the surface with some traceability features. It was designed for the SLM process and partially remelting the last layer [84].

2.4 Literature Gap

Most of the existing research on attack detection in AM using side channels works by comparing suspect data to known-good data. There are a few instances where G-code information was used to generate known-good data. In their study, Rais used mixed optical rotary sensors and temperature sensors to model the spatially temporal information of the prints [85] . Yu did use G-code information as a baseline for a known-good sample. Their research, however, used a repository of 20GB of data to match different sensor data and G-code timestamps [86]. Our proposed approach, though initially using a data repository to study the data, does not require the repository to generate signals. The mathematical modeling approach provides a more robust way of simulating the signals. In short, our research is unique in that it uses mathematical modeling to simulate the current signal.

Chapter 3

System Description

The system used for the study consists of designing and slicing software, a Lulzbot Taz 6 3D printer, a Picoscope oscilloscope 5444D, and current clamps to measure the current draw. Matlab is used for the data analysis described in the dissertation.

3.1 Design and Slicing Software

The first step in making an AM product is designing it. The required Computer-Aided Design (CAD) model can be made through various software like SolidWorks and Fusion 360. The design is then converted into a stereo-lithography format suitable for 3D printing. The most popular stereo-lithography formats for 3D printing are STL, 3MF, and AMF. In this study, Fusion 360 was used to get up to this point. The next step is to convert the file into suitable machine instructions. This step is known as slicing. The slicing software used in this study is "CURA, Lulzbot Taz Edition." This particular software is used since it is the software recommended by the machine vendor. However, the printer is capable of using files sliced by other slicing tools. The output of the slicing step is the G-code file. This file contains all the required instructions to successfully print a 3D object.

3.2 Lulzbot Taz 6 3D printer

Lulzbot Taz printers are widely used FDM printers by hobbyists and professionals. The large print size and high print quality are some of this device's major selling points. This printer is capable of printing objects up to a dimension of $280 \times 280 \times 250$ mm in size. This is a plug-and-play device requiring no additional setup for printing. The print surface can be heated up to 120° C and can move only along the Y-axis. This printer comes with a single extruder configuration with an option to use a dual extruder. The printer used in this study is with a

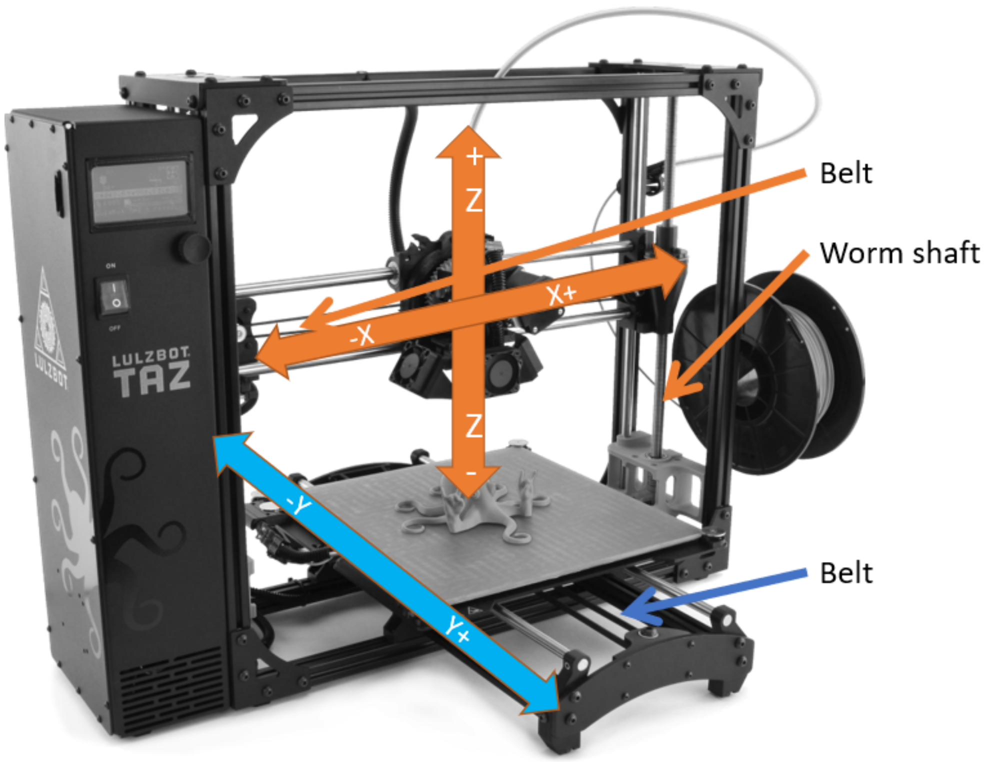

Figure 3.1: Lulzbot Taz 6 Printer

single extruder. The extruder used in this study can be heated to a maximum of 290° C and can move along both X and Z axes. This printer supports raw materials including PLA, ABS, Nylon, and many others [87]. The raw material is supplied as a 2.85mm diameter filament. The filament is then heated up to its specified temperatures based on the material used, and the fused filament is extruded with the help of an extruder motor. In order for the printer to work, it needs to be fed with some instructions. The printer takes a G-code file as the input instructions. The G-code command is broken down by the controller, and different instructions are sent to different components to finish a task. Taz 6 is an open-loop system; thus, it can not double-check its current position and rectify it. For the different movement operations, it thus uses stepper motors. Stepper motors are capable of moving into precise positions due to their inherent nature. Each of the X and Y axes and the extruder has one stepper motor, while the Z-axis has two. The usage of the belt-pulley mechanism makes the X and Y-axes capable of moving tiny distances. The Z-axis lacks a belt-pulley mechanism, and thus the smallest travel distance along the Z-axis is more than that of the X and Y axes. All the motors used in this printer are NEMA 17 motors, with the model number MS17HD6P4150. Figure 3.1 depicts the Lulzbot Taz 6 printer utilized in the study. The figure includes annotations where the orange bi-directional arrows represent the movement orientation of the extruder, and the blue bi-directional arrow indicates the movement orientation of the print bed. Additionally, the single-headed arrows correspond to the movement mechanism of their respective matching color.

3.2.1 Stepper Motors

Stepper motors are the single most important component of the study. Previous studies on anomaly detection using the current draw were based on the properties of the stepper motors. Since all the movements are performed in an open loop system using the stepper motor, they can provide a lot of information regarding what is being printed and at what speed. The motors used in the Taz 6 are 2-phase bipolar motors. For each phase, two wires make a loop to deliver current from the controller. The schematics given by the vendor of the motor ("Moon Industries") are shown in Figure 3.3. In order to make the motors work, the current is delivered in a sinusoidal waveform. The current is delivered to the motor stator. The stator has 48 teeth in total. The rotor in Figure 3.3a is made of a permanent magnet. This particular motor used has 50 teeth in the rotor. The tooth used has same width, thus, it is impossible to align all the teeth perfectly. This unbalanced teeth count is there to help the motor rotate. Based on the phase energized, the stator will attract some part of the rotor resulting in movement. Based on the way the current is delivered, the rotor either moves clockwise or counterclockwise. The movement orders are shown in figure 3.3b. The frequency of the sinusoidal current wave is proportional to the rate of current delivery by the controller, which is proportional to the feed rate.

The minimum movement possible with a normal step size in this motor is 1.8°. These motors are capable of "half-stepping," making the movements as small as 0.9°. Since the X and Y-axis motors are linked with similar belt pully systems, their unit rotation moves the axis the same amount. Unit Z-axis motor movement results in different lengths of movement than the other axes. One thing of high importance is that the manufacturer of the motor claims to have a tolerance of 5%. This suggests that the motor can sometimes have up to 5% lower or

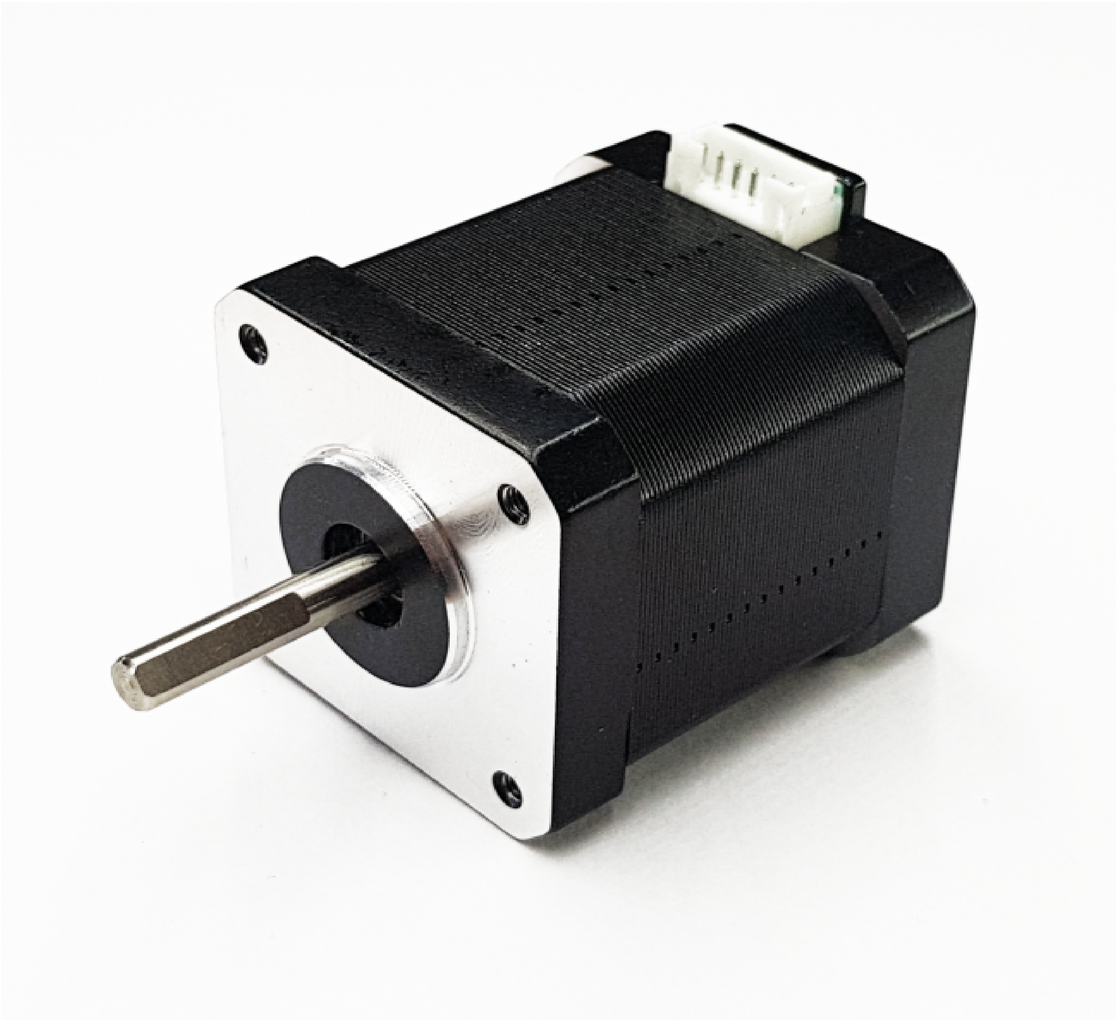

Figure 3.2: Nema-17 Stepper Motor

higher speed than the expected one. In our study a few times the speed was found to be more than the stated speed.

The movement of the motors is carried out when the required phases are energized. Here A and C remain in opposite phases while similar to B and D. Thus the peak of A aligns with the trough of C, and a similar happens for the B and D pairing. However, peaks of A/C and B/D differ by a small phase difference. For a particular movement along the x-axis, the current profile for wires A and C are shown in Figure 3.4. It is evident that the current in wires A and C are opposite in nature and magnitude. Reversing the current flow of C shows how close they are as signals A and C appear to be nearly identical in Figure 3.5.

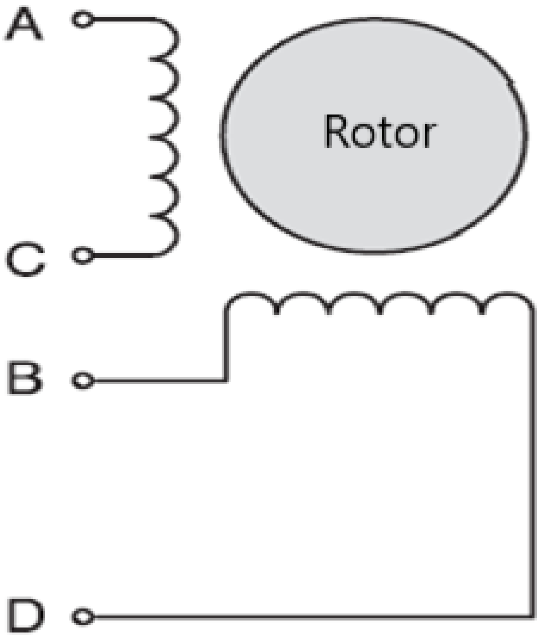

(a) Stator and Rotor Setup

Bipolar, Full Step

STEP	Phase 1 A	Phase 1 C	Phase 2 B	Phase 2 D
1	+	-	+	-
2	-	+	+	-
3	-	+	-	+
4	+	-	-	+

CW ↓ CCW ↑

CW & CCW rotation when seen from flange side of the motor.

(b) Motor Movement Direction

Figure 3.3: Stepper Motor Schematic
[88]

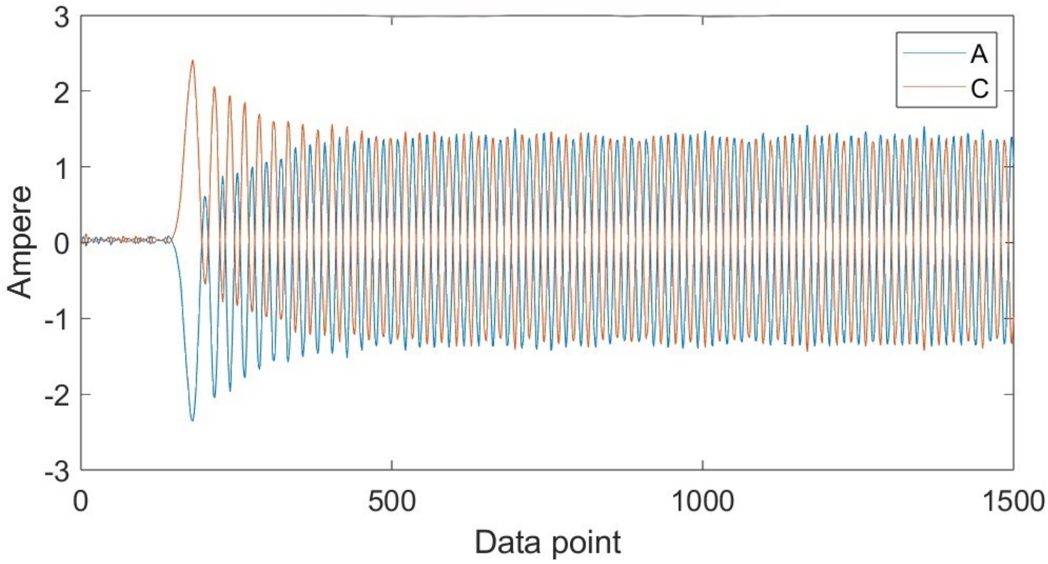

Figure 3.4: Current Behavior at A and C

A similar pattern is visible while working with wires B and D. On the other hand, for a particular movement along the x-axis, wires C and D displayed the behavior as shown in Figure 3.6. In this case, C and D have similar properties in terms of amplitude, wavelength, and the duration of the wave. However, they are temporally misaligned by a phase difference. Since stepper motor rotations are executed by order of energizing the cycles, the current profile may look different based on their phases. Thus, the duration and frequency of the energized signal carry more information than the phase they are in. However, a change in waveform during a movement indicates the change in direction, though it cannot determine the absolute direction.

Since a unit rotation of the motor results in some fixed length of movement along that axis, it is logical to have rotations at a higher speed to comply with the higher printing speed requirement. The frequency of the sinusoidal current wave is proportional to the rate of current delivery by the controller, which is, in turn, proportional to the maximum feed rate. Thus, a movement with the same distance with a higher maximum feed rate has the same number of peaks but with a higher frequency. Often the waves are characterized by having larger wavelengths at the beginning of a movement, then gradually converging to a value and increasing again. This pattern is consistent with the concepts of acceleration and deceleration. From rest, the motors speed up to attain the maximum feed rate specified by the G-code and then reduce the speed to come to rest. This zone of acceleration and deceleration is more prominent with a

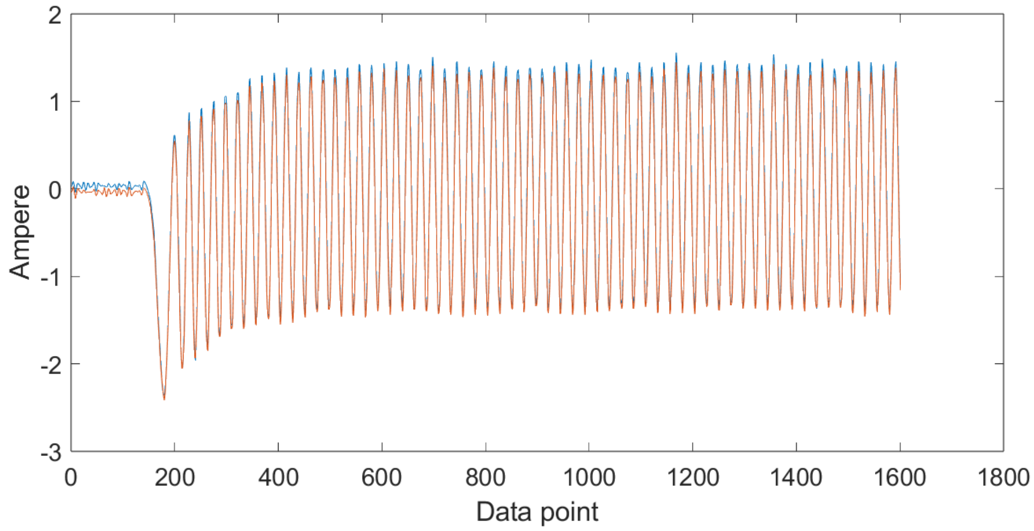

Figure 3.5: Modified Current Behavior at A and C

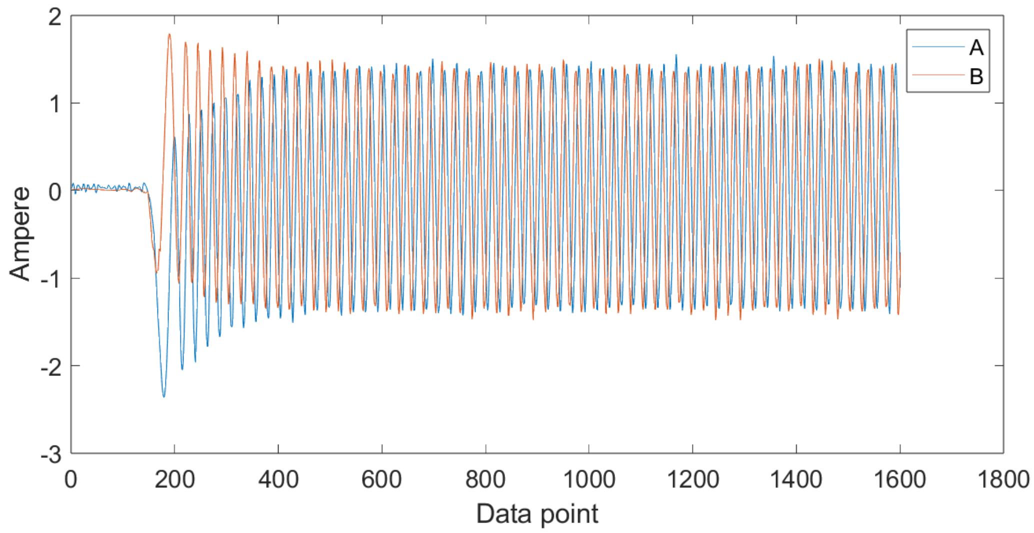

Figure 3.6: Phase Difference Between C and D

higher maximum feed rate. A good G-code command intends to speed up when no material is being extruded to speed up the whole process, and while printing, a lower speed is selected such that acceleration or deceleration does not impact the quality. Thus, non-printing movements are associated with a higher feed rate than printing movements. Unidirectional movement of the printer is fairly straightforward, only one motor is in action, and the power waveform can be predicted using the feed rate and distance to travel. Things become interesting for the simultaneous movement of the X and Y axes together. Thus the feed rate of the axis moving a lesser distance would be altered to match the desired movement. A change in direction is often characterized by an inflection point. However, if the change takes place at either peak, the changing point is hard to pinpoint

3.3 PicoScope

Figure 3.7 shows the oscilloscope used in this study. An oscilloscope is a device that is used as electronic test equipment and for data collection and visualization. The particular model used in this research is Picoscope 5444D. The oscilloscope in use is capable of collecting data in as many as four channels simultaneously. For this study, one current clamp is used for each of the X, Y, Z, and E (extruder) axes.

Figure 3.7: Picoscope 544D Oscilloscope

Figure 3.8: Pico TA018 Current Clamp

Figure 3.8 shows the current clamps used in this study. The current clamp use is of model TA018 from PicoScope. Though each motor is controlled by four wires, the current clamps are used around only one of the wires; in this case, the clamps are used on C wire (green colored wires). The clamps used were 60 Ampere clamps in the 20 amp mode. Data collection was done at a sample rate of 1000 per second. AC coupling was used for the data acquisition. The Picoscope was connected to a desktop via USB to collect data. The collected data was captured in CSV format for further study.

3.4 Connection

The connection involves opening the back plate to access the connection between the stepper motors and the central processing unit. Each motor is connected to the control unit through four wires. As mentioned in Section 3.2.1, the current clamp connected to any wire of a motor provides the same information. For this reason, current clamps are connected to only one wire of each motor. The current clamps are set to 20Amp mode. The current clamps are then connected to the Oscilloscope. Clamps are connected to the X, Y, and Z axes, and the extruder is connected to the A,B,C, and D channels of the oscilloscope, respectively. The output cable of the oscilloscope is connected to a computer. The data collection process was then carried out using the Picoscope 7 software. Figure 3.10 shows different settings used for the data

Figure 3.9: Lulzbot Taz with Attached Current Clamps

collection. The probes are selected as current 20/60, followed by 20A as shown in Figure 3.10a, the vertical axis is set as 5A as in Figure 3.10b, and the coupling mode was changed from DC to AC 3.10b. Each window of the software has 10 divisions, and each division is set to be 100 seconds long, as in Figure 3.10c. This setting, however, has nothing to do with actual data. This is the user's choice. Data is collected at a rate of 1000 Hz. Thus, the total sample in a window is 1 million, as shown in Figure 3.10d

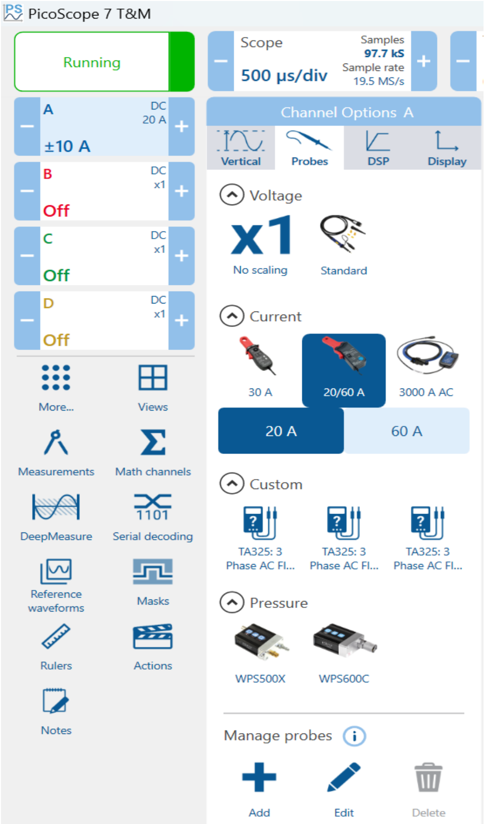

(a) Current Clamp Probe

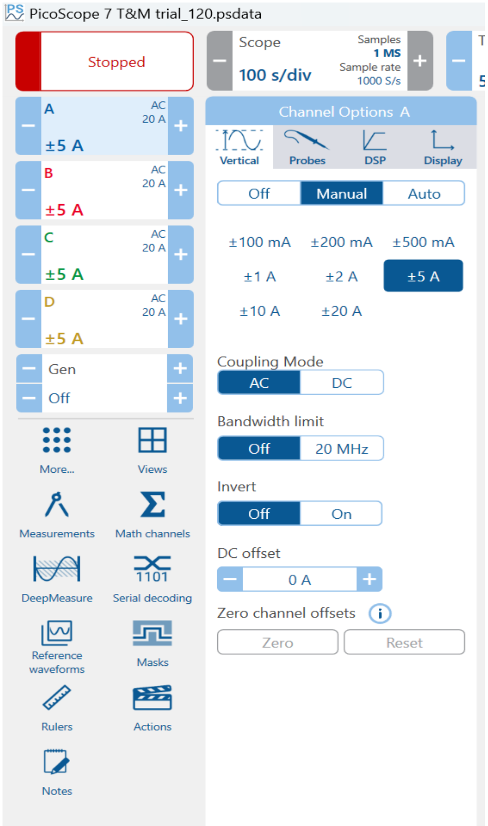

(b) Coupling and Axis Length

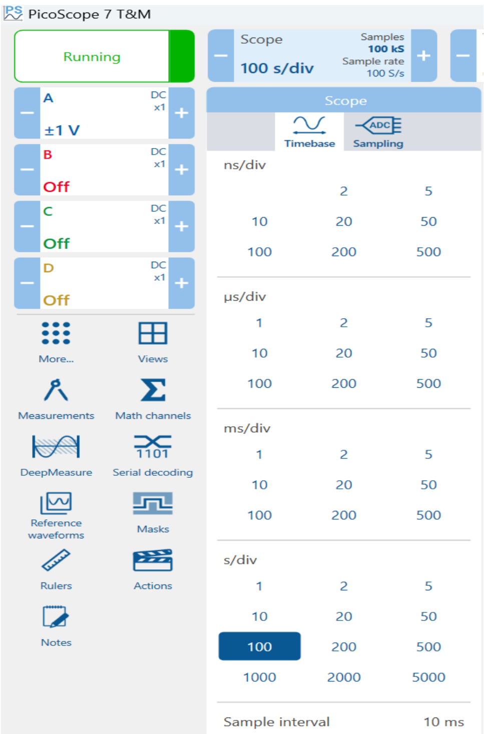

(c) Division per Window

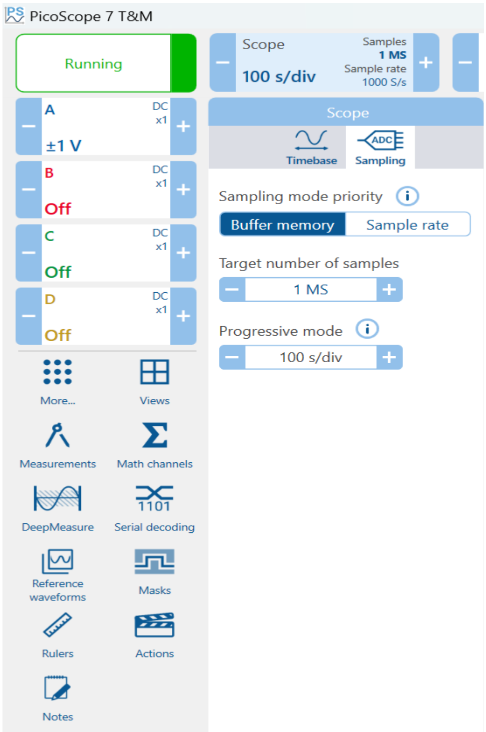

(d) Target Samples

Figure 3.10: Picoscope Settings

Chapter 4

Simulating Current Profile for Straight Lines and Curves

4.1 Introduction

Additive manufacturing has improved the flexibility of manufacturing many times. This novel technology allows the manufacturer to create complex objects with relative ease. Complex jet fuel nozzles and human prosthetics are a few examples of complicated designs fabricated with AM. However, the layer-by-layer manufacturing technique can be used against it. One such example is creating a low-strength drone propeller [60]. The printed part met the geometric specifications but had altered mechanical properties due to a change in the internal structure. Adversaries may be inclined to alter the mechanical properties keeping the topology the same to bypass the visual quality inspection. Therefore, process monitoring techniques are required to ensure product integrity. However, there are instances where process monitoring fails, as evident in the case of the Stuxnet malware attack. One such side channel is the power drawn by the actuators. This side channel is found to be successful in reconstructing the printed object geometry [46]. It is evident that a change in the G-code file may result in the same object geometry; it will definitely have a different current profile. This work is dedicated to creating a reference power draw profile, eliminating the need to require unaltered print parameters. The principle concentration is given to straight lines and curves.

4.2 Data Collection and Signal Analysis

Initially, a few test runs were conducted to observe the pattern of the current signal. In order to get a reading of the current signal, the 60 Amp probes were connected to the motor wires. There is one motor for each control of the X and Y axes as well as for extruding material. The movement along the Z axis, however, needs two motors. For our study, one of the Z-axis motors was not used, as the readings of the two Z-axis motors are the same. Each motor has four wires connected to the power source. To maintain consistency, all the green wires (2nd wire of each motor) are clamped to their respective current clamp. The clamps are set to 20 Amp mode and then connected to the Picoscope oscilloscope to measure and record data. The sample interval used here is one millisecond (ms), and the sample rate was 1000Hz. The coupling used here is AC coupling. In order to understand the pattern of the power signal, a simple hollow rectangular object was printed. The test object had a dimension of 15 mm in length, 10 mm in width, and 5 mm in height. The slicer used here was the manufacturer-recommended one, known as “Cura- Lulzbot edition- 3.6.13”. The object was printed five times in each of the standard template settings, “High detail,” “Standard,” and “High speed.” This was done to observe the consistency and scalability of data. It is to be noted that once a new print is ordered, the printer always performs a set of movements to facilitate the printing. In the case of our printer, it does move to the home position, cleans the nozzle, automatically adjusts bed level, and adjusts extruder and print bed temperature to result in a better print. Since all these steps are identical in all the prints, this research is interested in the activities after all the common steps are performed. The notable change point between the preliminary steps and final printing is the setting of the extruder temperature. Thus, the research here is more interested in the data after the extruder temperature is set. Though movements can be traced back to some mathematical formulae, some dwelling patterns can’t be. Thus, the whole simulation process uses a hybrid approach using mathematical modeling and machine learning. The major components of the simulation can be classified into the following properties.

The equation of AC current signal is given in Equation 4.1. Where,

- $f(t)$ is the instantaneous current at time t,
- A is the amplitude,
- ω is the angular frequency in radians per second,
- ϕ is the phase angle in radians.

$$f(t) = A\sin(\omega t + \phi) \tag{4.1}$$

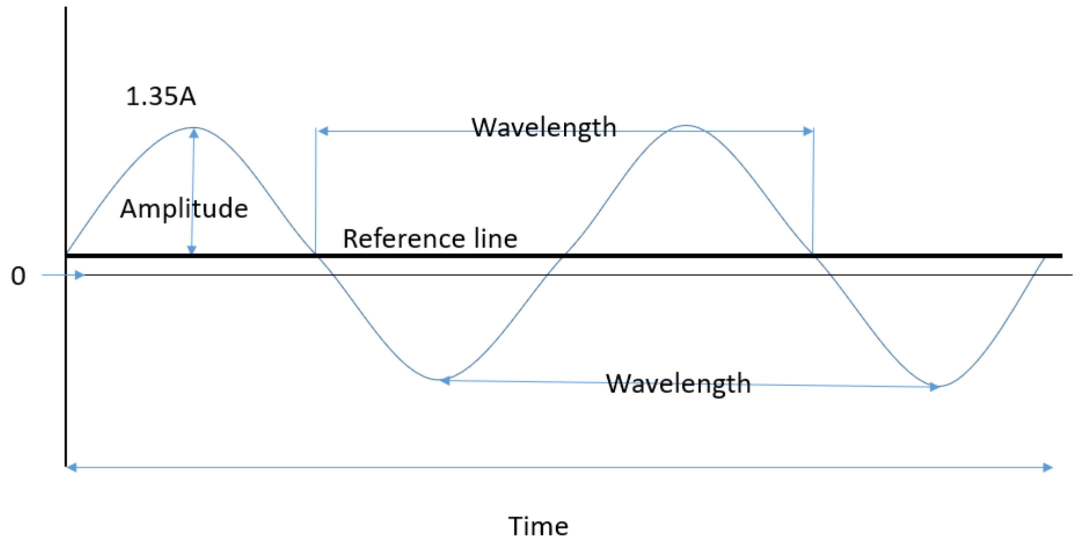

Figure 4.1: A Typical Current Signal

4.2.1 Power Signal Nature

Since the stepper motors operate by the successive energizing and de-energizing of the adjacent portion of the stator, the power drawing pattern of a stepper motor resembles an AC signal. Theoretically, the arithmetic average of a full wave is zero. However, in real life, they show a deviation from zero. In our test runs, the same conditions of the experiment resulted in different offset values. In our simulation, the average is considered to be 0. Once the motor itself is de-energized, there's a residual current left in the wire, which gradually becomes zero. They resemble a negative exponential pattern in this movement. If the motor is energized before reaching zero, the peak may be greater or less than the following waves based on previous waves.

4.2.2 Amplitude

The amplitude of an alternating current (AC) refers to the maximum value of the current during one cycle. In a sinusoidal AC waveform, the amplitude is the peak value that the current reaches, either in the positive or negative direction. This is depicted in Figure 4.1.

The rated current of the stepper motors used is 1.5 Ampere. However, from various test runs, the peak is around 1.35 Ampere. Depending upon the DC offset, the peaks may be slightly more or less. In general, the prominence remains around twice the peak for the whole time.

4.2.3 Frequency

The frequency of the wave is the single most critical component of this wave. Frequency can be obtained by dividing the velocity by wavelength. Gatlin et al. [46] noted that a full wave is represented by a single-step movement. For the stepper motor used in the Lulzbot Taz 6 printer, the step size is 1.8 degrees. Since every unit of movement produces the same number of sinusoids, a higher feed rate results in a higher frequency. For a given feed rate of 600 mm/min, the wavelength is measured by a few trial runs. The data of these trial runs were denoised using wavelet transformation. It was then decomposed into the frequency domain by using Fast Fourier Transform (FFT). The frequency obtained this way is used as the base wavelength of a feed rate of 600. With a change in feed rate, the wavelengths change proportionally. For example, if the feed rate given is 1200mm per minute, the frequency will be twice the base frequency.

4.3 Noise removal

The signal obtained from the Picoscope contains high-frequency noise. The noise throughout the length of time exhibits similar properties. The presence of noise in the signal affects the ability to detect important features like peaks, troughs, and dwells. Gatlin [89] used a modified low-pass filter to omit high-frequency noise from the signal. This approach has one possible problem. The frequency of current and printing speed are directly proportional, thus at some higher level of speed, there might be some overlap between the actual signal and noise.

Another approach to denoising a signal is wavelet smoothing. Wavelet denoising is a popular choice for removing noise from a signal while preserving its important features [90]. The discrete wavelet transform (DWT) is commonly used in wavelet denoising. It decomposes a signal into a series of wavelet coefficients at different scales and positions. These coefficients represent the signal's details at various resolutions [90]. A successful implementation of wavelet denoising requires selecting the right wavelet family and threshold techniques. In our research, we used the most widely used parameters, “Symlet” as the wavelet family and “Donoho-Johnstone” threshold [91]. Figure 4.2 demonstrates the process of wavelet denoising. First, a wavelet decomposition on the input signal using the specified wavelet and decomposition level is performed. For this research, wavelet 'sym' and a decomposition level of 4 are used. The next step is to compute a threshold value for noise reduction. This threshold is typically based on the statistical properties of the wavelet coefficients. There are different types of thresholding techniques; the type used here is “Donoho-Johnstone”. This is chosen for its automatic noise adaption ability.

The next step is to apply soft thresholding to the detail coefficients obtained from the wavelet decomposition. Soft thresholding involves reducing the magnitude of coefficients below the threshold to zero and shrinking the remaining coefficients by the threshold value. This helps in reducing the noise in the signal. Finally, the signal from the modified wavelet coefficients is reconstructed. The reconstruction approach results in a denoised signal. Figure 4.3 and 4.4 demonstrate a signal before and after the denoising filter is applied. Zones marked in red symbolize equivalent segments of data.

4.4 Signal Properties

The movement mechanism of the printer determines the signal properties. Though identical stepper motors carry out all the movements, the mechanism of translating the circular movement of the motor to linear motion is different. Movements along the X and Y axis are performed with the help of a belt-pulley mechanism. For the Z-axis, a worm shaft mechanism aids movement. This results in a deviation of the behavior of the current profile of the Z axis from the X and Y axes. The deviation, however, lies in the frequency of the resulting signal. Before describing the details of the signal properties, the feed rate must be known. In this study, the term feed rate signifies the maximum allowable speed for a particular movement, and the default unit used is millimeters per minute. The next portion of the paper discusses behaviors of the current signal based on different conditions. In order to understand current properties, it is important to map the power signal with different sections of the G-code. Since there were few

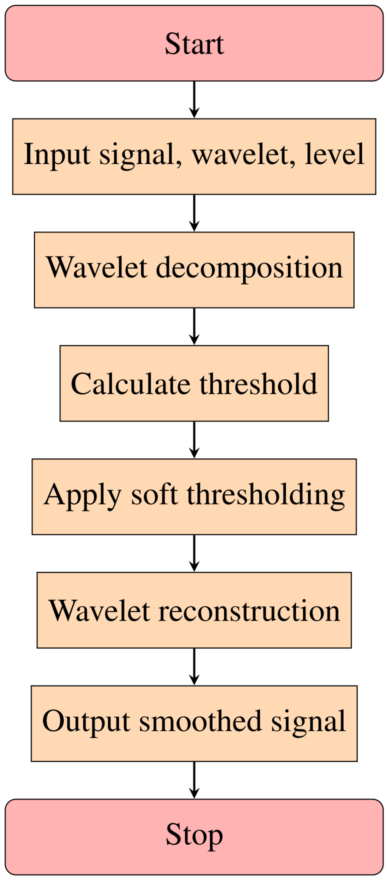

Figure 4.2: Wavelet Smoothing

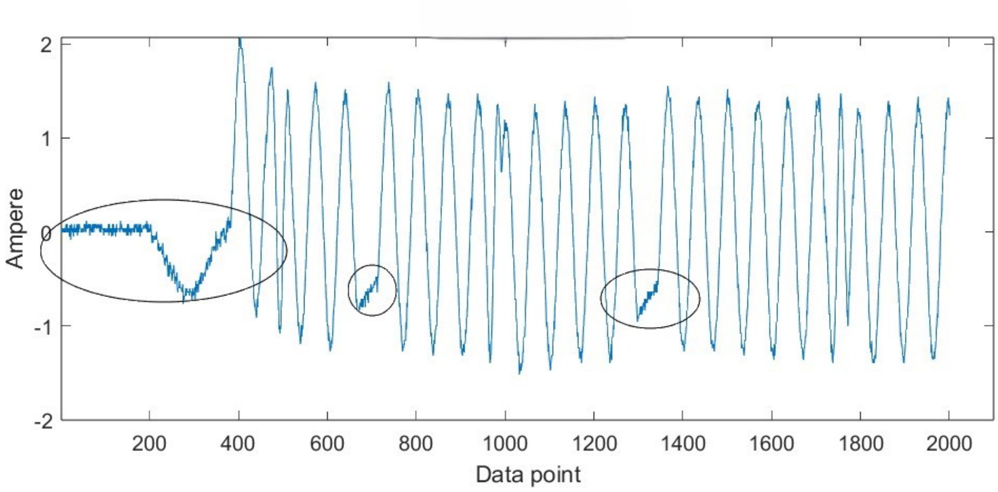

Figure 4.3: Signal Before Noise Removal

lines on G-code with very small movement ordered on them, it was necessary to understand how those small lengths of movement are captured in our data stream. The following sections discusses the general properties of the signals

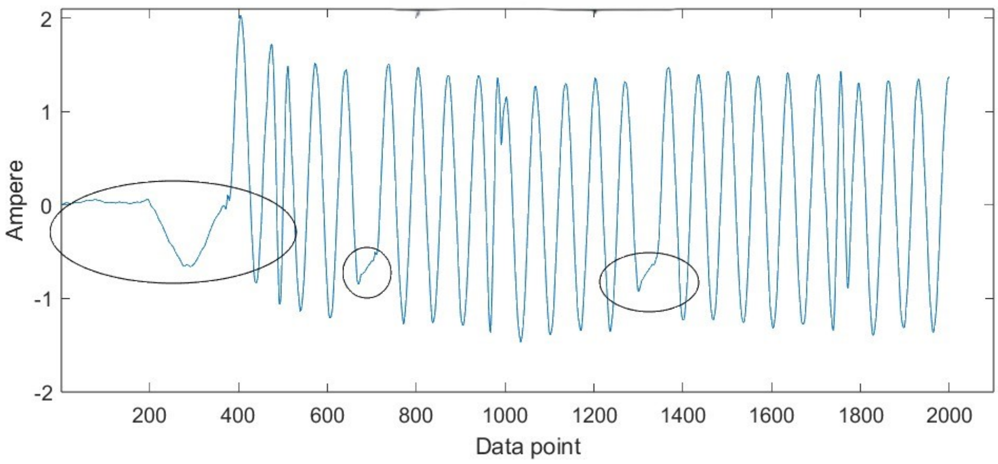

Figure 4.4: Signal After Noise Removal

4.4.1 General Properties of The Signal

The particular stepper motor used in this printer has two phases, each connected by two wires making a loop. The rotor is magnetized, thus providing current to the stator, affecting the rotor. Based on how the current is delivered, the rotor can move clockwise or counterclockwise and fast or slow. The current is delivered in a sinusoidal pattern, making it an AC signal [46]. The resulting signal properties of amplitude, frequency, and phase vary based on the input command. The motor used in this printer model has a step size of 1.8°. The equation of the current can be expressed as Eq. 4.2

$$f(t) = A \times sin(2\pi f t + \phi) \tag{4.2}$$

In this equation, A is the amplitude, f is the frequency, and t is the time. The amplitude used in this equation is obtained from the observed signals. The frequency is the number of full cycles per unit of time. Since a certain distance requires an equal number of cycles irrespective of the feed rate, frequency becomes directly proportional to the feed rate. In this study, the frequency was measured for a feed rate of 600 mm per minute as a base frequency and used to measure the frequency at different feed rates. Figure 4.1 shows these features of current signal.

4.4.2 Movement Along the Same Direction

The most straightforward movement for the printer is movement along the same direction at the same speed. Adding one such command results in a signal that behaves like the continuation of the last signal. The last known phase of the previous signal acts as the initial phase of the resulting signal. A change in the feed rate changes the frequency, but the direction of the movement remains unchanged. Figure 4.5 exhibits movement along the same axis and includes two separate movements with different feed rates.

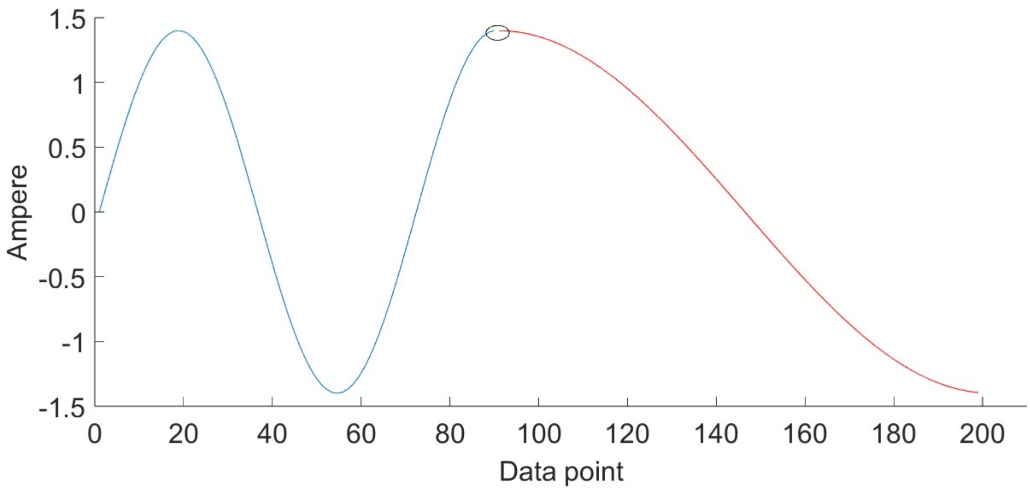

Figure 4.5: Consecutive Commands to Move in the Same Direction

4.4.3 Movement Along the Opposite Direction

Movement in the opposite direction is carried out by changing the pattern of the current delivery. As a result, a change in the direction is characterized by a change in the direction of the sinusoidal wave. Figure 4.6 exemplifies two movements along opposite directions and different feed rates.

4.4.4 Stop, Dwell, and Start

During a print, movement along a direction stops for a while and restarts along the same or the opposite direction. This kind of movement is called dwell. Once a movement stops, there

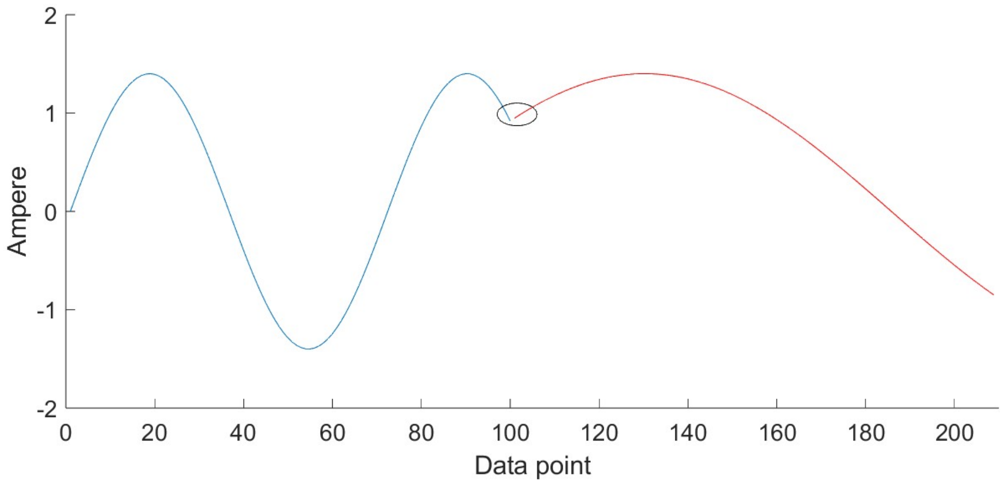

Figure 4.6: Consecutive Commands to Move in Opposite Direction

remains a residual current in the loop. In an ideal case, the current draw for a static motor should be zero. The current signal, in such cases, attempts to merge with the optimum value, zero. Once the motor is started again, the resulting signal takes the phase before the dwell step as the initial phase, and the signal is generated accordingly. Figure 4.7 illustrates the properties of the current signal when a motor stops and starts after some time. In this case, the movement is in the same direction.

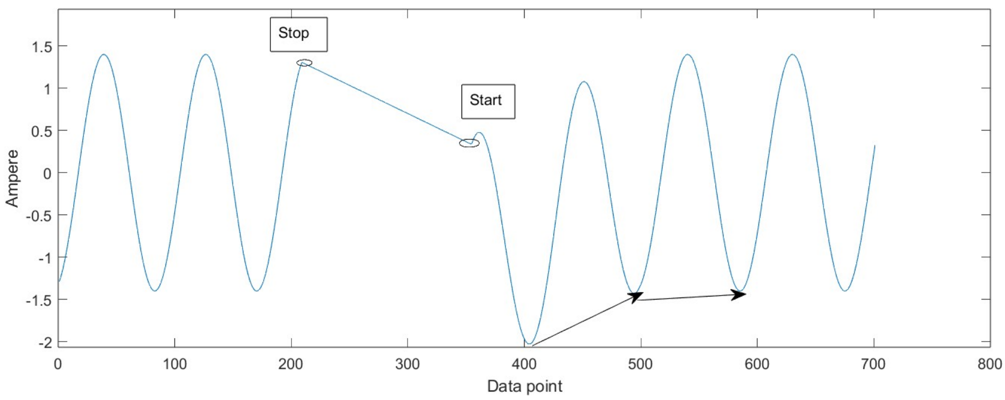

Figure 4.7: Starting a Movement After Dwell

4.4.5 Movement Along the Horizontal Plane

Movement along the horizontal plane can be either the X or Y axis or the X-Y plane. The difference between these two types lies in the feed rate adjustment. If a particular line of G-code command requires a movement of x units along the X axis and y units along the Y axis at a feed rate of f, the distance traveled, S, will be,

$$S = \sqrt{x^2 + y^2} \tag{4.3}$$

The adjusted feed rates along the X and Y axes would be 4.7 and 4.8, respectively.

$$feed_x = \frac{(abs(x)) \cdot ratedfeed}{\sqrt{x^2 + y^2}} \tag{4.4}$$

$$feed_y = \frac{(abs(y)) \cdot ratedfeed}{\sqrt{x^2 + y^2}} \tag{4.5}$$

Since the motor can not reach the highest speed or a full stop instantly, signals are usually accompanied by acceleration and deceleration phases at the beginning and the end of a movement. However, this behavior is not as apparent in the case of lower feed rates. As the feed rate increases, the behavior becomes more prominent. After printing several objects using the default set-up, movements with feed rates over 600 mm per minute exhibit some impact of acceleration and deceleration in the duration of the movement. The maximum acceleration attainable by the motors can be found using Equation 4.6.

$$T = \frac{2 \times feed}{a} + \frac{S - \frac{feed^2}{a}}{feed} \tag{4.6}$$

The equation is obtained by modifying the equations of motion. Here T is the time required for a motion to complete, a is the maximum acceleration, S is the movement, and $feed$ is the feed rate, which can be replaced by $feed_x$ or $feed_y$ based on the situation. The highest possible feed rate of the printer used is 18,000 mm per minute [87]. Experiments were run to record the run time for a length of 40mm with feed rates of 300, 600, 2,000, 6,000, 12,000, and

18,000 mm per minute. A length of 40 mm is chosen as a representative length that can exhibit stages of acceleration, constant speed, and deceleration distinctively. These values are used in Eq. 4.6 to find the maximum acceleration for different feed rates. The acceleration curve is then used to interpolate acceleration at any given or calculated feed rate.

Once the maximum acceleration is found, the same equation can be used to find the time required to complete a movement at a given feed rate.

4.4.6 Acceleration and Deceleration

One property of this signal is acceleration and deceleration. Since the motor cannot instantly move to the maximum allowable speed from rest, the beginning of each cycle is associated with acceleration. Similarly, the last portion of a movement cycle is accompanied by a deceleration. However, the changes are more prominent with a higher speed. Figure 4.8 shows a segment of movement divided into sections of acceleration, constant speed, and deceleration.

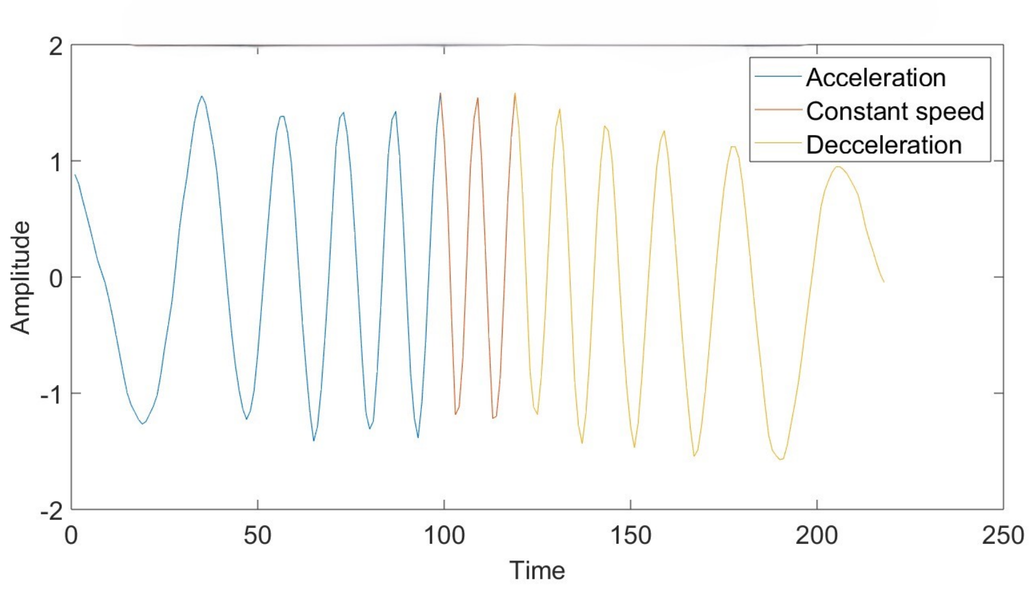

Figure 4.8: Section of Signal Showing Acceleration, Constant Speed and Deceleration

4.5 Case Studies

A case study is provided to illustrate the approach described in the previous section. The horizontal movements can be divided into linear and curvature movements. The linear movements can be again subdivided into single-axis and dual-axis movements. This type of printer's curvature movements are always associated with dual-axis movements. A vertical movement is similar to a single-axis horizontal movement. In only a few cases, all three axes move together. This type of movement is denoted as complex movements and is discussed later in the case studies. In the following case studies, the movements are characterized, and the current signal is predicted. Since the printer can not print a single line, the objects printed in this study are only two lines thick. For each case, the movement in discussion is ordered ten times, and the mean value is put forward.

4.5.1 Straight-lines

Predicting the power signal for straight-line features can be divided into two sections: movement along one axis and movement along both axes. In either case, the feed rate significantly impacts the signal generated. For lower feed rates (usually used while actually depositing material) there is no visible acceleration or deceleration; the same can not be said for the higher feed rates. This study thus discusses both the scenarios in high and low feed rate cases. The lengths chosen for this study are 1 mm, 10 mm, 20 mm, and 40 mm. Since curve lines consist of many small fractions of straight lines, lengths less than 1 mm are not considered for straight-line studies. The feed rates used are 300 and 600 as low speed, and the high-speed feed rates used are 2000 and 6000. The unit of feed rate is mm/minute.

4.5.1.1 Single-Axis Movement:

Simulating straight-line movement along a single axis is the least complicated. Since a particular movement along either the X or Y axis results in the same signature, in this study, the movement direction is taken along the X-axis. The feed rate stated in the G-code acts as the true feed rate used in the printing process. This feed rate is used to determine the frequency of the resulting sinusoidal wave for the X-channel. The Y-axis data theoretically remains zero throughout time. Cases with different feed rates are discussed in the following sections.

4.5.1.1.1 Feed Rate of 300: A slow feed rate of 300 mm per minute does not show a visible trend of acceleration and deceleration in the signal. Table 4.1 summarizes the actual and predicted signal based on time needed, number of peaks and accuracy.

Length (mm)	Time (Actual), s	Time (Predicted), s	No. of Peaks (Actual)	No. of Peaks (Predicted)	Accuracy (Time)	Accuracy (Peak count)
1	0.20	0.20	1	1	100	100
10	2.00	2.00	15	15	100	100
20	4.00	4.00	31	31	100	100
40	8.00	8.00	62	62	100	100

Table 4.1: Single Axis Movement at a Feed Rate of 300.

At this feed rate we observe that the time and peak count prediction are accurate. It is expected to have a high accuracy for a feed rate of 300, as this speed is usually reserved for prints with highest quality.

4.5.1.1.2 Feed Rate of 600 Like the case of a feed rate of 300, there is no visible period of acceleration and deceleration, but a slight change in time is observed. Table 4.2 compares the actual and predicted signatures in matrices used in the previous case. It is observed that the time needed for the same length of movement in a feed rate of 600 is almost half that of a feed rate of 300. However, the number of peaks remains the same.

Length (mm)	Time (Actual),s	Time (Predicted), s	No. of Peaks (Actual)	No. of Peaks (Predicted)	Accuracy (Time)	Accuracy (Peak count)
1	0.10	0.10	1	1	100	100
10	1.00	1.00	15	15	100	100
20	2.00	2.00	31	31	100	100
40	4.00	4.00	62	62	100	100

Table 4.2: Single Axis Movement at a Feed Rate of 600.

4.5.1.1.3 Feed Rate of 2000 A feed rate in the range of 2000 is needed when the primary purpose is to move the print bed or nozzle in a short range without extruding any material. Movement at this feed rate shows small transitions of acceleration and deceleration. In comparison to previously used feed rates, the number of peaks remains the same. In contrast, the time needed for the movement is not directly proportional to the feed rate. The time needed is slightly more due to slower periods at the beginning and end of the signal.

Length (mm)	Time (Actual), s	Time (Predicted), s	No. of Peaks (Actual)	No. of Peaks (Predicted)	Accuracy (Time)	Accuracy (Peak count)
1	0.03	0.03	1	1	99.97	100
10	0.36	0.36	15	15	99.98	100
20	0.66	0.66	31	31	99.99	100
40	1.25	1.25	62	62	99.99	100

Table 4.3: Single Axis Movement at a Feed Rate of 2000.

4.5.1.1.4 Feed Rate of 6000 A movement with a feed rate of 6000 exhibits similar behavior to that with a feed rate of 2000. Even though this feed rate shows significant areas of acceleration and deceleration, the properties and accuracy remain similar. It is observed that the time needed to move 1mm at a feed of 2000 and 6000 are almost same. This suggests that, during this movement, the speed never reached its rated feed.

Length (mm)	Time (Actual), s	Time (Predicted), s	No. of Peaks (Actual)	No. of Peaks (Predicted)	Accuracy (Time)	Accuracy (Peak count)
1	0.03	0.34	1	1	99.97	100
10	0.26	0.26	15	15	99.96	100
20	0.36	0.36	31	31	99.97	100
40	0.56	0.56	62	62	99.98	100

Table 4.4: Single Axis Movement at a Feed Rate of 6000.

The study of movements along one axis shows that irrespective of the feed rate, the number of peaks in the signal is going to be the same. The time required for a movement remains proportional to the feed rates, provided the printing speed is lower.

4.5.1.2 Dual-axis movement:

A movement with non-zero components along both axes needs some adjustment to correctly predict the signature. The first adjustment needed is that of the feed rate. Since the movement along a single axis shows the impact of different lengths, a single length is chosen for this study. However, in this case, the prediction was made for straight lines of length of 30mm at angles 15, 30, and 45 degrees with respect to the X-axis. The feed rates considered are the same as those in the case of single-axis movement.

In the case of a multi-axis movement, the run time for both axes remains the same irrespective of their movement length. For example, if it requires x mm movement along the X axis and y mm movement along the Y axis, the individual movements would take the same amount of time. However, the distance traveled for the movement would be $\sqrt{x^2 + y^2}$, and the time needed for the movement will be distance/ max feed. The effective feed rates along the X and Y axes will be

$$feed_x = \frac{(abs(x_2 - x_1)) \cdot rated_feed}{\sqrt{(x_2 - x_1)^2 + (y_2 - y_1)^2}} \tag{4.7}$$

And

$$feed_y = \frac{(abs(y_2 - y_1)) \cdot ratedfeed}{\sqrt{(x_2 - x_1)^2 + (y_2 - y_1)^2}} \tag{4.8}$$

Here, (x_2, y_2) is target co-ordinate and (x_1, y_1) is the origin co-ordinate. $ratedfeed$ is the feed rate stated in the G-code.

The following cases compare the actual and predicted scenarios for movement along the X-Y plane.

4.5.1.2.1 Feed Rate of 300 At a feed rate of 300, the signals resemble single-axis movement in terms of accuracy. It is evident that at lower speeds, the print is close to the ideal situation.

Angle (Degree)	Time (Actual)	Time (Predicted)	**No. of Peaks**		**No. of Peaks (Predicted)**		**Acuracy (time)**	**Accuracy (Peak count)**	
			X	Y	X	Y		X	Y
15	6.00	6.00	45	11	45	11	99.98	100	100
30	5.90	5.90	40	22	40	22	100	100	100
45	5.79	5.79	31	31	31	31	100	100	100

Table 4.5: Double Axis Movement at Feed 300

4.5.1.2.2 Feed Rate of 600 At a feed rate of 600, the signal accuracy is similar to that of 300. The feed rate of 600 is often used to print objects with the highest speed.

Angle (Degree)	Time (Actual)	Time (Predicted)	**No. of Peaks**		**No. of Peaks (Predicted)**		**Acuracy (time)**	**Accuracy (Peak count)**	
			X	Y	X	Y		X	Y
15	3.00	3.00	45	11	45	11	100	100	100
30	2.96	2.96	40	22	40	22	100	100	1000
45	2.90	2.90	31	31	31	31	100	100	100

Table 4.6: Double Axis Movement at Feed 600

4.5.1.2.3 Feed Rate of 2000 A feed rate of 2000 falls into the territory of ‘G0’ commands. movements at these speeds are not ideal for extruding materials at that high speed. However, even at this speed, the accuracy is good.

Angle (Degree)	Time (Actual)	Time (Predicted)	**No. of Peaks**		**No. of Peaks (Predicted)**		**Acuracy (time)**	**Accuracy (Peak count)**	
			X	Y	X	Y		X	Y
15	0.94	0.94	45	11	45	11	99.87	100	100
30	0.92	0.93	40	22	40	22	99.92	100	100
45	0.91	0.91	31	31	31	31	99.72	100	100

Table 4.7: Double Axis Movement at Feed 2000

4.5.1.2.4 Feed Rate of 6000 A feed rate of 6000 is only seen for moving objects at longer distances. This speed resulted in one of the lower accuracies in our study.

Angle (Degree)	Time (Actual)	Time (Predicted)	No. of Peaks		No. of Peaks (Predicted)		Acuracy (time)	Accuracy (Peak count)	
			X	Y	X	Y		X	Y
15	0.48	0.48	45	11	45	11	99.79	100	100
30	0.47	0.47	40	22	40	22	99.80	100	100
45	0.46	0.45	31	31	31	31	98.42	100	100

Table 4.8: Double Axis Movement at Feed 6000

4.5.1.2.5 Observations One thing that is common in all these cases is that, at 45 degrees, the X and Y axes are identical. This is consistent with the fact that at a 45-degree angle with the X axis, the X and Y components will be equal. Similarly, if a similar study was carried out at a 60-degree angle with the X-axis, the result obtained would be similar to the one found in the case with a 30-degree angle with the X-axis, with only the axes switching place.

4.5.2 Curves

The printer used in this study uses relative motions of the X and Y axes to create curvatures. The curvatures are combinations of multiple small straight lines. Depending upon the quality requirement, the number of straight lines can be increased or decreased. In this section, the properties of circular, elliptical, and irregular shapes are studied. The circle is with diamter 20mm, the ellipse has major axis of 20mm and minor axis of 10mm, the irregular shape resemles the shape of an amoeba. Since smaller feed rates are needed for the smooth printing of curves, only the feed rate of 300 is used in this study. Table 4.9 summarizes the study of curves.

In the case of a circle, the number of peaks along X and Y should be the same due to the inherent property of circles. However, the printer prints in such a way that after printing half of the circle, the printhead travels moves along X axis and prints the other half. These extra steps make the number of peaks along the X and Y axis different. Similar behavior happens in the case of the ellipse and the irregular shape, but the circle has the most prominent deviation. It is

Shape	Time (Actual), S	Time (Predicted), S	**No. of Peaks**		**No. of Peaks (Predicted)**		**Acuracy (time)**	**Accuracy (Peak count)**	
			X	Y	X	Y		X	Y
Circle	13.70	13.60	191	131	190	130	99.27	99.47	99.23
Ellipse	10.55	10.48	149	81	148	81	99.33	99.33	100
Irregular	33.04	32.78	671	570	669	568	99.21	99.70	99.33

Table 4.9: Study of Curves at Feed 300

possible to manually code the circle so that the number of peaks along both the X and Y axis remains the same.

4.6 Discussion

The first segment of the study covered movements along a single axis and along a plane. The feeds considered in this study can be divided into 2, printing feed and moving feed. A feed of 300 is more common when the 'Best Quality' preset is chosen. A feed of 600 is more common for printing that is more concerned about time. The results show that both these feed rates have very high accuracy. This means their behavior matches an expected behavior. This property is needed to ensure that products have acceptable quality. The other feed rates used in this study are mainly used for rapid movement. A feed of 2000 is more often used for rapid movement while printing. A feed rate of 6000, however, is more for moving longer distances, moving to the home position after movements, or other steps where quality is not an issue. These feed rates are not considered suitable for quality prints. Our research shows that the accuracies of movements with these feed rates are somewhat less than that of the printing feed rates.

The second segment of the study discussed movement along curves. In this particular model of printer, movement along curves is represented as movement along very small straight lines. Since the machine prefers to use a low feed rate of around 300, this section of the study only covers one feed rate. The object under study had a wide range of data points in it. Irrespective of number of data or time, the accuracy remains similar throughout the cases. One observation is a slightly different number of peaks between the actual and simulated number of peaks. The peak detection algorithm is discussed in a later section.

4.7 Conclusion

FDM printers generally produce products of acceptable quality, with stepper motors playing a crucial role in ensuring their accuracy. The 3D printer used in this research has various quality settings, where higher target quality necessitates lower feed rates and layer heights. This correlation is evident in our findings. At feed rates of 300 and 600, the mean time required for movements closely matches the expected time. However, as speed increases, the mean time deviates more significantly from the expected time, illustrating why products printed at lower speeds tend to have smoother and more reproducible results. Despite the lower accuracy at higher speeds, it remains above 99%, which ensures the final product is still of acceptable quality. For more complex movements, such as curves, the machine automatically reduces the feed rate regardless of the settings. These curved movements are essentially a series of very small straight-line movements. Thus, the principles behind simulating time and peaks are similar. Nevertheless, even at the low feed rate of 300, the accuracy of movements along curves is significantly lower compared to straight-line movements at the same feed rate.

Chapter 5

Creating a General Framework for Power Signal Simulation

5.1 Introduction

One of the major selling points of additive manufacturing is the ability to create complex designs. Thanks to additive manufacturing, sophisticated parts like jet engine fuel nozzles and human prosthetics are manufactured with much less complexity. A sabotage attack in such cases can be detrimental to product quality and very hard to figure out. Thus, prior knowledge about possible current signatures can help assess the quality issues. While Chapter 4 of the dissertation addresses current signatures in the case of individual movements, this chapter is dedicated to creating a framework to simulate current profiles for any complex shape. Additionally, this chapter closes with case studies of complex designs and their simulated current signatures.

5.2 Methodology

The process of simulating the power draw profile involves extracting the required pieces of information from the provided G-code file, constructing sinusoidal waves for each bit of information, and combining the sinusoids together. The steps are discussed in the following sections.

5.2.1 Information Extraction

In order to understand the set of G-code commands used in this model of 3D printer, different commonly used complex models are printed using the default setup. The models printed for this study are 3DBenchy (a benchmark print), Stanford Bunny, and rock2pus (the logo of the printer brand). The objects are sliced using Cura Lulzbot edition, and the unique G-code commands are studied. Table 5.1 lists the different codes in the order they arrive in a typical G-code

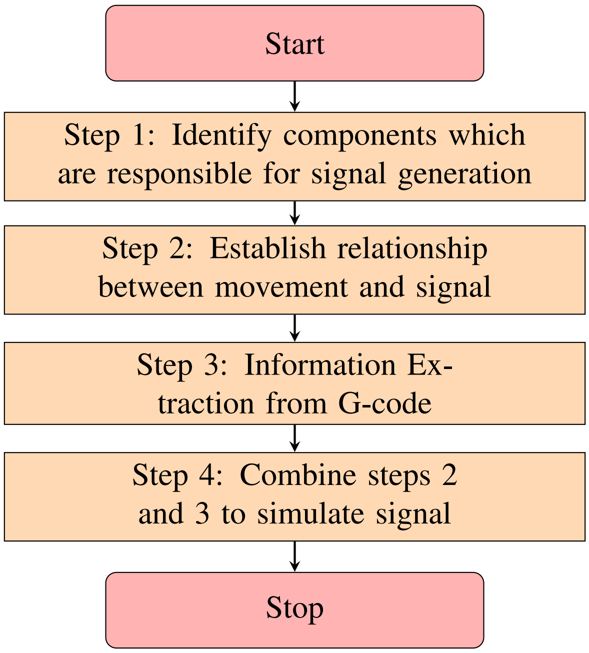

Figure 5.1: Simulation Model

command and if they have any impact on the signal generation steps. The entries with * show the commands that can impact the signal, but in practice, they were not modified in any print by the slicer.

(a) 3DBenchy (b) Stanford Bunny (c) Rock2pus

Figure 5.2: Objects Studied for G-code Commands

The G-code file used for the typical FDM process includes different types of commands, ranging from movement, temperature, fan speed adjustment, and many more. The parameters used in G-code are in millimeters(mm) by default. Among all the commands, however, only a handful are involved with stepper motors. The first step in the simulation process is to extract the information associated with stepper motors. The types of information extracted for this particular printer are:

Code	Description	Required for signal generation
M82	Absolute extrusion mode	yes
M92	Steps-per-unit	No*
M301	Set hot-end PID	No
M906	Stepper motor current	Yes
M206	Set home offset	No
M73	Clear progress bar	No
M75	Start timer	No
G26	Clear probe-fail condition	No
M107	Disable fans	No
M420	Clear previous levelling matrix	No
G90	Absolute positioning	Yes
G92	Set position (X/Y/Z/E)	No
M140	Print bed heating	No
M109	Soften filament	No
G28	Home all axis	No
G0	Linear movement (non-print)	Yes
G1	Linear movement (print)	Yes
G12	Nozzle wiping	No
M204	Probing acceleration	No
M420	Bed level matrix	No
M117	Message display	No
M109	Wait until set nozzle temperature	No
M190	Wait until set bed temperature	No
M221	Set flow percentage	No
M400	Wait for moves to finish	No
G91	Relative positioning	Yes

Table 5.1: G-code Commands and Their Impact on Signal Generation

5.2.1.1 Go Commands

These commands are associated with movements. A G0 command asks for rapid movement, while a G1 asks for slow movement. Mostly G1 is associated with actual material extrusion. G0 is mostly associated with moving the extruder or the base plate without extruding any material. In some different printers, there might be codes G2/G3, which means circular movement, or G5, which denotes cubic splines.

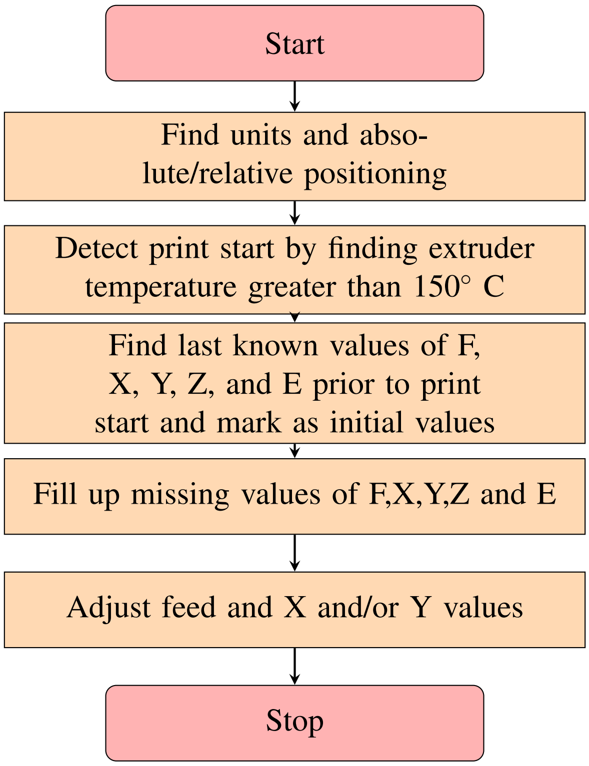

Figure 5.3: Information Extraction from G-code

5.2.1.2 Feed Rate

Feed rate is expressed as the letter "F" followed by the feed rate in number. One such example is "F600". If a feed rate is not specified in a particular line of code, the last known feed rate will be maintained. The feed rate, however, needs to be adjusted based on the ratio of distances covered by the X and the Y axis. Even though the printer used in this research can move each axis independently, it will not do so. In order to attain a smooth straight line between two consecutive commands, one axis might have to move slower than the other. It will result in a much lower actual velocity along that axis. In the previous example, the movement will have a speed equal to the stated maximum feed rate, while the maximum movement speed of the X and Y axes follow Equations 4.7 and 4.8, respectively

5.2.1.3 Absolute or Relative Positioning

There are two types of positioning systems used in such G-codes: absolute and relative. The code G90 denotes the absolute positioning system, while G91 denotes relative positioning. The change point between the types of positioning systems is to be traced.

5.2.1.4 Movements Along Axes

Movements and positions are signified by the letter representing axes (X, Y, or Z) followed by the coordinate. Examples of such positions are “X2”, “Y-3”, and “Z4”. Here a negative sign denotes movement in the opposite direction. In the case of absolute positioning, the numbers denote their position. If relative positioning is used, the numbers signify movement along that axis. In case of no mention of either of the “X”, “Y”, or “Z” values, their last known value is passed to the current line.

5.2.1.5 Extrusion

Extrusion of the material is denoted by the letter “E”, followed by the filament extrusion length. In G-code, the E axis describes the position of the filament in terms of input to the extruder feeder. A negative number followed by “E” denotes that material is taken upward instead of actually extruding.

5.2.1.6 Miscellaneous

Other commands include “G28” for auto homing and “G29” for bed leveling. These codes are machine-specific and consist of complex move-sets. There are codes for setting up temperatures that have nothing to do with the stepper motors, but they create a period of idle time for the motors. In this study, the codes to change temperature (M104, M109) are used to create partitions to match the actual print.

The pseudocode is referred to in Algorithm 1. In this case, the original G-code information is first read. Line 5 talks about selecting a trigger point for data extraction. This can be any segment of the G-code that denotes the actual print start. For this study, we choose nozzle temperature. The code for setting the nozzle temperature is M109, followed by R and the temperature. The materials suitable for printing in this printer are 190 degrees Celsius at the lowest. This temperature is chosen as our trigger point. The next step, as shown in lines 6 to 18, is to find the lines that contain ‘G0’, ‘G1’, ‘G91’, and‘G90’. Remove comments if any exist and save the file as an ‘intermediate file.’ Lines 20 to 40 talk about writing the information into

Algorithm 1 G-code Information Extraction

```
Read G-code from input file
Read all lines into a list gcode.
Process G-code and write to intermediate file
Open intermediate.txt for appending.
Find the line starting with "M109" followed by the letter "R" followed by a number greater than 190. Call this line initiation.
for each line in gcode do
    if current line index is greater than the index of initiation then
        Replace tab characters with spaces in the current line.
        if line starts with "G1", "G0", "G90",or "G91" then
            if line contains a semicolon then
                Split the line at the semicolon.
                Write the part before the semicolon to intermediate.txt.
            else
                Write the whole line to intermediate.txt.
            end if
        end if
    end if
end for
Read processed G-code from intermediate file
Open intermediate.txt for reading.
Read all lines into a list cleaned.
Initialize previous F, X, Y, Z values
Split the first line of cleaned and extract values followed by the letters F, X, Y, Z, and E.
Handle output file
if output_file_name exists then
    Delete it.
else
    Create and open it for writing.
end if
Write processed G-code to output file
Open output_file_name for appending.
Write the header "G F X Y Z" to the file.
for each line in cleaned do
    Split the line into a list m.
    for each element in m do
        Update previous F, X, Y, Z values if the element starts with "F", "X", "Y", or "Z".
    end for
    Write the updated line to the output file.
end for
Save differences to CSV file
Track "G90" and "G91".
if "G90" precedes the present line then
    Write the difference between consecutive lines to csv_file.
else
    Write the actual value to csv_file.
end if
```

a 'CSV' file. First, column headers are made with 'G', 'F','X', 'Y', 'Z' and 'E'. Their last known values are recorded. Next, each line of the 'intermediate' file is looped through, and only the numbers followed by the respective column headers are extracted. If any line does not have a value for any of the column headers, their last known value is updated as the new value. Lines from 41 work with the positioning system. In case the absolute positioning system is used, the difference between rows for 'X,' ' Y,' ' Z', and 'E' values are recorded. If not, they are kept as they appear on the G-code.

Figure 5.4 code shows a sample G-code file sliced by the CURA software, while Figure 5.5 shows a general G-code information extracted file.

5.2.2 Signal Generation

The signal generation step involves calculating and appending the amplitude, frequency, and time duration of the wave to the G-code extracted file, profiling the residual current, and combining all the information together. The following sections discuss the process in detail.

5.2.2.1 Amplitude

The rated current of the motors is 1.5 Ampere. However, experiments showed amplitudes of around 1.35 Ampere. For a feed rate lower than 600, the amplitude lowers slightly and ends up being around 1.25 Amperes at a feed rate of 100 and lower. Table 5.2 shows the mean amplitude at different feed rates. In this study, customized G-code commands were written to move the X-axis by 100mm, and each data set was repeated 10 times. In the signal generation step, for feed more than 600, the amplitude is taken as 1.35. For an amplitude between 600 and 100, interpolation is used, and for an amplitude under 100, it is taken as 1.25A. An ideal signal would have its mean around 0; a real signal, on the other hand, has a deviation in mean. This deviation of the mean is a random phenomenon. Thus, in this study, the mean is considered to be zero.

```
;Generated by Cura LulzBot Edition GCodeWriter Version: 3.6.37
;FLAVOR:Marlin
;TIME:569
;Filament used: 0.11578m
;Layer height: 0.25
;Generated with Cura_SteamEngine 3.6.37-win10
M82 ;absolute extrusion mode
;This G-Code has been generated specifically for the LulzBot TAZ
;
;The following lines can be uncommented for printer specific fine
;More information can be found at https://marlinfw.org/meta/gcode
;
;M92 E833                  ;Set Axis Steps-per-unit
;M301 P21.0 I1.78 D61.93   ;Set Hotend PID
;M906 E135                 ;Digipot Motor Current ((750mA-750)/5+1
;M206 Y4                   ;Set Home Offsets (default:4)
;
M73 P0 ; clear GLCD progress bar
M75 ; start GLCD timer
G26 ; clear potential 'probe fail' condition
M107 ; disable fans
M420 S0 ; disable previous leveling matrix
G90 ; absolute positioning
M82 ; set extruder to absolute mode
G92 E0 ; set extruder position to 0
M140 S60.0 ; start bed heating up
M109 R140 ; soften filament before homing Z
G28 ; Home all axis
G1 E-15 F100 ; retract filament
M109 R140                   ; wait for extruder to reach wiping te
;M206 X0 Y0 Z0               ; uncomment to adjust wipe position (
forward)(+Z ~ nozzle moves down)
G12                          ; wiping sequence
M206 X0 Y4 Z0                ; reseting stock nozzle position ###
quality ###
M109 R140 ; wait for extruder to reach probe temp
G1 X-10 Y293 F4000 ; move above first probe point
M204 S100 ; set probing acceleration
```

Figure 5.4: Sample G-code

5.2.2.2 Time

One of the important aspects of the simulation process is calculating the time required to complete the movement. In general, such motions have a component of acceleration and deceleration in them. When extruding material, a lower feed rate is usually used to maintain

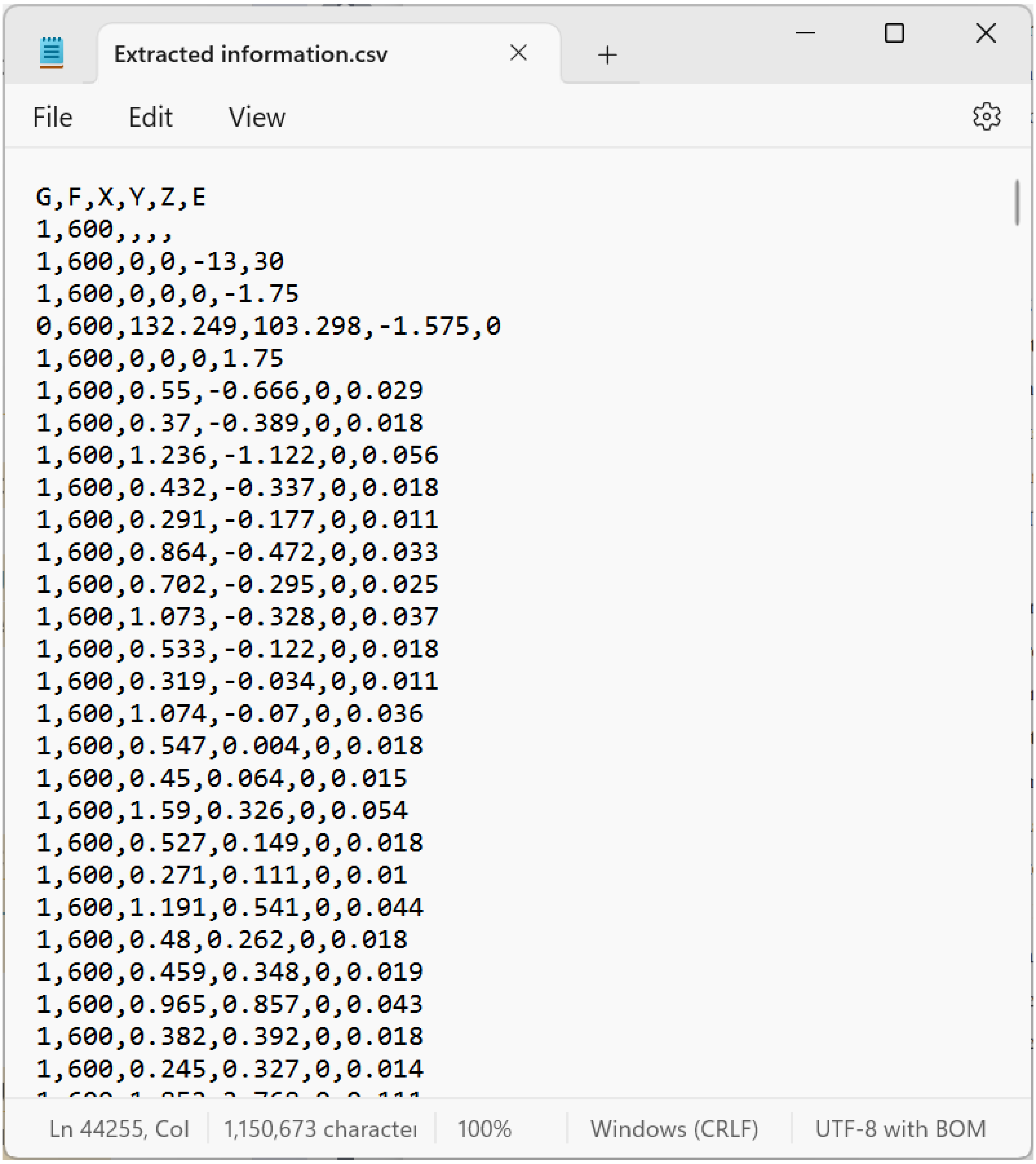

Figure 5.5: Sample Data Extraction from G-code

consistency in product quality. In such cases, the stages of acceleration, moving at the highest speed and deceleration, are not prominent. The time required to perform such movements is $Distance/feed$. The same can not be said for a high feed rate. These are often associated with high acceleration, a period of constant speed, and deceleration. The time required to complete such movements is the summation of time of acceleration, deceleration, and movement at uniform speed.

Feed	Mean amplitude (A)
100	1.25
200	1.32
300	1.33
600	1.35
1200	1.34
1500	1.35
1800	1.35

Table 5.2: Mean Amplitude at Different Feed Rate

Study shows that in such cases, the time to accelerate and decelerate is equal. If the maximum acceleration is denoted by a. In order to find the total time of travel, the maximum acceleration of the motors must be determined. The maximum possible feed rate of this machine,18000, is used to find the maximum possible value of a. If time T is needed for a movement of S, a can be calculated by solving the following equation 5.1,

$$T = \frac{2 \cdot feed}{a} + \frac{S - \frac{feed^2}{a}}{feed} \tag{5.1}$$

Once the maximum acceleration is figured out, the equation 5.1 can be used to the time needed to perform any movement at a given rate. The G-code works one line at a time. Thus, all the commands in a line will take the same amount of time to complete.

5.2.2.3 Frequency

The frequency of the wave is the single most critical component of this wave. Frequency can be obtained by dividing the velocity by wavelength. Gatlin et al. noted that a full wave is represented by a single-step movement [46]. For the stepper motor used in the Lulzbot Taz 6 printer, the step size is 1.8 degrees. Since every unit of movement produces the same number of waves, a higher feed rate results in a higher frequency. For a given feed rate of 600 mm/min, the wavelength is measured by a few trial runs. A feed rate of 600 is used since this is more common than any other feed rates used in printing straight lines in the default settings of the Cura software. The data of these trial runs were denoised using a wavelet transformation. It was then decomposed into the frequency domain by using the Fast Fourier Transform (FFT).

Feed	Frequency (Hz)
300	7.85
600	15.69
1200	31.38
1500	39.23
2000	52.38
6000	156.9

Table 5.3: Frequency at Different Feed Rate

The frequency obtained this way is used as the base wavelength of a feed rate of 600. With a change in feed rate, the wavelengths change proportionally. The best fit of frequency for a feed rate of 600 is found to be 15.69 Hz. At this particular frequency, the distances between the original printed and simulated graphs are the smallest. For any feed rate that is not 600, the frequency is simply implied by 15.69 times the ratio between the said feed rate and 600.

5.2.2.4 Addressing Residual Current

Once the motor is stopped while running, there is still some residual current in the wire. It takes time for the residual current to be zero. In order to have a good simulation of the power draw profile, it is important to understand the nature of the residual current. For this, similar sections appearing in our study are studied to determine how long the residual current takes to be zero. These data are curve fitted in MATLAB to find an equation of residual current.

5.2.2.5 Finalizing the Simulation

The simulation is done using the "dsp" package of MATLAB. This package is utilized for digital signal processing. The simulation is done using a sampling frequency of 1000 Hz. Here, each individual axis is simulated separately and combined to produce the final output. There will be instances where a particular line will have a particular axis that does not move. In such cases, the maximum time needed for any axis for that line will be termed as the time needed for that axis. The first step in simulating is to check if the initial movement is zero; an initial movement of zero would result in a flat line consisting of data points equal to the time needed to perform any movement specified by that time. For any non-zero movement, a sine wave is to be generated with the amplitude and frequency. The total number of samples is equal to the time in milliseconds rounded to the nearest integer. For objects with “G0” or rapid movement, based on the feed rate, there can be multiple sine waves to represent acceleration, deceleration, and no-acceleration movements. The sine wave is offset if needed to merge with the nearest sine waves. In case of a change in the direction shown in the G-code, the sine waves are offset so that the next sine wave moves in the opposite direction. Algorithm 2 describes the steps of simulating the signal.

Algorithm 2 Signal Generation

```
Read data from data file into the variable data.
Extract specific columns from data: Distance as ‘S‘, Time as ‘T‘, Amplitude as ‘A‘, Frequency as ‘F‘
Initialize non_zero with the first element of ‘x‘.
Initialize out array with zero.
for each element i from the second to the end of ‘x‘ do
    if current element is zero then
        Set flag to 0.
    else if previous element is zero then
        if product of current element and non_zero is negative then
            Set flag to 1.
        end if
        Update non_zero to current element.
    else if product of current and previous element is negative then
        Set flag to 1.
    else
        Set flag to 0.
    end if
    Update out with flag.
end for
Initialize final output waveform:
if the first element of ‘x‘ is zero then
    Set finale to an array of zeros with length T(1).
else
    Generate a sine wave a1 with parameters A(1) and F(1), and store it in finale.
    Set p1 and p2 to the last two elements of finale.
end if
Modify waveform based on direction and motor on/off status, append steps:
```

```
for each element i from the second to the third last element of 'x' do
    if current element is zero then
        Set flag to 0.
        if the last element of finale is positive then
            Calculate y_fit and y_fit_2 using polynomial yy.
            Generate a3 using polynomial zz.
        else
            Calculate y_fit and y_fit_2 using absolute value.
            Generate a3 using polynomial zz.
        end if
    else
        if no sign change (out(i) == 0) then
            if p1 equals the last element of finale then
                Generate sine wave a2 based on the sign and values of p1 and p2.
                Generate a3 and update a3.
            else
                Generate sine wave a2 based on the sign and values of p1 and p2.
                Calculate a4, a5, and a6 using polynomial yy and zz.
                Update a3 with a6.
            end if
        else
            if p1 equals the last element of finale then
                Generate sine wave a2 based on the sign and values of p1 and p2.
                Update a3 with sine wave a2.
            else
                Generate sine wave a2 based on the sign and values of p1 and p2.
                Calculate a4, a5, and a6 using polynomial yy and zz.
                Update a3 with a6.
            end if
        end if
    end if
    Update p1 and p2 with the last two elements of a3.
    Append a3 to finale.
end for
Plot final waveform:
Plot finale.
```

As shown in Algorithm 2 the process of simulating the signal involves multiple steps. The columns for calculated distance, time, frequency, and amplitude are added to the file with extracted G-code information. The file is named “data”. Steps 3-18 discuss the detection of directional change. The variable is set as ‘flag’. This tracks changes in movement along any axis from positive to negative. Zero is not considered a change in direction. The next step talks about structuring the signal. Lines 22-26 talk about creating the first portion of the signal representing the first line of the ‘data’ file. If the first has a movement of zero along that axis, the resulting signal will be a set of zeros along the duration of movement of the other axis. For movement of any other length, a sine wave is produced with the said frequency and amplitude. The last two data points are recorded to see the trend of data if it is going up or down.

The next steps are to create signal segments with the calculated amplitude, frequency, and time. However, the initial phase is determined by the last two points of the previous signal segment. For no change in direction, the last two points of the previous segment work as the initial phase of the new signal. The new segment is made to follow the path of the previous segment. If there is a change in direction, the new segment is made to move the other way. In case of a value of zero as the distance, the signal segment is made to merge to 0 A, if it reaches to 0 A, the next points remain on 0 until a new length of movement is ordered. This curve is done by doing a polynomial fit of the second degree. For a segment following zero, it has to keep track of the last known phase prior to the line segment with 0 movements being ordered. For the next non-zero movement, an initial segment is generated as if there is no segment of 0 length. However, on top of that segment, the movement for the 0-length segment is added.

5.3 Case Study

The case study is divided into three types of objects: objects with predominantly straight lines, objects with circular features, and objects with irregular features and variable layers. examples of these types are rectangle, cone, and Rock2pus, respectively. Rock2pus is the logo of Lulzbot. One thing to note is that none of the prints are entirely made of the said features. The 3D printer aims to print objects with the highest quality at the least possible time. To achieve this feat, the printer prints the infill structure as straight lines irrespective of the external feature. Besides, this particular printer model represents curved paths as the summation of small straight lines. Figure 5.6 shows the objects that are under study.

(a) Rectangle (b) Cone (c) Rock2pus

Figure 5.6: CAD models for Case Study

The test objects are designed by Fusion 360 designing software and sliced by using the ”CURA - Lulzbot Edition”. The resulting G-code is taken for information extraction. The information extraction involves discarding some information, including print bed temperature, fan turn/off, display text, and others. Information like positioning system (absolute or relative) and unit system (SI or metric) are used to make the data uniform. In this research, we have used nozzle temperature as a trigger point; information extraction begins once the G-code signifies a temperature of over 190 degrees Celcius. This temperature is chosen as it is close to the operating temperature for filaments that can be used for this printer. A lower nozzle temperature would mean bad or no print at all. The extracted file includes the information on feed rate and XYZ coordinates and the material extraction. Only Go-commands (G0 and G1) are responsible for the signal generation. The type of Go commands are also included in the extracted file. There is no significant difference in how they impact signal generation, but G0 signifies a non-printing move and usually has a much higher traveling speed. However, in some cases, it is not unusual to have low speed for G0 commands. G1 commands carry out the print and are much slower while printing curved paths than longer straight-line segments. Figure 5.4 shows a typical G-code while Figure 5.5 shows sample extracted data.

The extracted information is then used to calculate the values of frequency, time, and amplitude of the signal. The values are then combined to obtain the simulated signal.

5.4 Results

In this section, the current signals of different objects are discussed. For each object, data along both the X and Y axes are compared side by side. Besides, for each object type, a section of data is zoomed in to give a better view of the signals. In the case of the cone and the Rock2pus, the data are split into layers to accommodate large datasets.

5.4.1 Rectangle

The rectangle is chosen as a representative of the simplest structure. The actual print data is captured along the X,Y, and Z axes. Figure 5.7 and 5.8 shows a comparison between actual and simulated data along the X and Y axes, respectively. The figures show a similarity between the actual and the simulated signal. The signals consist of more than four hundred thousand data points. Thus a chunk of data is taken for qualitative comparison. For comparative studies, sections of data that represent features like change in direction, dwell, and change of speed are chosen as they show more variation even for the actual prints. The black strip of data from Figure 5.8a and Figure 5.8b are zoomed in for a better study.

Figure 5.9 shows a comparison between the original and zoomed-in signals. Some zones in the graph are highlighted to show changes in speed and direction in the first area, dwelling in the second highlighted area, and change in direction in the third and fourth zones. Similar activities are observed in the simulated signal as well.

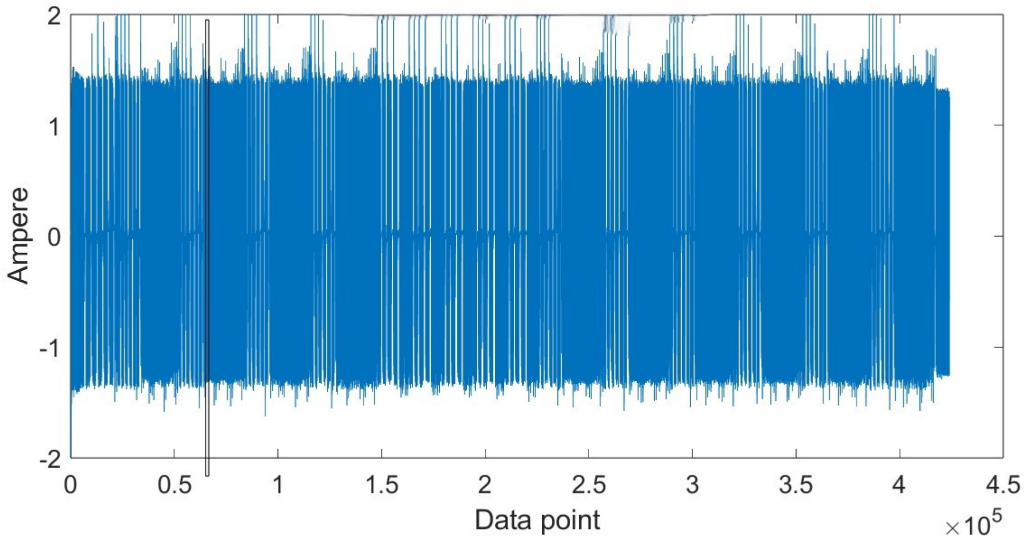

(a) Rectangle, X-axis Actual Signal

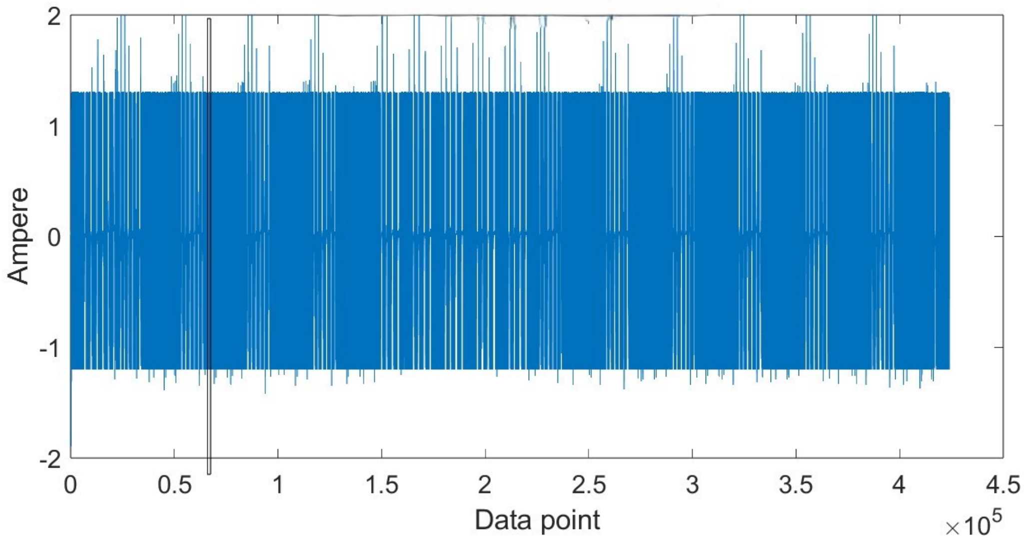

(b) Rectangle, X-axis Simulated Signal

Figure 5.7: Actual vs Simulated Signal for Rectangle Along X Axis

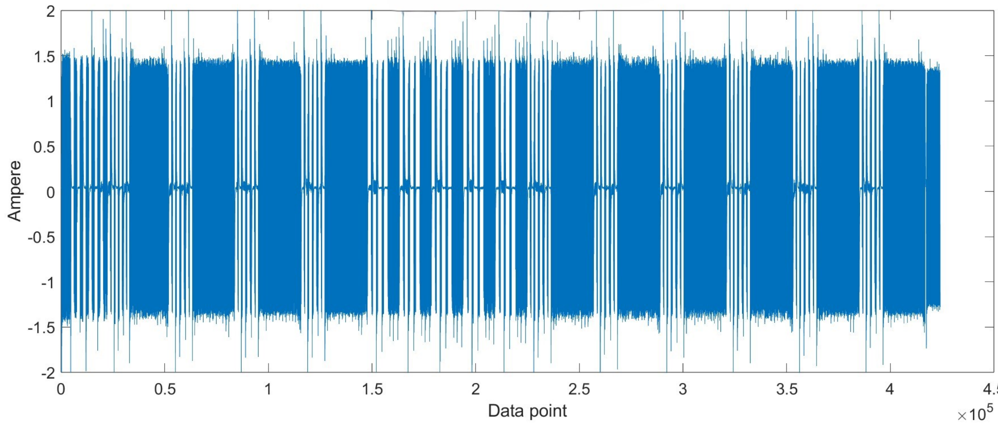

(a) Rectangle, Y-axis Actual Signal

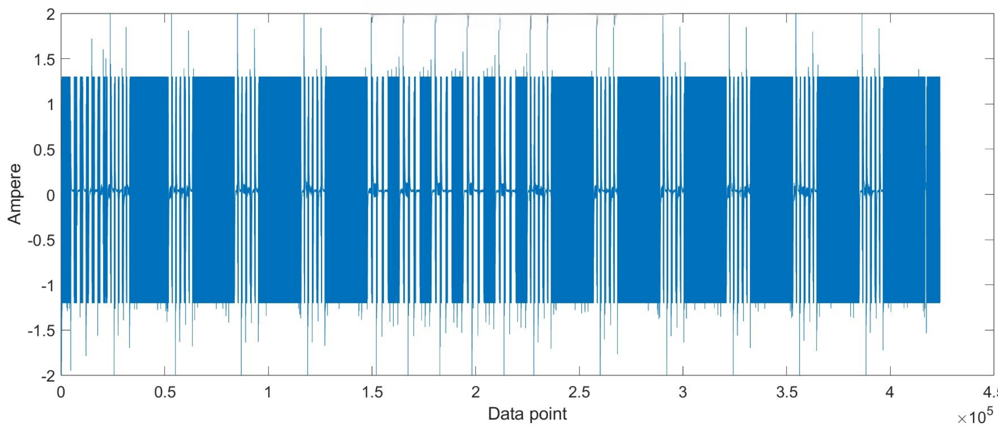

(b) Rectangle, Y-axis Simulated Signal

Figure 5.8: Actual vs Simulated Signal for Rectangle Along Y Axis

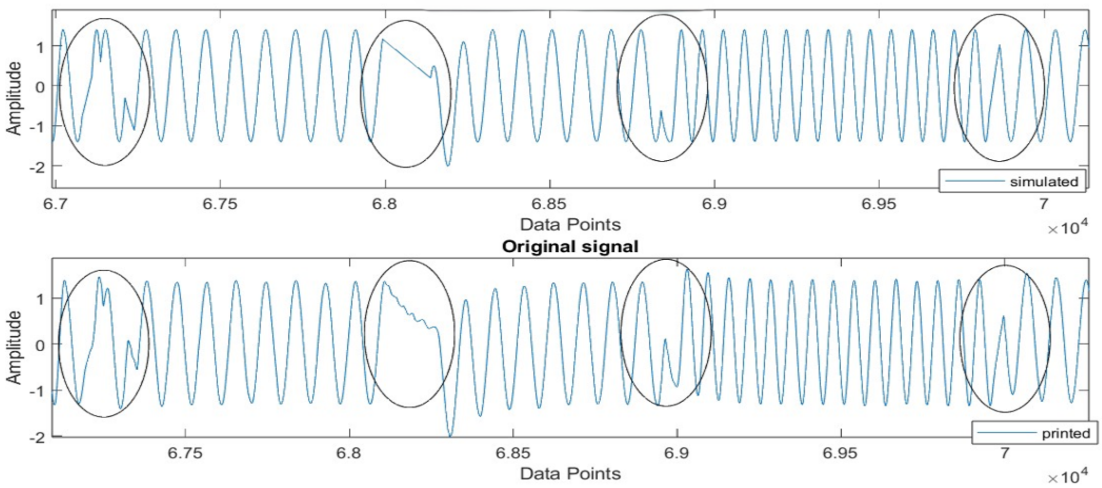

Figure 5.9: Simulated Vs Original Signal Zoomed, Rectangle Along X Axis

5.4.2 Cone

The second object under study is a cone. This object is a representative of objects with mostly circular features. The printed object, however, takes a lot longer time than the rectangle. Thus, the signals are tough to visualize. In order to better segment the object, the object is broken into layers. The process is outlined as Algorithm 3. The splitting is performed by observing a spike in the Z-axis data. During printing any layer, the Z-axis motor remains idle, resulting in a flat line in the current graph. However, a change in layer is signified by a change in peaks of the Z-axis curve. Usually, this change accompanies a flat line along the X and Y axes. During the operation, the Z-axis can occasionally exhibit unexpectedly high peaks for a short burst of time. Studies showed that such peaks are observed when the extruder head needs to move to a different position at the same height level without continuing material extrusion. Thus, a change of layer is defined when a high peak is observed along the Z-axis data for a longer duration. The exact duration and number of peaks depend on the print settings. In this study, the minimum possible print height (10 mm) denoted in the product specification is considered the minimum movement required along the Z-axis to denote a layer change. Figure 6.3 demonstrates layer segregation. In the graph, positive peaks are marked by green dots and negative peaks by red. In one case, it is observed that there is a red dot with a relatively higher current value than the idle state. This peak is considered a one-off situation here because there are not enough high peaks in close vicinity.

Algorithm 3 Layer Segregation

1: Read the source file *source* and reference signatures `start_z` and `end_z`.
2: Extract and denoise the information in different channels:
3: Apply wavelet denoising on columns 2, 3, 4, and 5 of *source* and store results in `x_1`, `y_1`, `z_1`, and `e_1` respectively.
4: Crop the signal portion for actual printing:
5: Find delay between `z_1` and `start_z`.
6: Crop `x_1`, `y_1`, `z_1`, and `e_1` to remove the portion before the actual printing using the calculated delay.
7: Find delay between `z_1` and `end_z`.
8: Extract the tail portion of `z_1` using the calculated delay.
9: Identify change points in the tail portion using RMS statistic.
10: Crop `x_1`, `y_1`, `z_1`, and `e_1` to remove the portion after the actual printing.
11: Find peaks in `z_1`:
12: Identify peaks in `z_1` with a minimum peak distance of 10 and minimum peak prominence of 1.
13: Identify negative peaks in `z_1` with a minimum peak distance of 10 and minimum peak prominence of -1.
14: Combine and sort the peak locations:
15: Combine locations of positive and negative peaks.
16: Sort the combined peak locations.
17: Identify initial Z movements:
18: Initialize `initial_z_movement` as an empty list.
19: Iterate through the combined peak locations:
20: If n peaks are found within *window* data points and the next w peaks are outside the *window* length:
21: Add the index to `initial_z_movement`.
22: Refine start points and determine end points:
23: Initialize `st` with the first value of `initial_z_movement`.
24: Iterate through `initial_z_movement`:
25: If the current value is not consecutive to the previous value:
26: Add the current value to `st`.
27: Iterate through `st`:
28: Add the maximum combined peak location within 100 data points of each start point to `en`.

Figures 5.11 to 5.14 showcase different segments of the codes and their simulated counterparts.

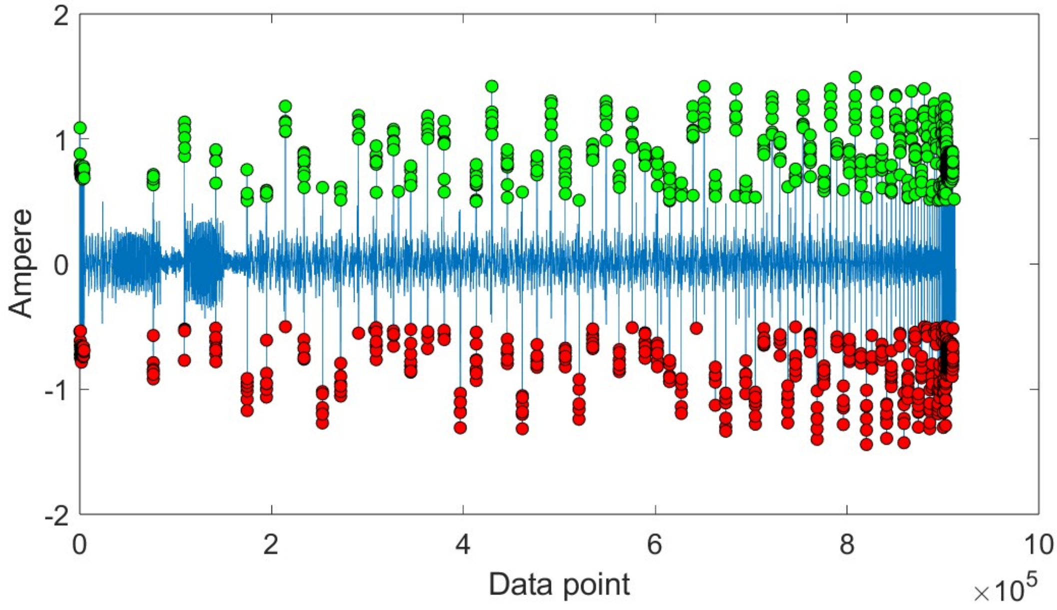

Figure 5.10: Layer Segregation for Cone

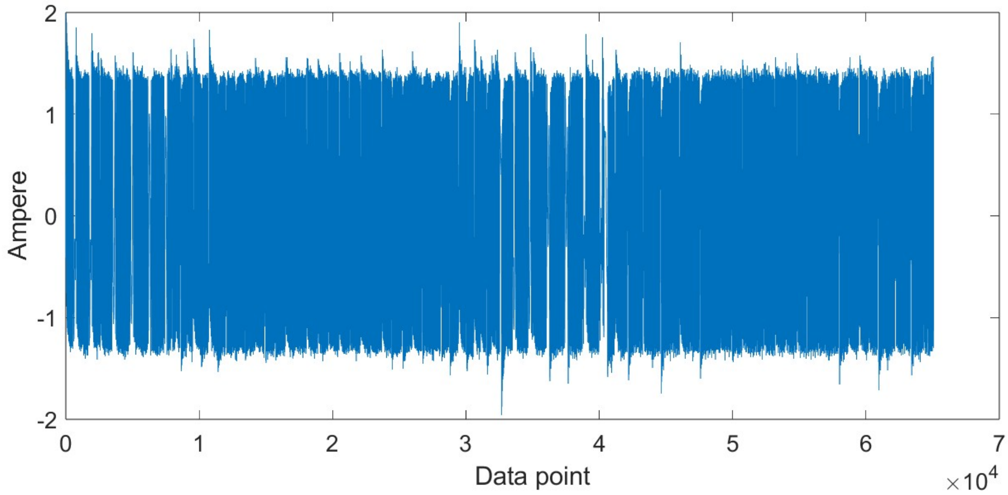

(a) Cone Actual

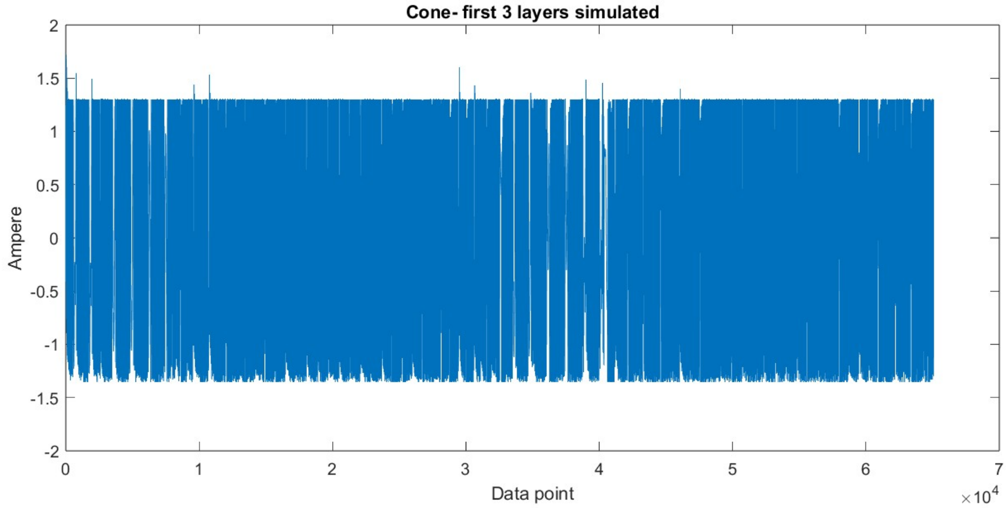

(b) Cone Simulated

Figure 5.11: Cone X Axis Signal Layers 1-3 Actual (a) vs Simulated (b)

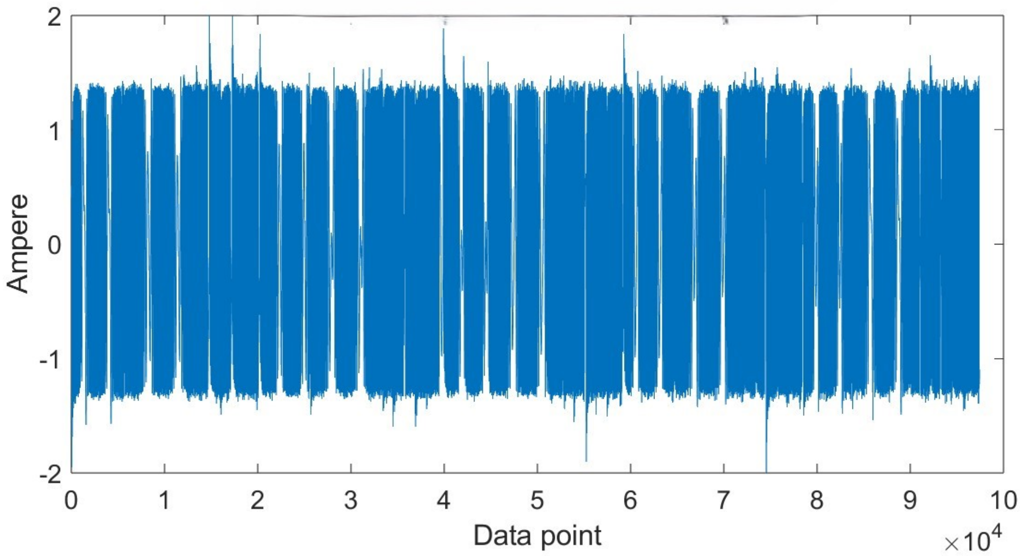

(a) Cone Actual

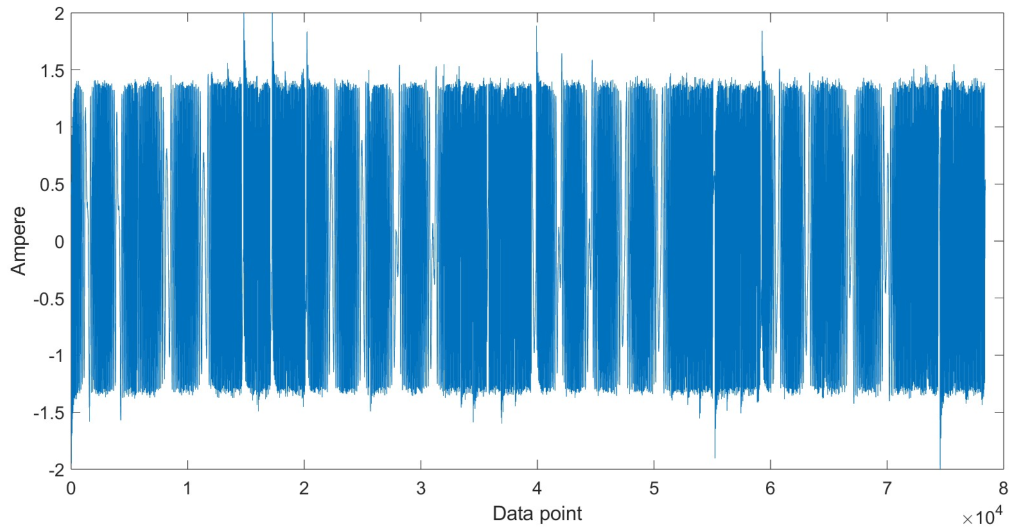

(b) Cone Simulated

Figure 5.12: Cone X Axis Signal Layers 4-8 Actual (a) vs Simulated (b)

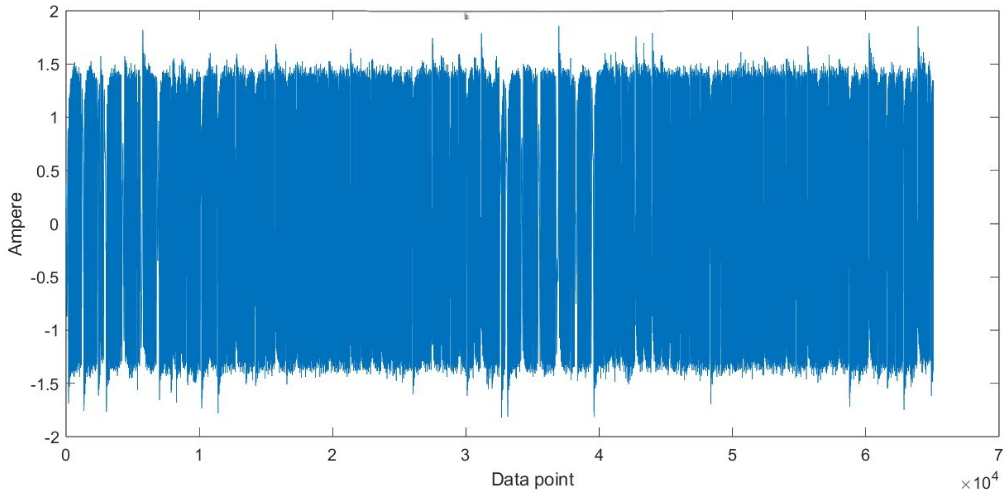

(a) Cone Actual

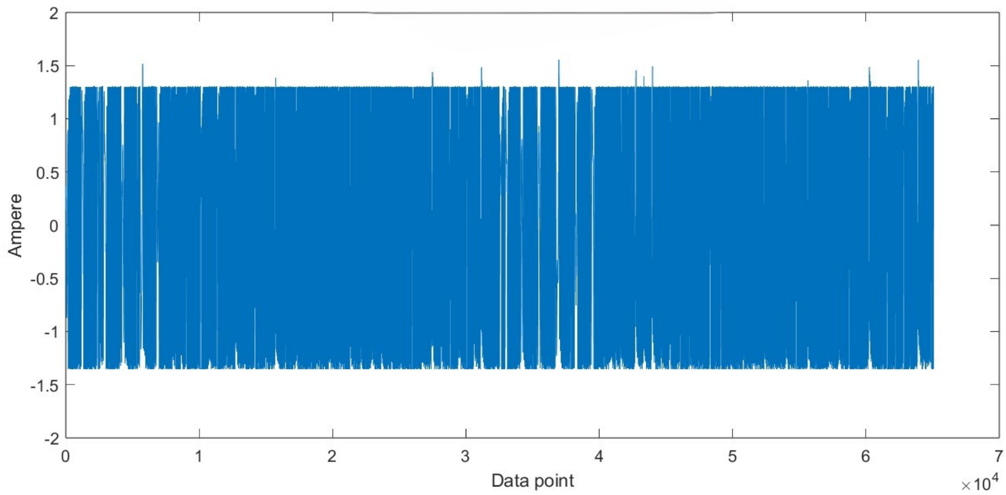

(b) Cone Simulated

Figure 5.13: Cone Y Axis Signal Layers 1-3 Actual (a) vs Simulated (b)

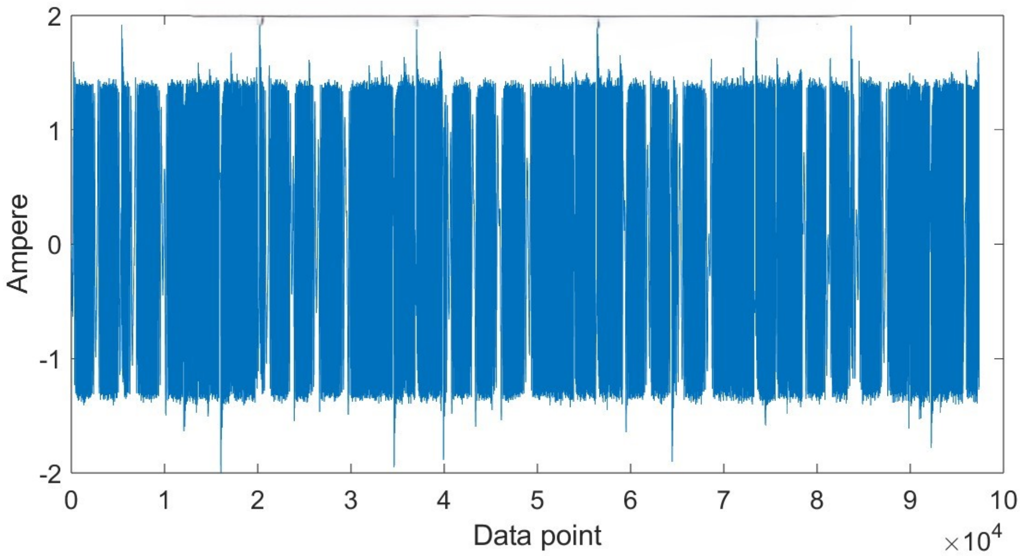

(a) Cone Actual

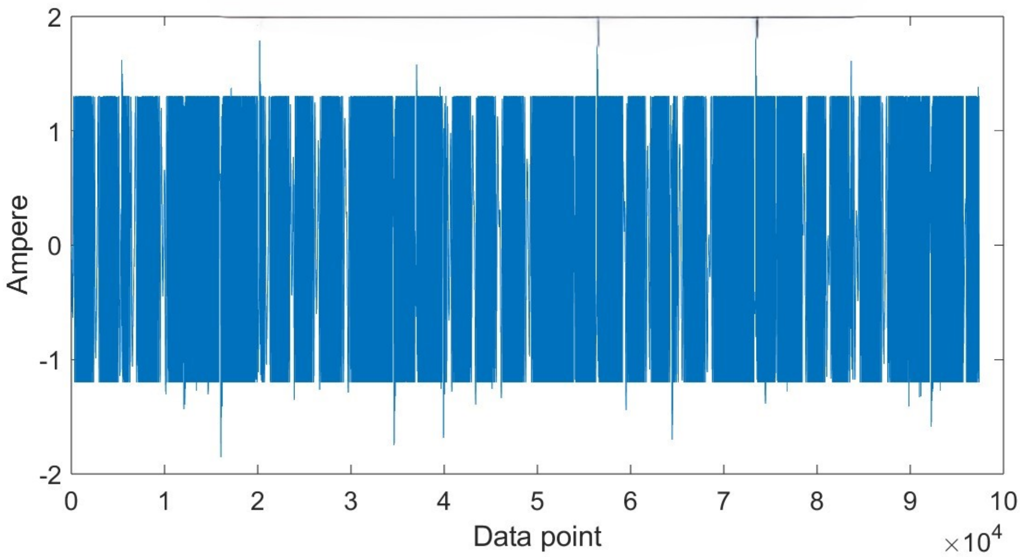

(b) Cone Simulated

Figure 5.14: Cone Y Axis Signal Layers 4-8 Actual (a) vs Simulated (b)

Figure 5.10 shows splitting the data by tracking the Z-axis movement. The original vs simulated graphs for the cone the along X axis are shown in Figures 5.11 and 5.12. The comparison along the Y channels is shown in Figures 5.13 and 5.14.

Figure 5.15 shows a comparison between the original and zoomed-in signals. The data is picked from first layer of the cone. This figure captures similar activities in both the actual and simulated signals. The activities are changes in speed, direction, and dwell.

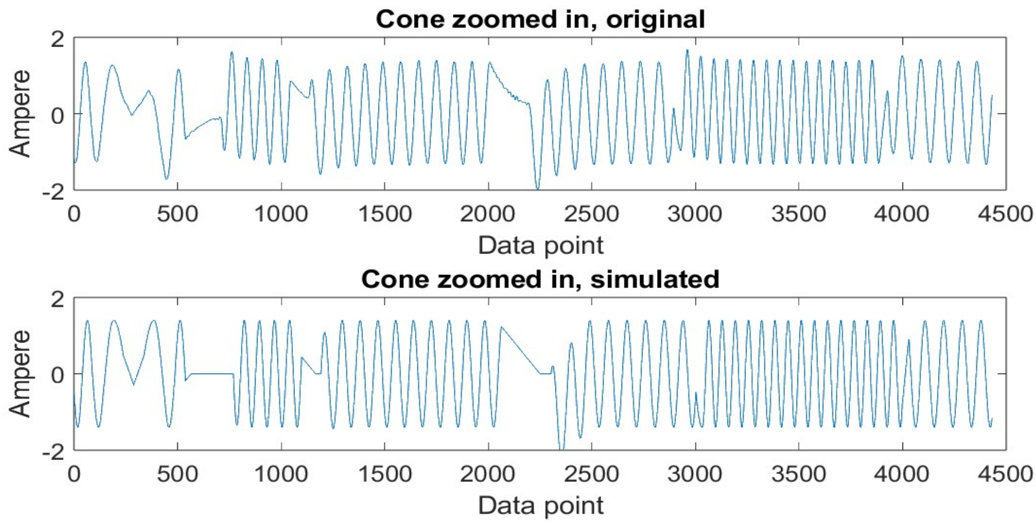

Figure 5.15: Simulated Vs Original Signal Zoomed, Cone Along X Axis

5.4.3 Rock2pus

Rock2pus is the representative of objects with the most complex features. This object consists of curved features on the external side and a straight line for building the in-fill. Moreover, each layer of the object is different from the others. Like the cone, Rock2pus is also split into sections for better visualization of the signals. The object being more complex, the results along the X axis are shown for the first five and last ten layers in Figures 5.16, 5.17, and 5.18. Figures 5.19, 5.20, and 5.21 show the results for the Y-axis.

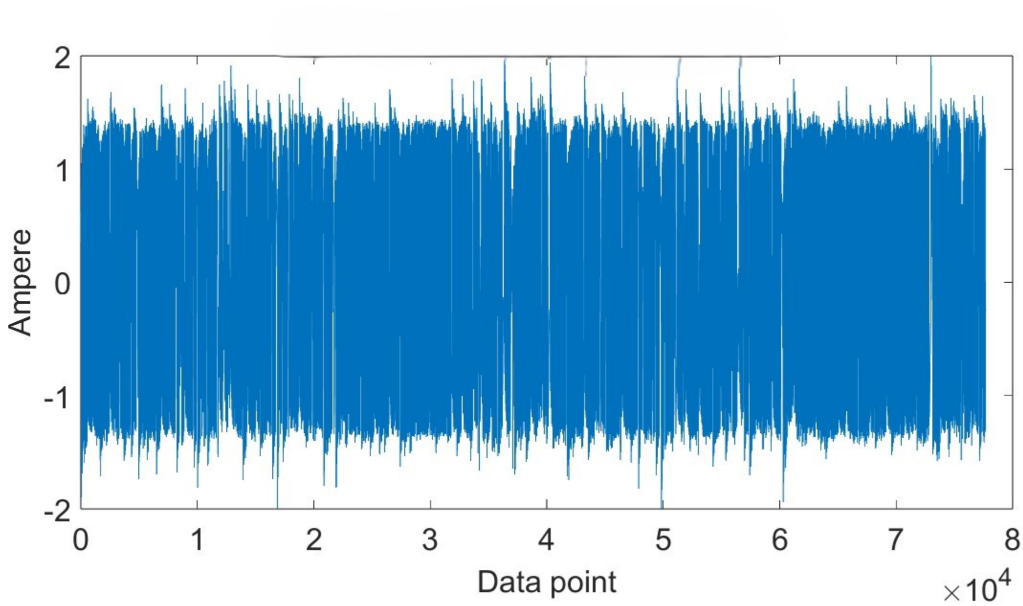

(a) Rock2pus Actual

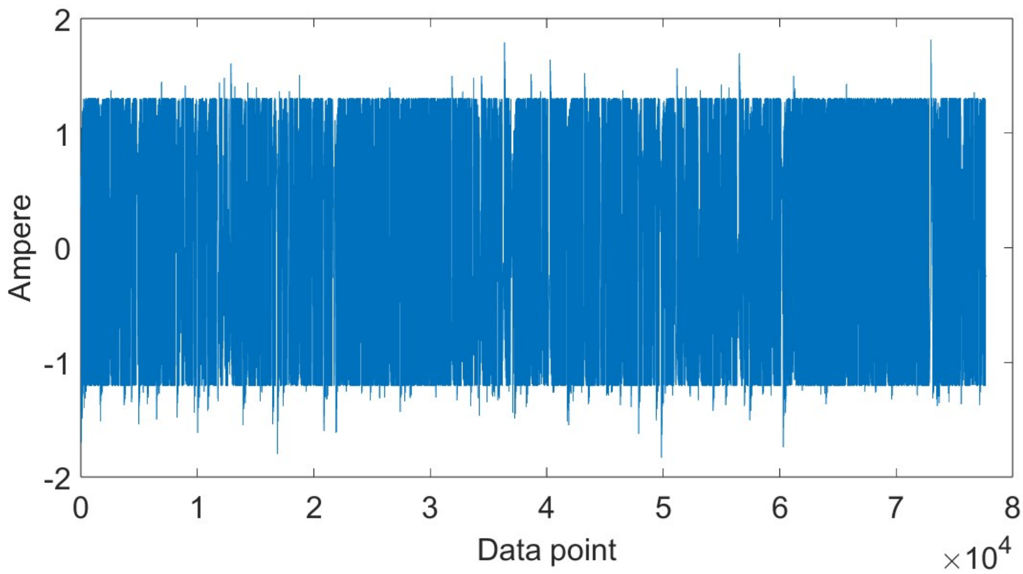

(b) Rock2pus Simulated

Figure 5.16: Rock2pus X Axis Signal Layers 1-2 Actual (a) vs Simulated (b)

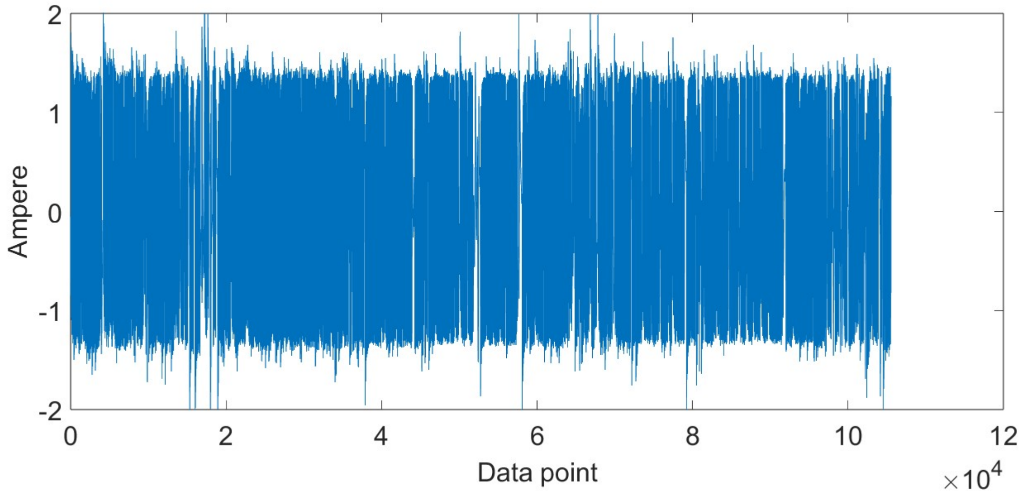

(a) Rock2pus Actual

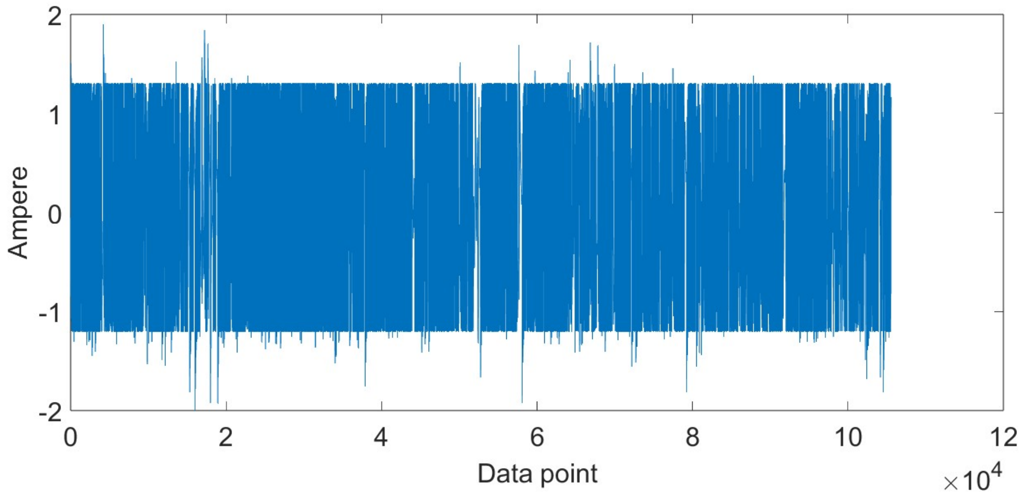

(b) Rock2pus Simulated

Figure 5.17: Rock2pus X Axis Signal Layers 3-5 Actual (a) vs Simulated (b)

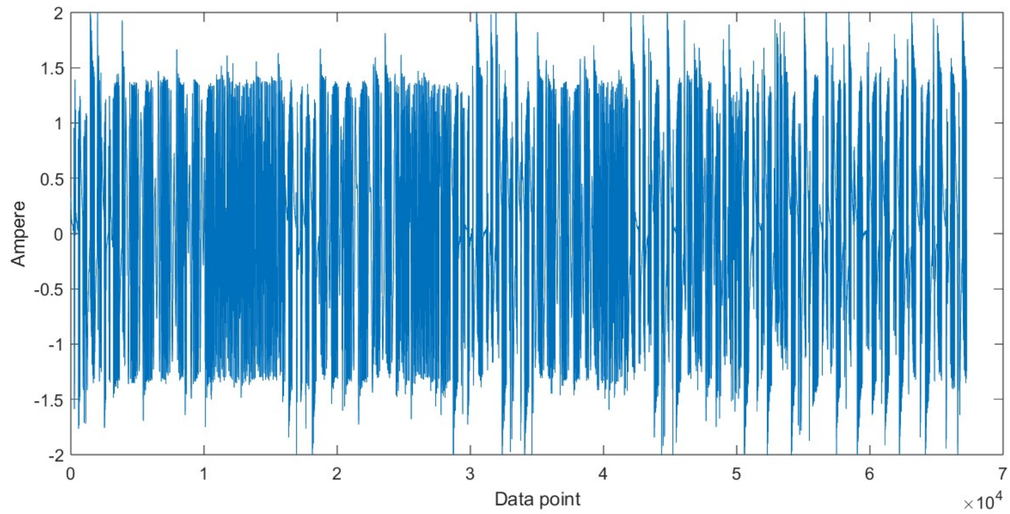

(a) Rock2pus Actual

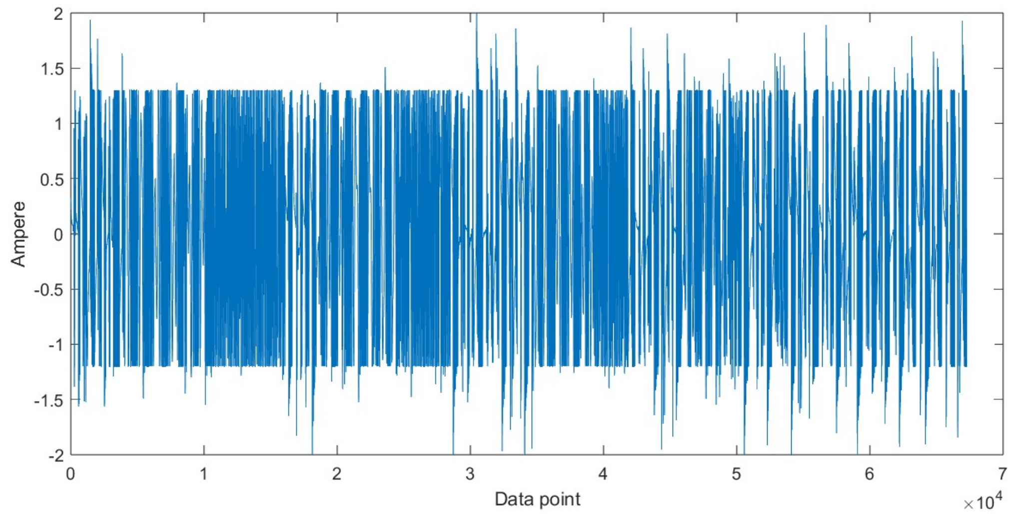

(b) Rock2pus Simulated

Figure 5.18: Rock2pus X Axis Signal Layers 39-49 Actual (a) vs Simulated (b)

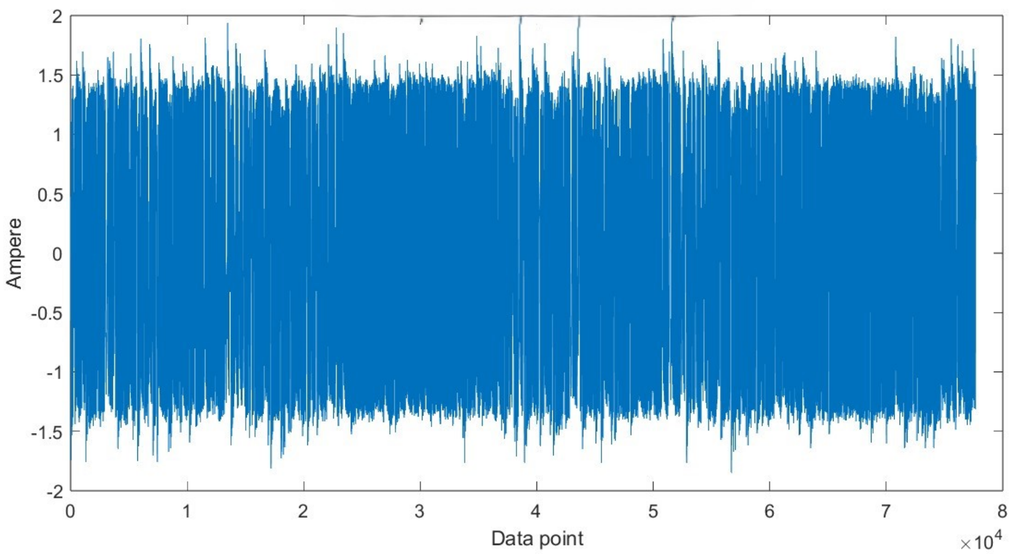

(a) Rock2pus Actual

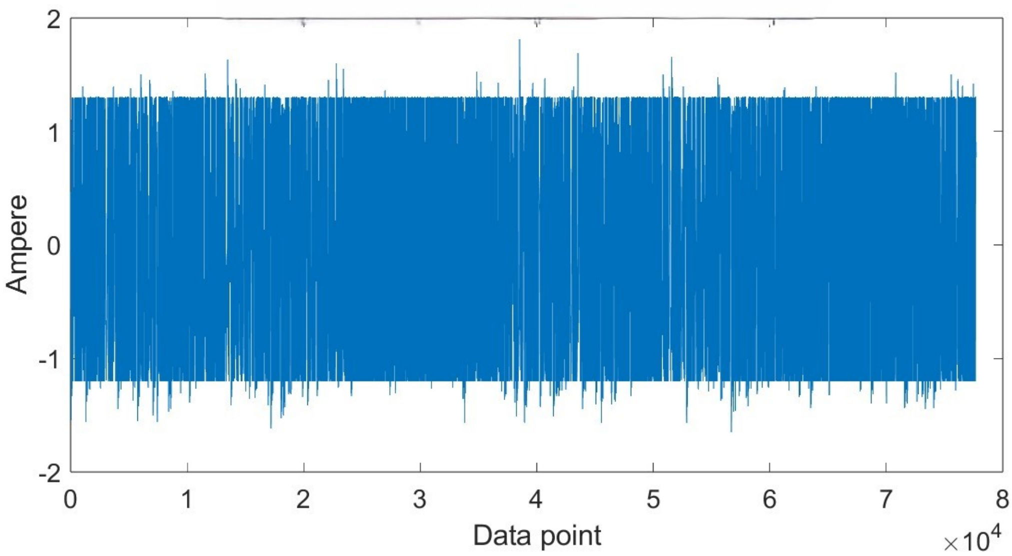

(b) Rock2pus Simulated

Figure 5.19: Rock2pus Y Axis Signal Layers 1-2 Actual (a) vs Simulated (b)

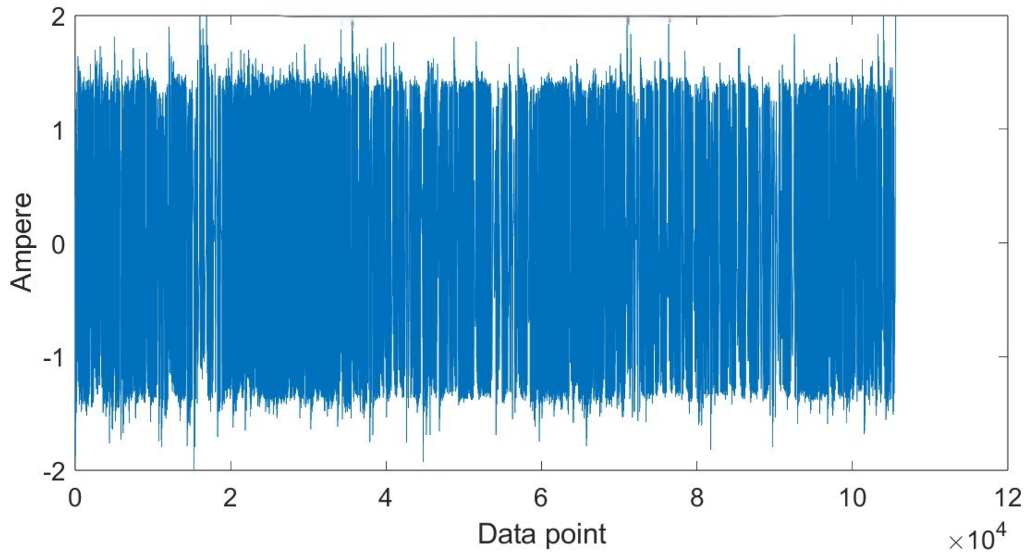

(a) Rock2pus Actual

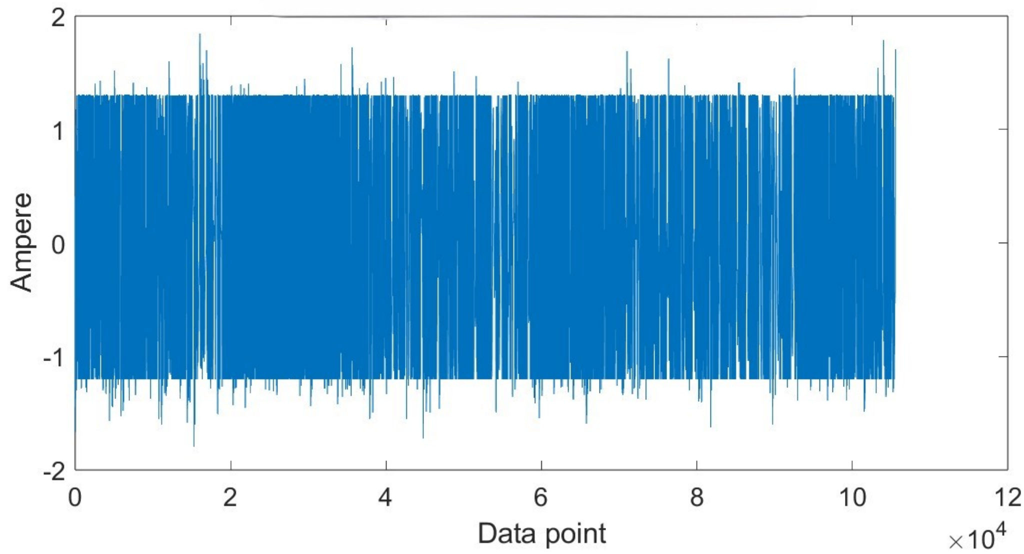

(b) Rock2pus Simulated

Figure 5.20: Rock2pus Y Axis Signal Layers 3-5 Actual (a) vs Simulated (b)

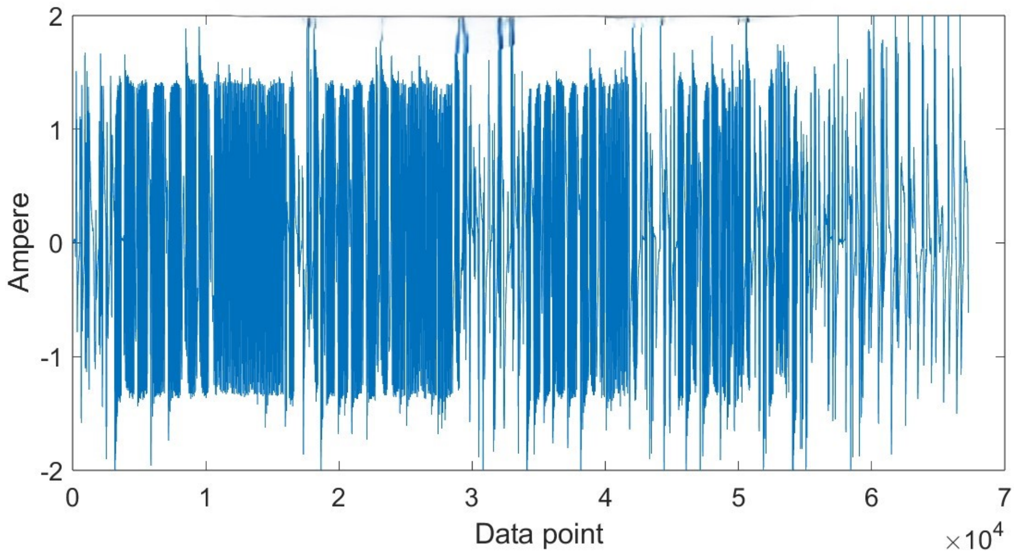

(a) Rock2pus Actual

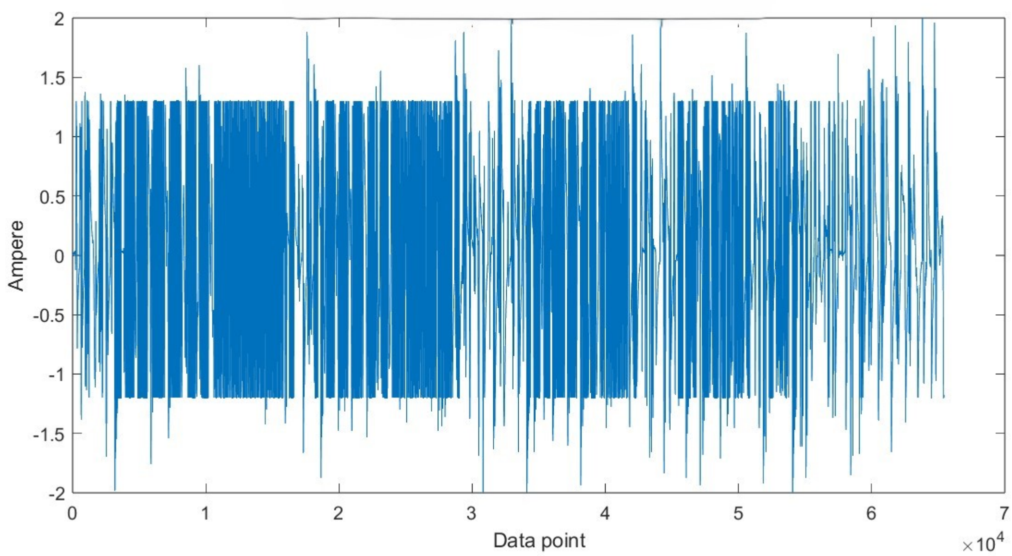

(b) Rock2pus Simulated

Figure 5.21: Rock2pus Y Axis Signal Layers 39-49 Actual (a) vs Simulated (b)

Figure 5.22 shows a comparison between the original and zoomed-in signals. The data is picked from the 48th layer of the Rock2pus. This section was chosen as it shows some problems capturing every detail of the process. The sections marked in the circle are somewhat successful in capturing the key steps. However, The zone marked in the rectangle had a change in direction in the original signal, which is absent in the simulated signal. Besides, the other marked areas have a little less prominence than the others. This can be traced back to a phase offset due to natural process variation.

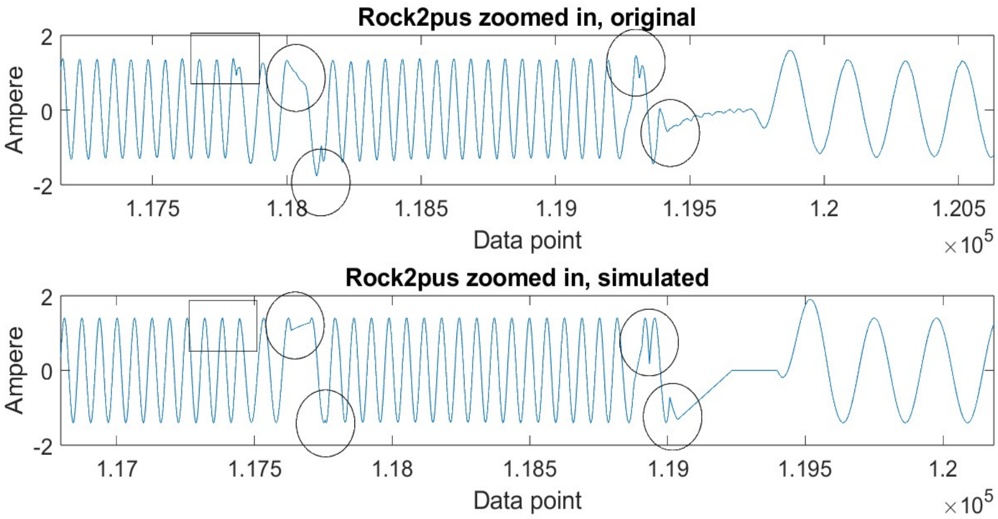

Figure 5.22: Simulated Vs Original Signal Zoomed, Rock2pus Along X Axis

5.5 Discussion

Each object of our study is printed ten times for this study. Once the individual signal was simulated, the object was printed using the Lulzbot Taz 6, and current data from all four axes were captured. The captured data is formatted and denoised, and data of interest is separated. The simulated data is then taken for comparison with the original signal.

Visual observation shows similar pattern between the actual and simulated signals. However, the actual signal appears to have a slightly different peak current. This can be explained by the ”DC offset” of the signal. The DC offset refers to a constant value that is added to the AC signal, causing the entire waveform to shift vertically.

The simulated signal works exceptionally well to predict the time needed to print the object and is really close to counting the number of peaks in the signal. Table 5.4 and 5.5 summarizes the time and peak counts for types of signals.

Object	Minimum	Mean	Maximum	Simulated
Rectangle	423.81	425.93	428.7	427.05
Cone	910.30	912.86	915.41	915.22
Rock2pus	1082.55	1085.8	1088.5	1088

Table 5.4: Time Comparison Between Signals (s)

Object	Minimum	Mean	Maximum	Simulated
Rectangle	6292	6297	6301	6241
Cone	13162	13168	13172	13027
Rock2pus	15649	15660	15669	15450

Table 5.5: Peak Count Comparison Between Signals

The simulated time falls within the typical range of time it takes to print a particular object. But they are close to the upper limit of the time. This can be attributed to the fact that a few times, a tool movement was observed to be slightly faster than the mentioned feed rate. The number of peak counts, however, has a different story. The peak counts in the original signal are counted using MATLAB, which was designed to filter unwanted peak detection due to noise. The "findpeaks" function of MATLAB was modified to avoid detecting points as peaks due to the presence of noise. The threshold for detecting peaks was set to 5% of the last peak. The minimum distance between peaks is set to be 10ms. This small gap is provided to accommodate sudden layer change as peaks but reduces false positive peak detection due to noise. The peak count using MATLAB was found to be less than that found using the Picoscope in-build measurement tool. The deviation in peak count in the worst scenario is less than 1.5%. One reason behind the higher number of peaks detected in the original signal is the presence of noise. Figure 5.23 shows an incident where an additional peak is observed due to noise. The area is marked in a circle. The simulated data, on the other hand, does not have the noise component. As a result, in this system, the number of peaks in the original signal is supposed to be more than that of the simulated signal.

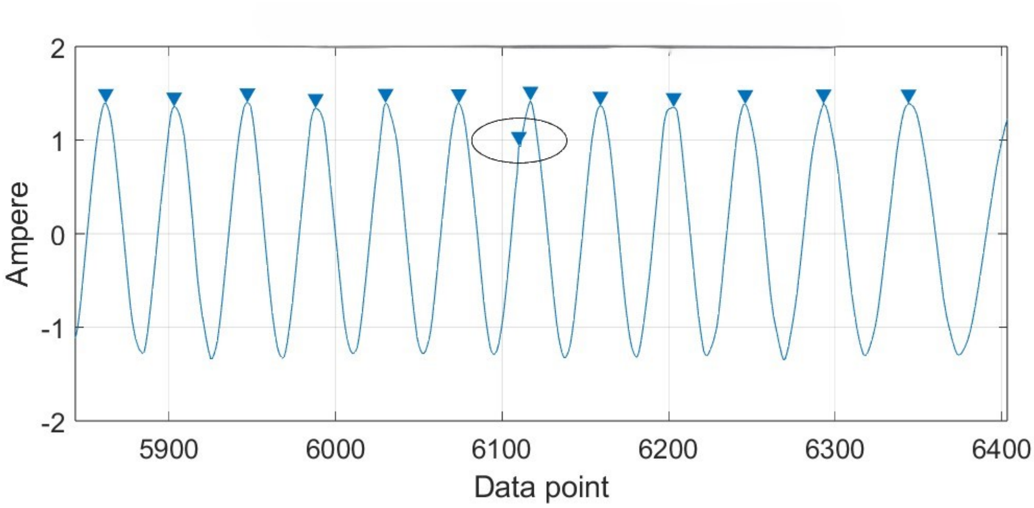

Figure 5.23: Additional Peak Detected Due to Noise

5.5.1 Similarity with Actual Signal

While predicting the actual run-time accurately suggests a good performance of the model, it is always possible to come up with a design that will take a similar time to print the object, but the properties will be different. In this case, we have replicated one attack detection method by [89]. Our approach, in this case, uses their research to see if there is any significant variation between the simulated and original signals to label them as totally different signals. The first step, in this case, involves downsampling the signal and dividing it into a window size of 32 and a window step of 16. Then, the Fast Fourier Transform is used for each frame, and the position of the maximum value in the FFT is found. This position is then used to compute the fingerprint value, which is added to the list of fingerprints. Finally, the list of fingerprints is returned. The outline is explained in Algorithm 4 [89].

The next step involves finding dissimilarity in layers.

Their research focused on detecting changes in the power side channel due to editing the code. In their research, the authors separated the data into windows and set up a threshold of more than 15 mismatches in a layer or 3 consecutive mismatches for a layer to be different from the actual print. these values were set by adding a 20% margin, rounded up, above the largest deviations observed between unmodified prints. For our research, the same approach is used to select a threshold. In their study, each layer had around 180 windows of 32 data points, on the

Algorithm 4 Fingerprint Creation

```
Require: signal, wnd_size, wnd_step
resample_rate ← 400
downsample ← Resample(signal, resample_rate)
fingerprint ← [ ]
frames ← SplitToFrames(downsample, wnd_size, wnd_step)
for each frame in frames do
    fft_frame ← FFT(frame)
    max_bin ← MaxPosition(ABS(fft_frame))
    fingerprint_value ← (max_bin / wnd_size) * resample_rate
    Append(fingerprint, fingerprint_value)
end forfingerprint
```

Algorithm 5 Is Similar

```
Require: layerA, layerB, offset, mismatch_threshold
mismatch ← 0
for i = 0 to len(layerA) − offset do
    if layerA[i + offset] ≠ layerB[i] then
        mismatch ← mismatch + 1
    end if
    if mismatch > mismatch_threshold then false
    end if
end fortrue
```

other hand, our object have variable number of windows in different layers. We kept the same ratio of mismatch as the threshold for our test object. In our research, the same principle is used to find the similarity between the actual and the simulated signals. The pseudocode to find dissimilarities is given in Pseudocode 5. Unlike their approach, our test objects have a variable number of data points in the signal. Thus, our threshold for the detection of dissimilar signals is variable.

In order for a signal to represent unusual activity, we require both X and Y channel data to be above the threshold. Figure 5.24 shows the number of mismatched windows in different layers for the rectangular object. It is seen that a few layers have a mismatch close to the threshold limit but did not cross it. This shows that the simulated data works similarly to any benign data.

The same approach is used to compare the simulated signals in the case of other objects. The threshold in those cases was adopted with a change in window number, and the objects seemed to mimic an actual benign print.

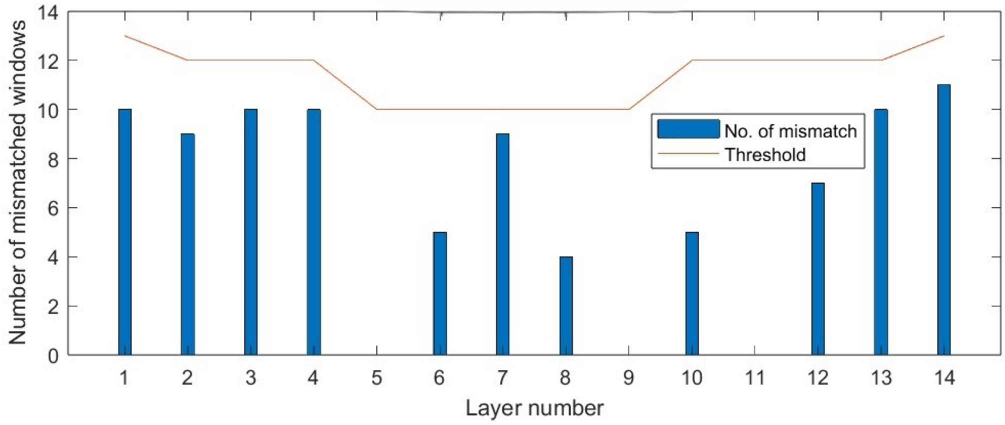

(a) Mismatch Along X Channel

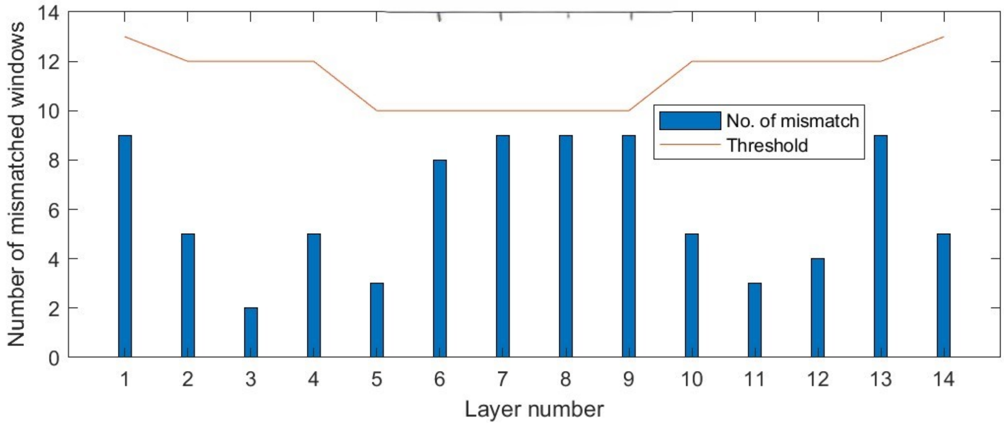

(b) Mismatch Along Y Channel

Figure 5.24: Mismatch Along Layers

5.6 Conclusion

This section talks in detail of simulating current signal based on G-code. In this section we talked about how we can extract information from G-code, how this information can be used to calculate some critical values and how these values can be summed up to generate a current signal. In the next phase we carried out some case studies to see the performance of our proposed method. The object chosen represent three different level of complexity. First, we analyzed the signal for a rectangle. This shape consists of straight lines. A rectangle represents the simplest object we can print. We compared the time and number of peask of the simulated data to the ten already printed samples. Once we got a healty accuracy, we went to explore how different machine movements are captured in the simulated signal. It appeared that the simulated signal was succesull in detecting key machine movements like change of speed, chang in direction, dwell etc. The similar steps are carried out for cone and Rock2pus. They represent much more complicated object as the features like circle and irregular curves appear in the design. In these cases also, our approach have similar results. For the Rock2pus, however, in some cases the key features were barely detected, and in one case, one feature was totally missed. Apart from these issues our proposed model was able to capture all key machine movement. Lastly we used a previous approach to see if that approach can distinguish between our simulated signal from the pool of known-good signal. It turned out that according to that algorithm, our simulated signal behaves similar to the actual data.

The findings of this study suggests that our proposed model can be utilized to obtain expected signal from the G-code.

Chapter 6

Study of Deviation in Current Signal in Fused Deposition Modeling Based on Print Complexity

Our two previous research helped us simulate a side-channel profile. Our aim is to use the simulated signal to detect process anomalies. This can be done by comparing a test signal obtained while printing to the simulated signal.

Stepper motors are used in the FDM printers to produce an identical current profile under the same conditions. But in reality, there lies some variation in the system. As in previous sections, it is observed that the variation increases with an increase in feed rate and a decrease in length. With increased complexity, the number of lines in a command also increases. Combining all these events increases the variation of the output current profile. Thus, it is necessary to know the nature and range of the variation caused by different properties of the printed object.

This nature of the process makes it difficult to compare between signals. One way this issue is often resolved is by collecting data from multiple instances of the operation and designating a range of deviations under which the system is marked as acceptable. The aforementioned approach, however, works for only that particular object, requiring one to repeat the process multiple times if a new object is to be studied. Our proposed approach aims to model process deviation in the current side-channel signature in a Fused Deposition Model (FDM) machine such that the expected range of process deviation can be calculated from the G-code of the print alone. The work analyzes the deviation in the current signature generated by the stepper motors used in an FDM process when objects of different levels of feature complexity are printed. First, the test print objects are categorized in terms of feature complexity and number of features. Both the feature complexity and number of features can be categorized as low, medium and high. Thus, any print can fall into one of the nine combinations possible. Each print object is repeated multiple times to analyze the deviations. The second step in this work involves selecting a parameter to measure the deviation between signals and comparing the signals of a particular layer of print between objects with identical G-code. In the third step, a comparison is made about how the deviation among signals changes with the change in feature complexity and numbers. Findings of this stage are used to model the expected signal deviation between two signals with the same G-code. Successful implementation of the proposed approach will remove the need to print an object multiple times to obtain a standard range of acceptable good signals.

6.1 Process Outline

This study is based on the understanding of the signal. So, the first step is a detailed study of the signal. In the next step, we selected the objects to be printed and studied. The Objects are categorized into different levels of complexity and feature numbers. The general idea is that the more complex objects will have higher deviation among themselves. Each selected design is printed ten times and compared with each other. The next step is a layer-by-layer comparison of the signal. A detailed study of this step shows the contributors of deviation between signals. It turned out the common contributors are noise, the asynchronous nature of prints, and residual currents. This information is used to find the expected range of signal deviation in the case of good prints. Finally, the objects with both good and bad designs are compared to see if the model is good enough to detect unexpected features in the print objects. Figure 6.1 outlines the detailed process.

6.2 Case Studies

In this study, nine objects were selected. The objects are characterized by feature complexity and the number of features. Each of the characters has three levels: low, medium, and high. Thus, any object printed can classified as one of nine types. The objects printed for this study are printed with the default setup, with an in-fill rate of 20%. The printer, however, can not print each layer with the same fill rate. At the beginning and end layers of an object, the prints have a 100% in-fill rate to provide support for the design and also to have the expected surface finish. Table 6.1 explains different levels of feature complexity and feature size.

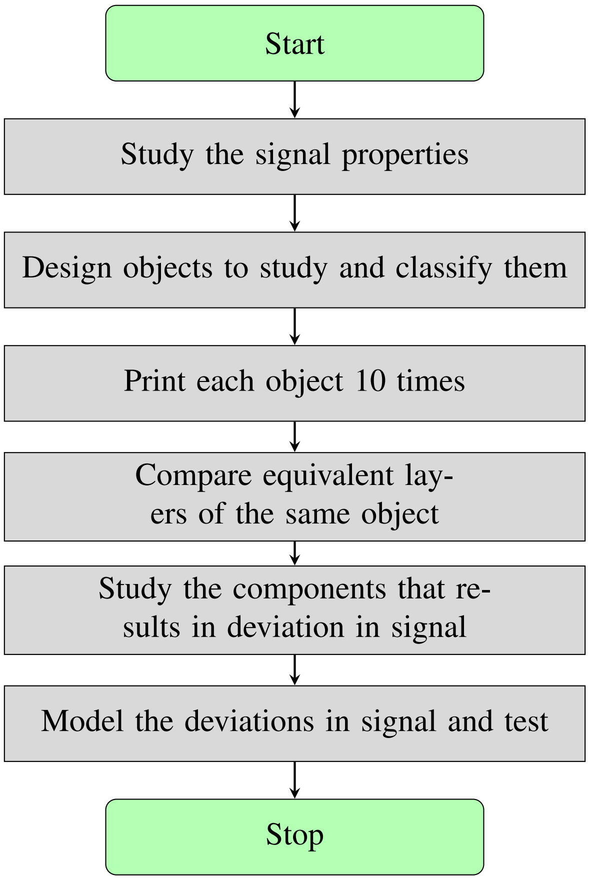

Figure 6.1: Process Flow

Characteristics	Level	Explanation
Feature complexity	Low Medium High	Mainly straight lines Straight lines and circles All inclusive
Feature number	Low Medium High	Mostly similar layers Layers vary significantly Almost every layer is unique

Table 6.1: Feature and Characteristics Explained

These features are solely based on the appearance of the object printed. It is to be noted that, in FDM print, it is difficult to have printed with exactly one type of geometrical movement. The examples of different print types are shown in Figure 6.2. Each object under study was printed 10 times.

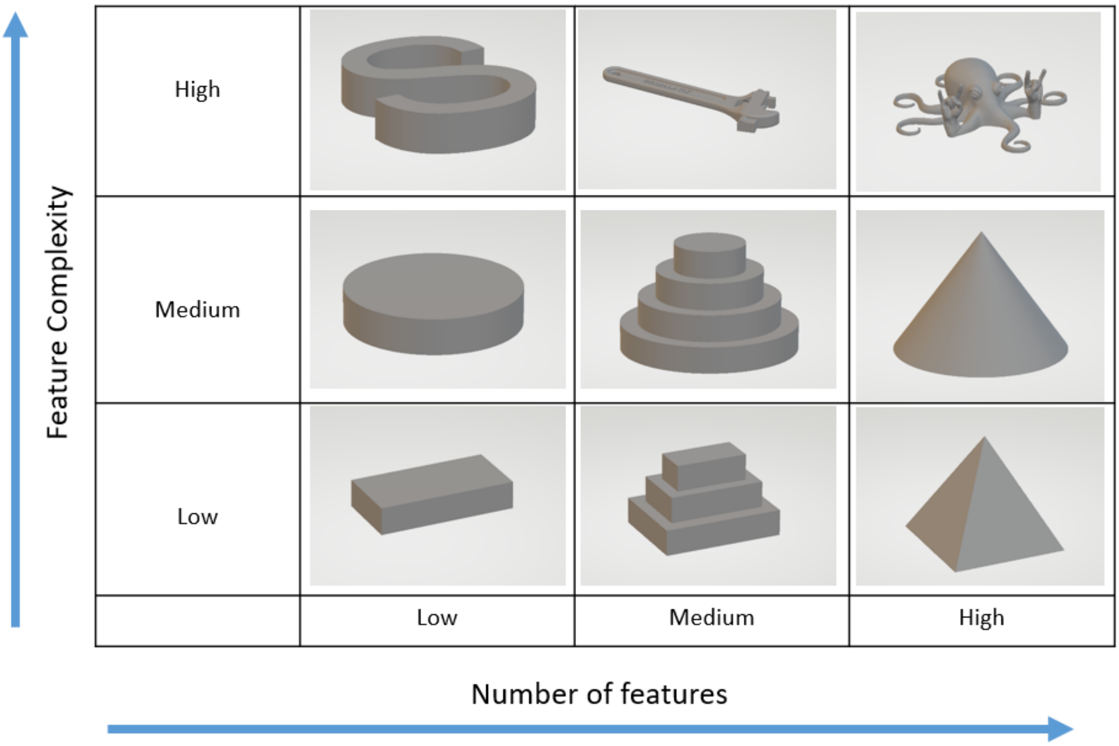

Figure 6.2: Objects Under Study

6.2.1 Data Analysis

Each object's data is first split into layers. The splitting is performed by observing a spike in the Z-axis data. During printing any layer, the Z-axis motor remains idle, resulting in a flat line in the current graph. However, a change in layer is signified by a change in peaks of the Z-axis curve. Usually, this change accompanies a flat line along the X and Y axes. During the operation, the Z-axis can occasionally exhibit unexpectedly high peaks for a short burst of time. Studies showed that such peaks are observed when the extruder head needs to move to a different position at the same height level without continuing material extrusion. Thus, a change of layer is defined when a high peak is observed along the Z-axis data for a longer duration. The exact duration and number of peaks depend on the print settings. In this study, the minimum possible print height (10 mm) denoted in the product specification is considered the minimum movement required along the Z-axis to denote a layer change. Figure 6.3 demonstrates layer segregation. In the graph, positive peaks are marked by green dots and negative peaks by red. In one case, it is observed that there is a red dot with a relatively higher current value than the idle state. This peak is considered a one-off situation here because there are not enough high peaks in close vicinity.

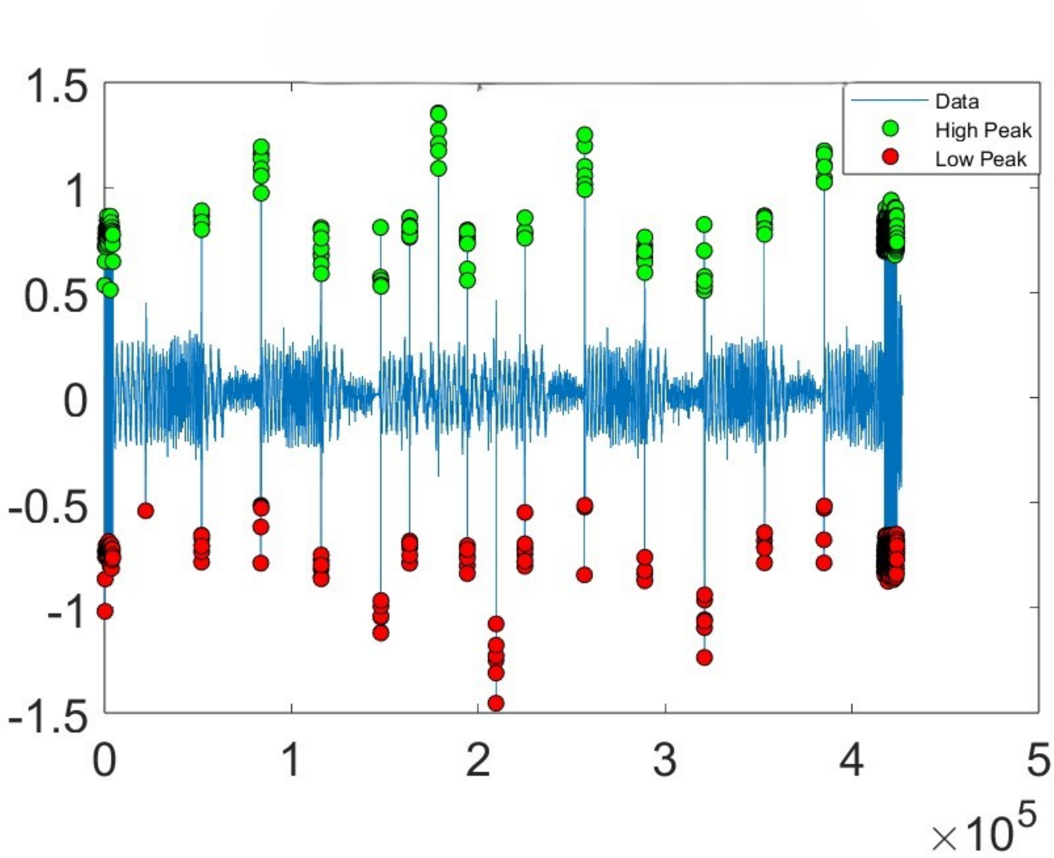

Figure 6.3: Segregating Layers by Z axis Data

Once the data is segregated into layers, different prints of the object with the same G-code are compared on each layer. The distance between signals in each layer is measured by using the Dynamic Time Warping (DTW) algorithm. After layer-by-layer comparisons between similar objects, the maximum distances are recorded.

6.2.2 Dynamic Time Warping

Dynamic Time Warping (DTW) is an algorithm used for measuring the similarity between two temporal sequences that may vary in speed or timing [92]. It is particularly useful in applications such as speech recognition. The advantage of using the DTW algorithm lies in the fact that it works great for comparing data with different lengths. In DTW, the warping path is a series of index pairs that define the mapping between elements of the two sequences. This path is constructed in such a way that the overall distance between the sequences is minimized. A cost matrix $c(i, j)$ is created such that it represents the cost of aligning the i-th element of the first sequence with the j-th element of the second sequence. The cumulative cost matrix D is used to find the optimal warping path. Each element $D(i, j)$ represents the minimum cumulative cost to align the sequences up to i and j. The matrix is filled using the following recurrence relation:

$$D(i, j) = c(i, j) + min\{D(i-1, j), D(i, j-1), D(i-1, j-1)\} \tag{6.1}$$

The optimal warping path is determined by backtracking from $D(n, m)$ to $D(0, 0)$, which results in the minimal cumulative cost. Algorithm 6 shows a pseudocode of DTW.

Algorithm 6 Dynamic Time Warping

Require: Sequences $X = [x_1, x_2, \ldots, x_n]$ and $Y = [y_1, y_2, \ldots, y_m]$
Ensure: DTW distance $DTW(X, Y)$

1: $n \leftarrow$ length of X
2: $m \leftarrow$ length of Y
3: $DTW \leftarrow$ 2D array of size $(n+1) \times (m+1)$ initialized with ∞
4: $DTW[0][0] \leftarrow 0$
5: **for** $i \leftarrow 1$ to n **do**
6:     $DTW[i][0] \leftarrow \infty$
7: **end for**
8: **for** $j \leftarrow 1$ to m **do**
9:     $DTW[0][j] \leftarrow \infty$
10: **end for**
11: **for** $i \leftarrow 1$ to n **do**
12:     **for** $j \leftarrow 1$ to m **do**
13:         $cost \leftarrow d(x_i, y_j)$
14:         $DTW[i][j] \leftarrow cost + \min(DTW[i-1][j], DTW[i][j-1], DTW[i-1][j-1])$
15:     **end for**
16: **end for**
        $DTW[n][m]$

Here, the initiation phase introduces sequences X and Y. Lines 1 and 2 determine their lengths. Lines 3-4 tell us to create a 2D array of (n+1)*(m+1) size. Every element is set to infinity except for the first one, which is set to 0. For each pair of indices (i,j), calculate the cost of aligning the elements x_i and y_j using a distance function $d(x_i, y_j)$. This function is typically the Euclidean distance. The DTW table DTW[i][j] is then updated with the computed cost plus the minimum of the three neighborhood cells. The final DTW distance is found by DTW[n][m]

DTW was chosen due to its ability to work with data of unequal sample size. The FDM process is asynchronous by nature. Thus, it is likely to have different sizes of data for different iterations of data. DTW is thus a very good candidate for such type of data analysis. One drawback of DTW is, however, that the matrix size becomes exponentially larger with added data. Thus, to cope up, the data is split into smaller windows. The maximum size of the window is kept as a maximum number of data points of a layer in the object categorized as (low, low) complexity.

6.2.3 Results

This section discusses the deviation results under different scenarios. Each layer of an object type is compared with the same layer of the same object type. The study was conducted to produce results for all possible combinations of each object type. Total possible combination of such comparison is

$$102 = \frac{10 \times 9 \times 8!}{2 \times 1 \times 8!} = \frac{10 \times 9}{2 \times 1} = \frac{90}{2} = 45$$

. Since it is difficult to display 45 comparisons in a table, 5 paired comparisons are shown in the following sections.

6.2.3.1 Low, Low

The representative of this group is a rectangle. Here, the feature is straight lines, and each layer appears to be the same. The print was made with a system default 20% in fill rate. The machine, however, applies the in fill rate only after a certain condition is matched. By default, the first and last 4 layers are fixed with a 100% in fill rate. Figure 6.4 shows a graph of the DTW distance per data point for object (low,low).

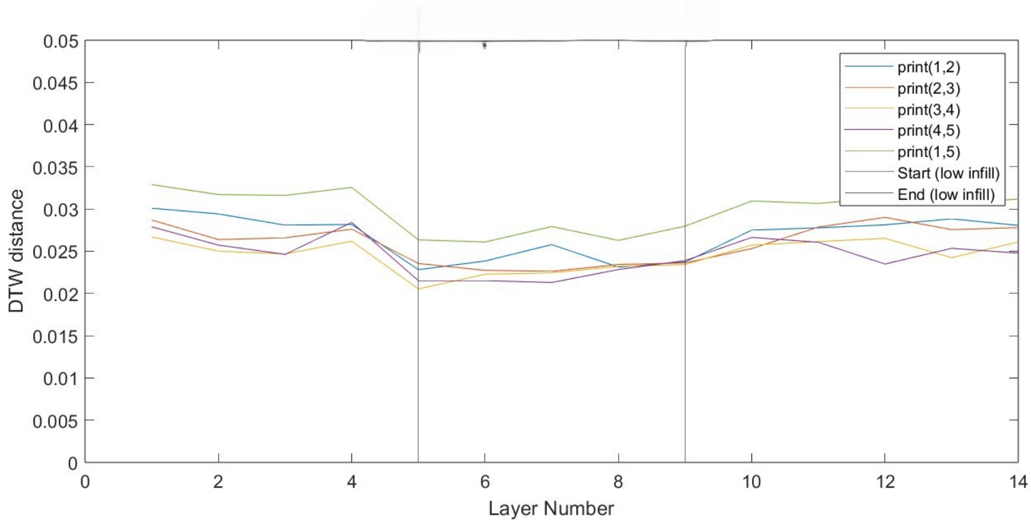

Figure 6.4: DTW Comparison for Object Low Low

In this particular object, layers five to nine have a 20% in-fill rate and thus have a lower number of data points to consider. A lower time required for a print can mean a lower error accumulation in the process. This explains the lower deviation in these layers.

6.2.3.2 Low, Medium

The representative of this group is a stepped rectangle. This object consists of 52 layers in total. Like in the case of our first test object, apart from 1st four and last four, each layer have a 20% in fill rate. The object have three distinct rectangular steps. Figure 6.5 shows the selected comparison for a low, medium setup. The figure shows some kind of staircase feature that mimics the layer positions.

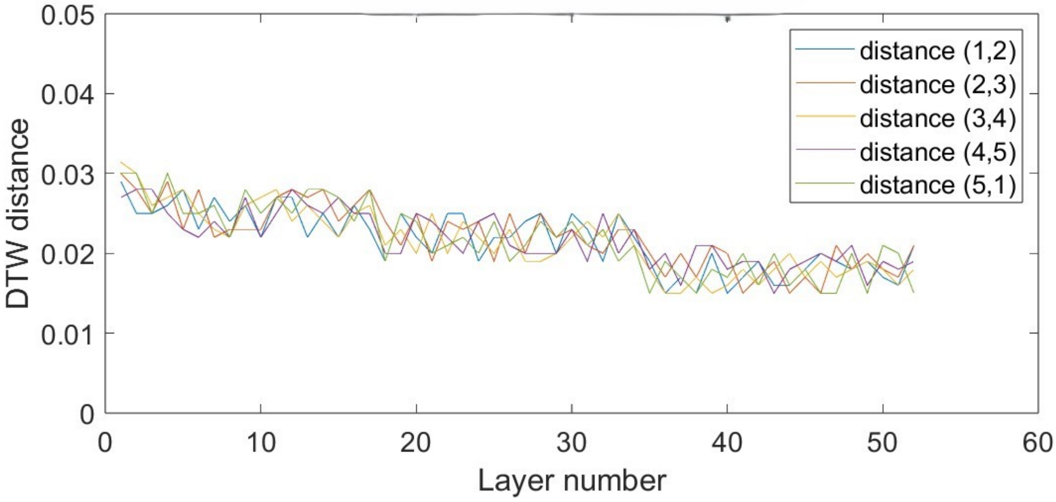

Figure 6.5: DTW Comparison for Low Medium

6.2.3.3 Low, High

The representative of this group is a pyramid. This object consists of 76 layers in total. In this case, each object is different from the last layer. Figure 6.6 shows selected comparison for low medium setup. This graph shows correlation between number of data points and the DTW distance. However, there are some places that shows somewhat elevated dissimilarities.

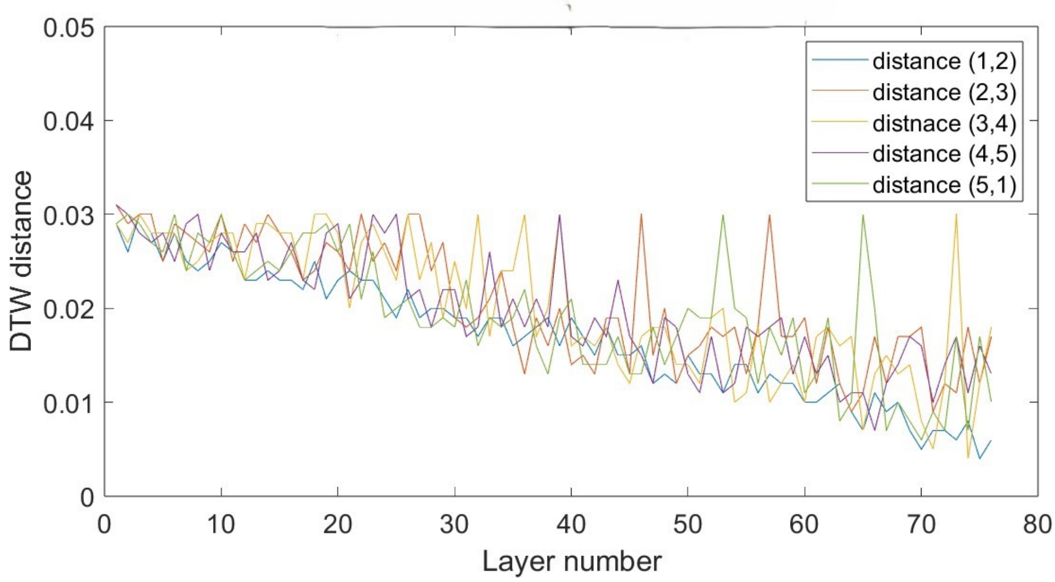

Figure 6.6: DTW Comparison for Low High

6.2.3.4 Medium, Low

The representative of this group is extruded circle. The major feature in this case is circular and it appears to have identical layers throughout. This object consist of 20 layers. Figure 6.7 shows selected comparison for medium low setup. This figure shows similar behavior like that in Figure 6.4. The distances at the beginning and end tends to be slightly higher than the middle section. Like the (low,low) object, the infill rate is 20% in the middle section.

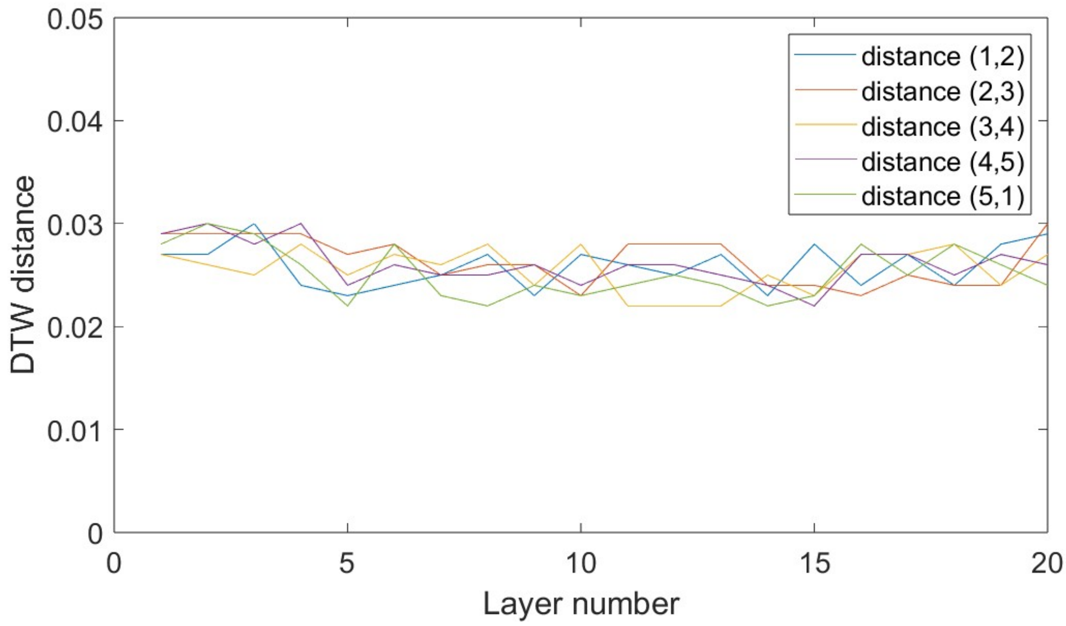

Figure 6.7: DTW Comparison for Medium Low

6.2.3.5 Medium, Medium

The representative of this group is stepped circle. The major feature in this case is circular and it have 4 distinct stpes. This object consist of 64 layers.

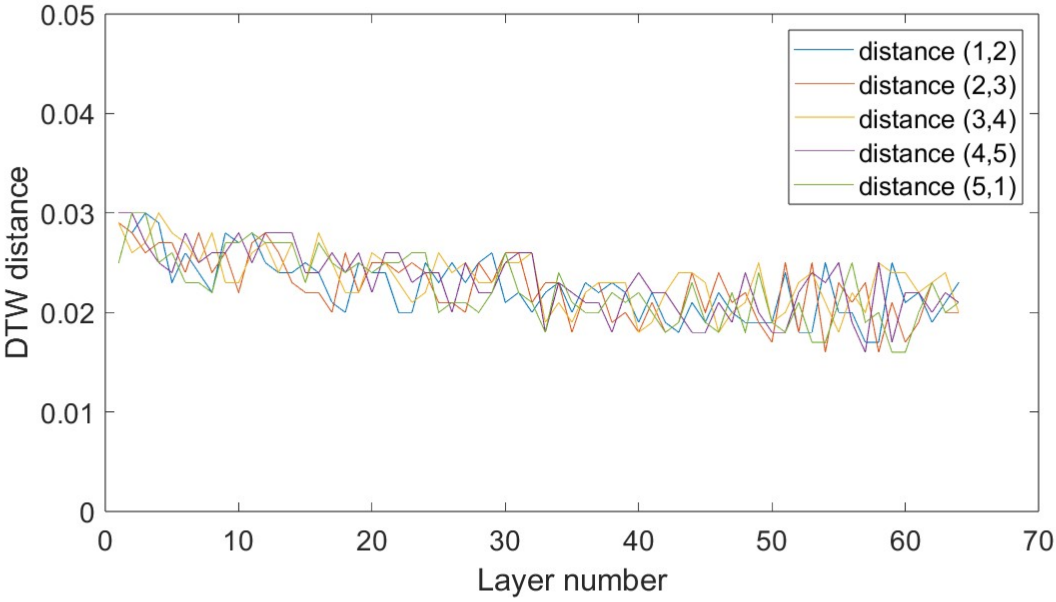

Figure 6.8: DTW Comparison for Medium Medium

Figure 6.8 shows selected comparison for medium medium setup. The DTW distance tends to lower as we proceed to objects with lower number of data points. This graph behaves similar to the 6.5 figure.

6.2.3.6 Medium, High

The representative of this group is a solid cone. The major feature in this case is circular and each layer is different in this setup. This object consists of 86 layers.

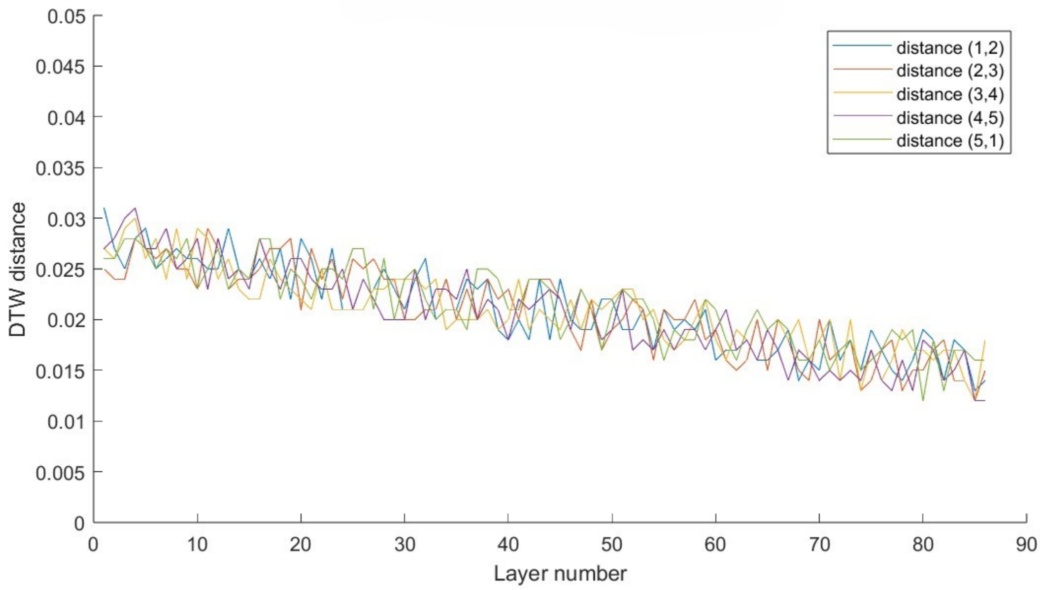

Figure 6.9: DTW Comparison for Medium High

Figure 6.9 shows selected comparison for medium high setup. This figure show similar properties like the Figure 6.5. Diminishing number of data points shows a diminishing distance.

6.2.3.7 High, Low

The representative of this group is the letter S extruded. The major feature in this case is irregular curves, and each layer looks identical to the other in this setup. This object consists of 26 layers.

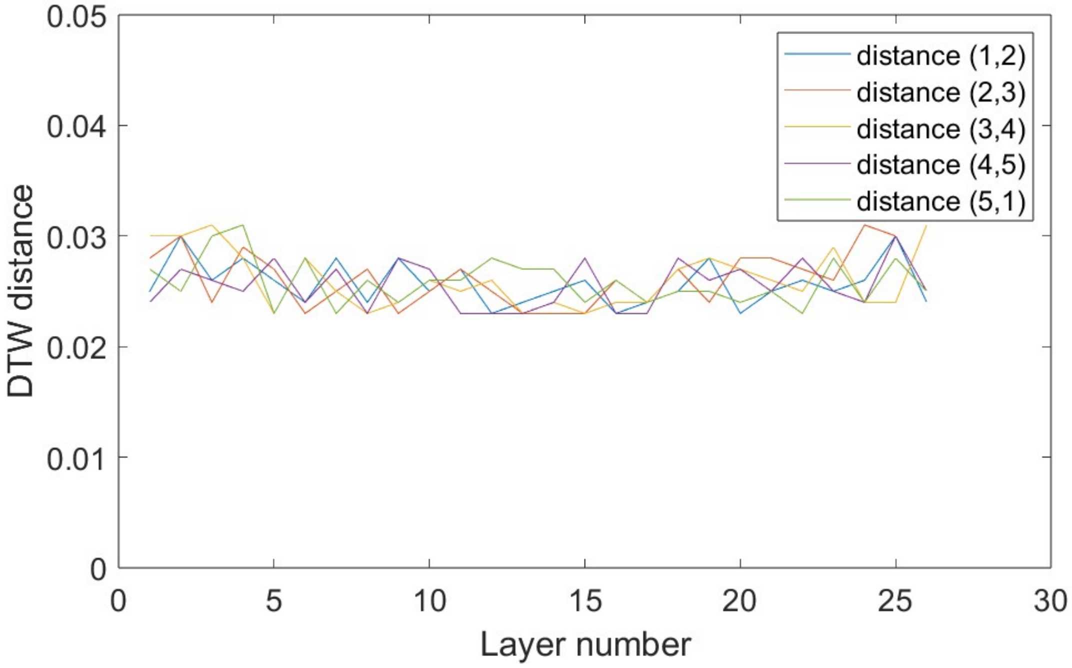

Figure 6.10: DTW Comparison for High Low

Figure 6.11 shows the selected comparison for high-low setup. The property mimics the other objects in the category of low in terms of number of features.

6.2.3.8 High, Medium

The representative of this group is an adjustable wrench. The object includes features like straight lines, curves, and circles.

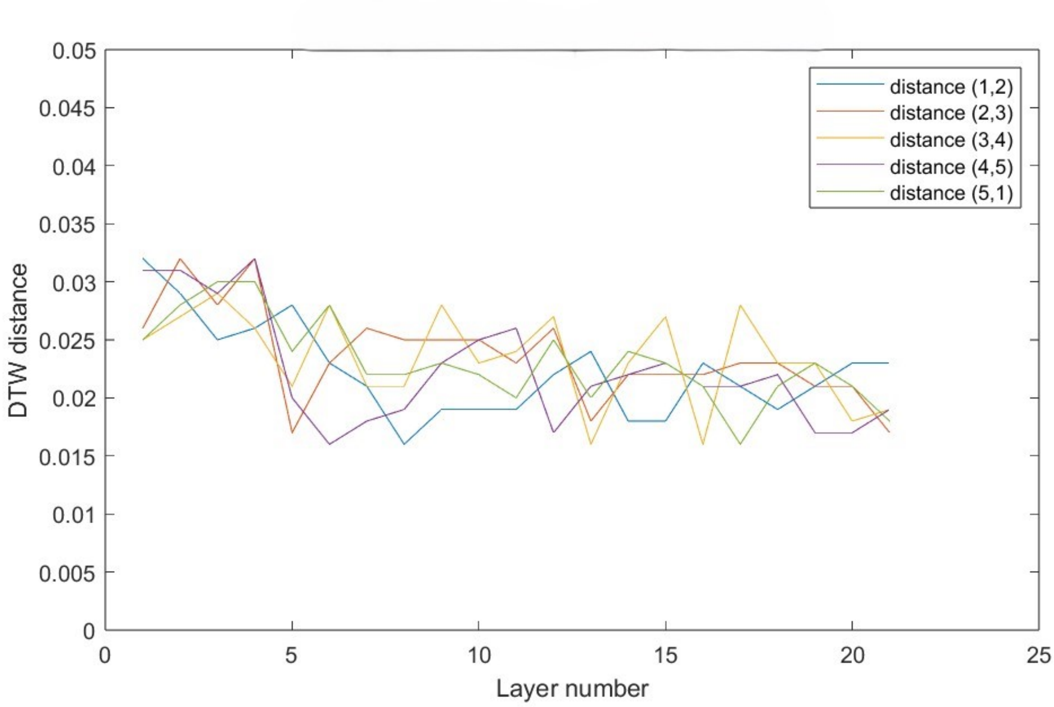

Figure 6.11: DTW Comparison for High Medium

Figure 6.9 shows the selected comparison for the high-medium setup. The wrench consists of 21 layers. This object has a few layers that are repeated. Unlike other previous objects in this study, the number of data points did not decrease as we up. In stead, there are some layers in middle that have higher number of data points than both the upper and lower part of the object.

6.2.3.9 High, High

The representative of this group is the Rock2pus. The object includes features like curves, and circles. In this case each layer is different prom the others. For This object consists of 51 layers.

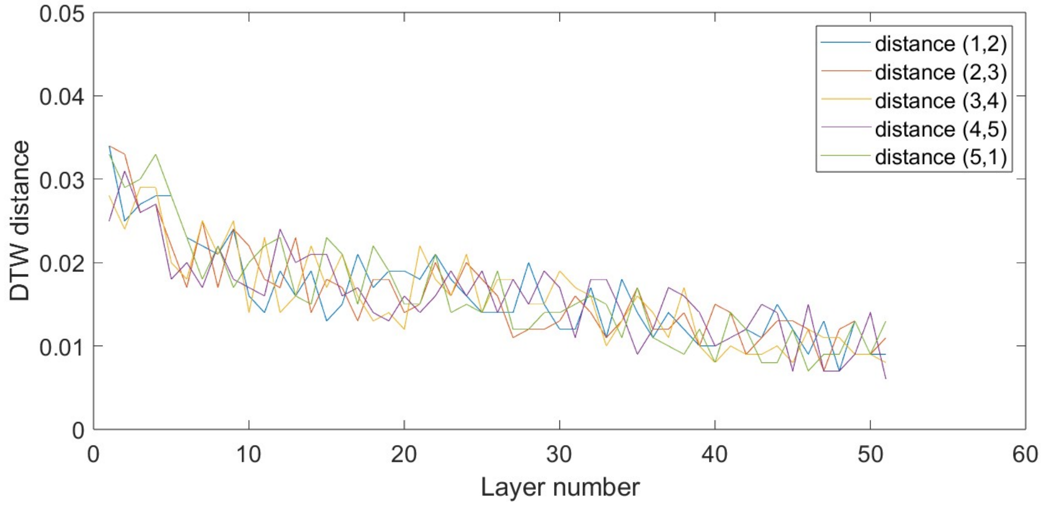

Figure 6.12: DTW Comparison for High High

Figure 6.12 shows the selected comparison for the high-medium setup. In this case, the number of data points gets reduced as we go up. This section also shows similarity with Figure 6.6 and 6.9.

6.2.4 Observation

The first observation in this study is the asynchronous nature of data. Figure 6.13 and 6.14 demonstrate how two aligned data streams differ significantly after some time. The deviation, however, is not homogeneous throughout the process. It is not uncommon to observe the signal once, leading to a lag compared to the other signal.

Figure 6.15 shows one of the areas that results in the highest deviation. This portion of data can be divided into three sections: first, the motor is running, then it stops, and it starts again. Throughout this study, it has been observed that a higher deviation is always visible when a motor remains at rest. One more reason behind deviation can be traced back to noise in the signal. Even though the signals are mostly denoised, some noise still persists which can contribute to the deviation among the signals. All the figures highlighted in this section show noise of some magnitude.

Irrespective of the external complexity, the features causing most of the deviation persist in all types of objects. This becomes apparent when trying to find the maximum DTW distance for objects with different complexity. The general expectation was to observe higher deviation

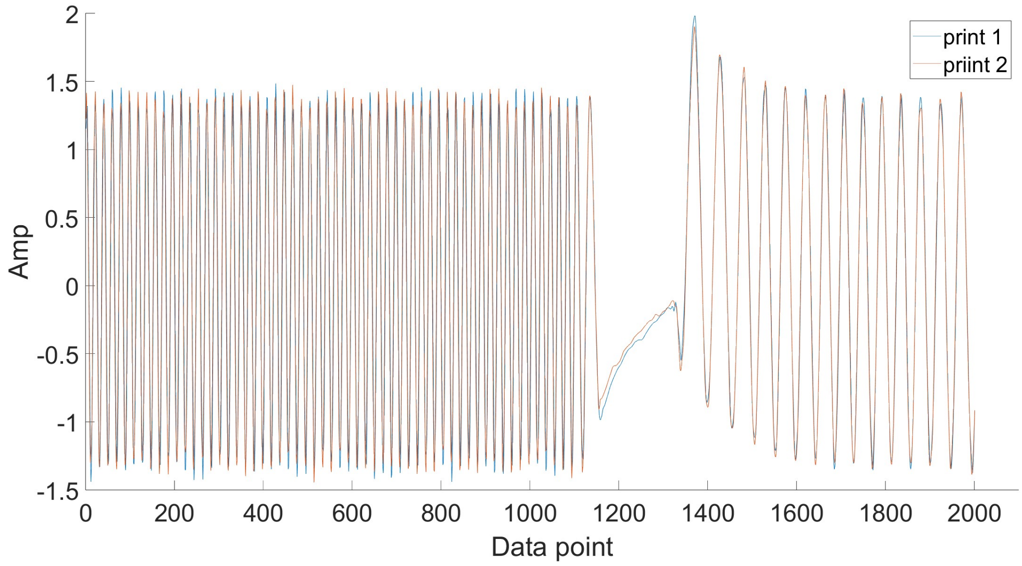

Figure 6.13: Signals at the Beginning

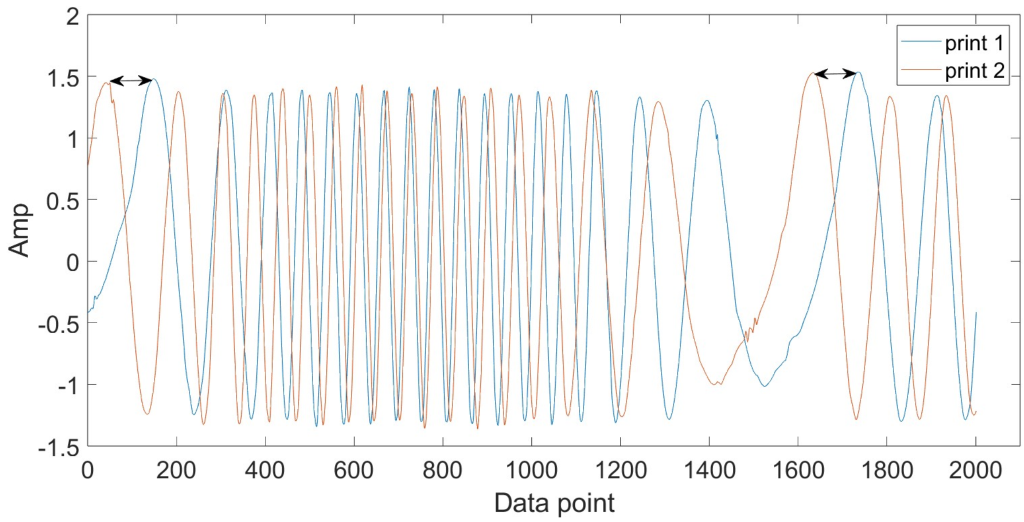

Figure 6.14: Signals at the Later Phase

as we go to more complex features. The result, however, shows little correlation with feature complexity. Since the aim of this study is to model a threshold of maximum deviation, we primarily focus on the highest DTW distance. Table 6.16 shows the distribution of different levels of complexity. In this table, the Complexity of an object is expressed in terms of (feature complexity and feature numbers).

It is observed from the table that objects with a high number of features have a very low distance in some layers. This can be explained by the fact that these objects have a very low number of data points in the top layer, resulting in less error accumulation. This study, however,

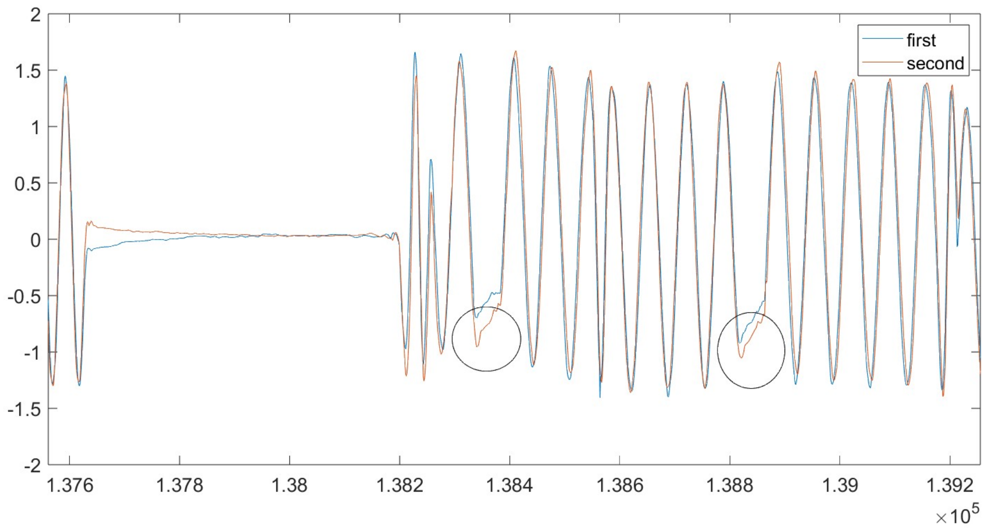

Figure 6.15: Higher Deviation in Signals at Idle Phase

Feature Complexity ↑

High	Max = 0.031 Min = 0.023 Mean =0.027 SD= 0.003	Max = 0.031 Min = 0.016 Mean =0.028 SD = 0.004	Max = 0.033 Min = 0.009 Mean =0.024 SD = 0.008
Medium	Max = 0.031 Min = 0.022 Mean =0.027 SD = 0.003	Max = 0.031 Min = 0.016 Mean =0.027 SD = 0.005	Max = 0.031 Min = 0.007 Mean =0.022 SD = 0.008
Low	Max = 0.031 Min = 0.022 Mean =0.025 SD = 0.002	Max = 0.031 Min = 0.015 Mean =0.025 SD = 0.005	Max = 0.031 Min = 0.007 Mean =0.020 SD = 0.008
	Low	Medium	High

Number of features →

Figure 6.16: DTW Deviation at Different Levels

shows some areas that dictate the deviation in the signals. These are primarily a number of data points that refer to the actual run time and the idle time of the motors. This information can be used to model the deviation in new test prints.

Chapter 7

Conclusion

This chapter highlights the three key contributions of the doctoral research study. The following subsections outlined the contributions, limitations, and plans for future works of the three studies.

7.1 Contributions

This research consists of three contributions, all of which aim towards anomaly detection by using side-channel information. This research, however, aims to achieve the target by using a simulated signal instead of a range of reference signals. The first contribution works towards understanding a typical FDM machine and how it produces one of the side-channel information, current pulled by the motors.

In the first study, components responsible for side-channel information are studied in detail, and a relation between the signal and the G-code command is established. Understanding the correlation between the command and signal properties plays a vital role in simulating the current profiles. One of the key findings of this study is that this particular model of 3D printer treats curves as the summation of small straight lines. As a result of this property, all types of movement can be characterized in the same way. The initial research plan was about preparing a data repository of signals resulting from different designs and using machine-learning approaches to predict data for unseen designs. Once the working mechanism of the printer is studied, a mathematical model seems appropriate for this research.

For the second research contribution, the printing process was studied at a deep level. The software and machine commands used to print the objects differ from machine to machine. Though there are several open-source applications available to carry out the same task, we preferred to stick to the application packages suggested by the vendor of the 3D printer. One observation in this study was the absence of some commonly used G-code commands like G2 and G3 designated for movements in a curved path. The absence of some particular commands made us rethink which of the G-code commands should be studied. In order to see the types of commands used, we explored and printed different open-source 3D models like Benchy, Rock2pus, and Stanford Bunny. It was observed that the slicer uses only a handful of different types of commands to carry out the task, irrespective of the complexity of the object. While it is possible to have a G-code file generated through a different slicer and use that to print in our 3D printer, we mainly used the commands that were used by our slicer. This study is the first to simulate a side channel based on the given G-code. This paves the way for the inclusion of more side channels in future studies.

Our first and second contributions are based on the fact that a typical FDM printer uses stepper motors instead of a closed-loop control system, and they offer a good deal of repeatability in the process. While comparing the simulated data with actual data, the asynchronous nature of the data was observed. For data exploration, we have super-imposed data, only to realize that after some time, there is a deviation in the phase of the signals. The deviations also appeared random. It was not uncommon for one signal to lead another for a few seconds and then to trail behind at a later time. Apart from this phenomenon, noise and natural process variation are always present in such data.

The third contribution of the research aims to study the deviation in the signals based on feature complexity. In this case, objects with variable complexity are printed a few times to explore if any correlation exists between feature complexity and signal variation. Initial observations showed that deviation among simplest objects are really close to the deviation among objects with much higher complexity. The result seemed counterintuitive. A deeper investigation, however, showed that there are some features like start after stop, asynchronous nature of the signals, noise all have some impact on the deviations of the signal, and these values are present in all type of prints irrespective of their complexity. These are mainly observed when one of the motors remains stopped. This property is prevalent in all types of prints. These findings are used to model the expected deviation to a test object.

7.2 Limitations

In our research, we focused on using the vendor-suggested approaches to mimic a standard operation. As a result, our model is built on a lower number of G-code commands. It is possible to print quality products with G-code that was originally designed for another model. Our research excluded those G-code commands.

In the third contribution, the objects were labeled based on their visual complexity. However, in terms of the actual G-code command, there seemed to be a lower variation among the prints. The model selection could have been done based on the G-code. This approach might have produced a different type of result

7.3 Future Work

The next step of our research is to use the findings of the three contributions to prepare a model to detect process anomalies. First, a simulation of the current profile will be generated, followed by signal deviation estimation. This reference signal and deviation are then to be compared to the test signal to detect system anomalies.

This research opens up a lot of possibilities for future work. In our case, we simulated the current signal for a particular model of a 3D FDM printer. An initiative can be taken to do the same with FDM machines in general. Setting up such a framework can make it easier to expand to other types of research.

The success of our research demonstrates that it is possible to model side-channel information. From a security perspective, different side channels, like sound, vibration, and heat, among others, can be studied. A successful simulation of these can result in a much faster anomaly detection requiring much less data storage.

References

[1] D. S. Landes. *The wealth and poverty of nations: why some are so rich and some so poor*. W.W. Norton, New York, 1st ed edition, 1998.

[2] Industrial revolution - from industry 1.0 to industry 4.0. `https://tinyurl.com/2p8dw3zh`. Accessed on October 17, 2022.

[3] M. Mamad. Challenges and benefits of industry 4.0: an overview. *International Journal of Supply and Operations Management*, 5:256–265, 2018.

[4] E. Karayel and Y. Bozkurt. Additive manufacturing method and different welding applications. *Journal of Materials Research and Technology*, 9(5):11424–11438, 2020.

[5] R. Langner. Stuxnet: dissecting a cyberwarfare weapon. *IEEE security privacy*, 9(3):49–51, 2011.

[6] World economic forum. `https://www.weforum.org/agenda/2015/01/companies-fighting-cyber-crime/`. Accessed: 2023-01-30.

[7] A. A. Cardenas, S. Amin, B. Sinopoli, A. Giani, A. Perrig, and S. Sastry. Challenges for securing cyber physical systems. 5(1):7, 2009.

[8] L. Li, W. He, L. Xu, I. Ash, M. Anwar, and X. Yuan. Investigating the impact of cybersecurity policy awareness on employees' cybersecurity behavior. *International Journal of Information Management*, 45:13–24, 2019.

[9] G. Loukas. *Cyber-physical attacks: A growing invisible threat*. Butterworth-Heinemann, 2015.

[10] D. Kushner. The real story of stuxnet. *IEEE Spectrum*, 50(3):48–53, 2013.

[11] T. Alladi, V. Chamola, and S. Zeadally. Industrial control systems: Cyberattack trends and countermeasures. *Computer Communications*, 155:1–8, 2020.

[12] N. Jazdi. Cyber physical systems in the context of industry 4.0. In *2014 IEEE International Conference on Automation, Quality and Testing, Robotics*, pages 1–4, 2014.

[13] L. Wang, M. Törngren, and M. Onori. Current status and advancement of cyber-physical systems in manufacturing. *Journal of Manufacturing Systems*, 37:517–527, 2015.

[14] L. Wang and C. A. Alexander. Big data analytics and cybersecurity for advanced manufacturing. *Industrial and Systems Engineering*, 1(1):10, 2016.

[15] K. Hemsley and R. Fisher. A history of cyber incidents and threats involving industrial control systems. In *Critical infrastructure protection xii*, IFIP Advances in information and communication technology, pages 215–242, Cham, 2018. Springer international publishing.

[16] S. R. Chhetri, J. Wan, and M. A. A. Faruque. Cross-domain security of cyber-physical systems. In *2017 22nd Asia and South Pacific Design Automation Conference (asp-dac)*, pages 200–205, Chiba, Japan, 2017. IEEE.

[17] G. Wu, J. Sun, and J. Chen. A survey on the security of cyber-physical systems. *Control Theory and Technology*, 14(1):2–10, 2016.

[18] B. Genge, I. Nai Fovino, C. Siaterlis, and M. Masera. Analyzing cyber - physical attacks on networked industrial control systems. In Jonathan Butts and Sujeet Shenoi, editors, *Critical infrastructure protection v*, IFIP Advances in Information and Communication Technology, pages 167–183, Berlin, Heidelberg, 2011. Springer.

[19] R. Candell, T. Zimmerman, and K. Stouffer. *nist - ir 8089 an industrial control system cybersecurity performance testbed.* 2016.

[20] J. Kosturko, E. Schlieber, S. Futch, and S. Nielson. Cracking a continuous flow reactor : a vulnerability assessment for chemical additive manufacturing devices. In *2018 IEEE International Symposium on Technologies for Homeland Security (HST)*, pages 1–6, 2018.

[21] D. Lichte, K.-D. Wolf, and K.-D. Wolf. Use case-based consideration of safety and security in cyber physical production systems applied to a collaborative robot system. *Safety and Reliability of Safe Societies in a Changing World*, 2018.

[22] A. Bracho, C. Saygin, H. Wan, Y. Lee, and A. Zarreh. A simulation-based platform for assessing the impact of cyber-threats on smart manufacturing systems. *Procedia Manufacturing*, 26:1116–1127, 2018.

[23] H. Orojloo and M. A. Azgomi. A method for evaluating the consequence propagation of security attacks in cyber-physical systems. *Future Generation Computer Systems*, 67:57–71, 2017.

[24] H. Turner, J. White, J. A. Camelio, C. Williams, B. Amos, and R. Parker. Bad parts : are our manufacturing systems at risk of silent cyberattacks ? *IEEE Security Privacy*, 13(3):40–47, 2015.

[25] A. Giehl, N. Wiedermann, and S. Plaga. A framework to assess impacts of cyber attacks in manufacturing. In *Proceedings of the 2019 11th international conference on computer and automation engineering*, ICCAE 2019, pages 127–132, Perth, WN, Australia, 2019. Association for computing machinery.

[26] A. Chattopadhyay, A. Prakash, and M. Shafique. Secure cyber - physical systems : current trends, tools and open research problems. In *Design, automation & test in Europe conference & exhibition (date), 2017*, pages 1104–1109, Lausanne, Switzerland, 2017. IEEE.

[27] A. E. Elhabashy, L. J. Wells, J. A. Camelio, and W. H. Woodall. A cyber-physical attack taxonomy for production systems: a quality control perspective. *Journal of Intelligent Manufacturing*, 2018.

[28] U. P. D. Ani, H. He, and A. Tiwari. Review of cybersecurity issues in industrial critical infrastructure: manufacturing in perspective. *Journal of Cyber Security Technology*, 1(1):32–74, 2017.

[29] K. V. Wong and A. Hernandez. A review of additive manufacturing. *ISRN Mechanical Engineering*, 2012:1–10, 2012.

[30] L. M. G. Graves, J. Lubell, W. King, and M. Yampolskiy. Characteristic aspects of additive manufacturing security from security awareness perspectives. *IEEE Access*, 7:103833–103853, 2019.

[31] T. A. Campbell and O. S. Ivanova. Additive manufacturing as a disruptive technology: implications of three-dimensional printing. *Technology & Innovation*, 15(1):67–79, 2013.

[32] P. K. Rao, J. Liu, D. Roberson, Z. Kong, and C. Williams. Online real - time quality monitoring in additive manufacturing processes using heterogeneous sensors. *Journal of Manufacturing Science and Engineering*, 137(6), 2015.

[33] A. Slaughter, M. Yampolskiy, M. Matthews, W. E. King, G. Guss, and Y. Elovici. How to ensure bad quality in metal additive manufacturing : in - situ infrared thermography from the security perspective. In *Proceedings of the 12th international conference on availability, reliability and security*, ARES '17, pages 78:1–78:10, New York, NY, USA, 2017. ACM.

[34] N. Gupta, A. Tiwari, S. T. S. Bukkapatnam, and R. Karri. Additive manufacturing cyber - physical system : supply chain cybersecurity and risks. *IEEE Access*, 8:47322–47333, 2020.

[35] M. Yampolskiy, W. E. King, J. Gatlin, S. Belikovetsky, A. Brown, A. Skjellum, and Y. Elovici. Security of additive manufacturing: attack taxonomy and survey. *Additive Manufacturing*, 21:431–457, 2018.

[36] M. Yampolskiy, T. R. Andel, J. T. McDonald, W. B. Glisson, and A. Yasinsac. Intellectual property protection in additive layer manufacturing : requirements for secure outsourcing. In *Proceedings of the 4th program protection and reverse engineering workshop*, PPREW-4, pages 7:1–7:9, New York, NY, USA, 2014. ACM.

[37] S. Moore, P. Armstrong, T. McDonald, and M. Yampolskiy. Vulnerability analysis of desktop 3d printer software. In *2016 resilience week (rws)*, pages 46–51, 2016.

[38] G. Pope and M. Yampolskiy. A hazard analysis technique for additive manufacturing. *Arxiv e-prints*, page arXiv:1706.00497, 2017.

[39] Z. DeSmit, A. E. Elhabashy, L. J. Wells, and J. A. Camelio. An approach to cyber-physical vulnerability assessment for intelligent manufacturing systems. *Journal of Manufacturing Systems*, 43:339–351, 2017.

[40] Q. Do, B. Martini, and K. R. Choo. A data exfiltration and remote exploitation attack on consumer 3D printers. *IEEE Transactions on Information Forensics and Security*, 11(10):2174–2186, October 2016.

[41] Z. Xu and Q. Zhu. Cross-layer secure cyber-physical control system design for networked 3d printers. In *2016 American Control Conference ACC*, pages 1191–1196, 2016.

[42] A. Zarreh, C. Saygin, H. Wan, Y. Lee, and A. Bracho. A game theory based cybersecurity assessment model for advanced manufacturing systems. *Procedia Manufacturing*, 26:1255–1264, 2018.

[43] M. Wu and Y. B. Moon. Taxonomy of cross - domain attacks on cybermanufacturing system. *Procedia Computer Science*, 114:367–374, 2017.

[44] Z. Yu, L. Zhou, Z. Ma, and M. A. El-Meligy. Trustworthiness modeling and analysis of cyber -physical manufacturing systems. *IEEE Access*, 5:26076–26085, 2017.

[45] T. Johnston, T.D. Smith, and J.L. Irwin. Additive manufacturing in 2040 powerful enabler. *Disruptive Threat, RAND Corporation*, page 31, 2018.

[46] J. Gatlin, S. Belikovetsky, Y. Elovici, A. Skjellum, J. Lubell, P. Witherell, and M. Yampolskiy. Encryption is futile : reconstructing 3d - printed models using the power side - channel. In *24th international symposium on research in attacks, intrusions and defenses*, pages 135–147, San Sebastian Spain, 2021. ACM.

[47] W. Förster, T. Pucklitzsch, and D. Nickel. The influence of different infill structures on the mechanical properties in additive manufacturing. *Acc Journal*, 27(1):7–16, 2021.

[48] K. Zhu and Y. Zhang. A cyber - physical production system framework of smart cnc machining monitoring system. *IEEE/ASME Transactions on Mechatronics*, 23(6):2579–2586, 2018.

[49] M. Van Elsen. Complexity of selective laser melting : a new optimisation approach. 2007.

[50] J. N. Zalameda, E. R. Burke, R. A. Hafley, K. M. Taminger, C. S. Domack, A. Brewer, and R. E. Martin. Thermal imaging for assessment of electron-beam freeform fabrication (EBF3) additive manufacturing deposits. In *Thermosense: thermal infrared applications XXXV*, volume 8705, pages 174–181. SPIE, 2013.

[51] T. Hua, C. Jing, L. Xin, Z. Fengying, and H. Weidong. Research on molten pool temperature in the process of laser rapid forming. *Journal of Materials Processing Technology*, 198(1-3):454–462, 2008.

[52] S. Liu, W. Liu, M. Harooni, J. Ma, and R. Kovacevic. Real-time monitoring of laser hot-wire cladding of inconel 625. *Optics & Laser Technology*, 62:124–134, 2014.

[53] V. Carl. Monitoring system for the quality assessment in additive manufacturing. In *AIP Conference Proceedings 1650*, pages 171–176, Boise, Idaho, 2015.

[54] S. Berumen, F. Bechmann, S. Lindner, J. Kruth, and T. Craeghs. Quality control of laser- and powder bed-based additive manufacturing (AM) technologies. *Physics Procedia*, 5:617–622, 2010.

[55] E. Rodriguez, F. Medina, D. Espalin, C. Terrazas, D. Muse, C. Henry, E. MacDonald, and R. B. Wicker. Integration of a thermal imaging feedback control system in electron beam melting. In *2012 international solid freeform fabrication symposium*, page 17.

[56] S. Clijsters, T. Craeghs, S. Buls, K. Kempen, and J.P. Kruth. In situ quality control of the selective laser melting process using a high-speed, real-time melt pool monitoring system. *The International Journal of Advanced Manufacturing Technology*, 75:1089–1101, 2014.

[57] J. Schwerdtfeger, R. F. Singer, and C. Körner. In situ flaw detection by IR-imaging during electron beam melting. *Rapid Prototyping Journal*, 18(4):259–263, 2012.

[58] S. Price, J. Lydon, K. Cooper, and K. Chou. Experimental temperature analysis of powder-based electron beam additive manufacturing. In *2013 international solid freeform fabrication symposium*. University of Texas at Austin, 2013.

[59] S. Rokka Chhetri and M. A. Al Faruque. Side channels of cyber - physical systems : case study in additive manufacturing. *IEEE design test*, 34(4):18–25, 2017.

[60] S. Belikovetsky, M. Yampolskiy, J. Toh, J. Gatlin, and Y. Elovici. Dr0wned cyber - physical attack with additive manufacturing. In *11th \${\$usenix\$}\$ workshop on offensive technologies (\${\$woot\$}\$ 17)*, 2017.

[61] S. Belikovetsky, Y. Solewicz, M. Yampolskiy, J. Toh, and Y. Elovici. Detecting cyber - physical attacks in additive manufacturing using digital audio signing. *Arxiv:1705.06454 [cs]*, 2017.

[62] H. Wu, Y. Wang, and Z. Yu. In situ monitoring of FDM machine condition via acoustic emission. *The International Journal of Advanced Manufacturing Technology*, 84(5):1483–1495, 2016.

[63] H. Wu, Z. Yu, and Y. Wang. Real-time fdm machine condition monitoring and diagnosis based on acoustic emission and hidden semi- markov model. *International Journal of Advanced Manufacturing Technology*, 90(5-8):2027–2036, 2017.

[64] S. R. Chhetri, A. Canedo, and M. A. A. Faruque. Confidentiality breach through acoustic side - channel in cyber - physical additive manufacturing systems. *ACM Transactions on Cyber-Physical Systems*, 2(1):1–25, 2017.

[65] M. A. A. Faruque, J. Wan, and S. R. Chhetri. Defending side channel attacks in additive manufacturing systems, 2019.

[66] Samuel B. Moore, Jacob Gatlin, Sofia Belikovetsky, Mark Yampolskiy, Wayne E. King, and Yuval Elovici. Power consumption -based detection of sabotage attacks in additive manufacturing. *Arxiv:1709.01822 [cs]*, 2017.

[67] M. A. Al Faruque, S. R. Chhetri, A. Canedo, and J. Wan. Acoustic side - channel attacks on additive manufacturing systems. In *2016 ACM/IEEE 7th international conference on cyber-physical systems (iccps)*, pages 1–10, Vienna, Austria, 2016. IEEE.

[68] M. A. Al Faruque, S. R. Chhetri, A Canedo, and J Wan. Forensics of thermal side-channel in additive manufacturing systems. *University of California, Irvine*, 12(13):176, 2016.

[69] C. Bayens, T. Le, L. Garcia, R. A. Beyah, M. Javanmard, and S. A Zonouz. See no evil, hear no evil, feel no evil, print no evil? malicious fill patterns detection in additive manufacturing. In *USENIX security symposium*, pages 1181–1198, 2017.

[70] L. Sturm, M. Albakri, C. B. Williams, and P. Tarazaga. In-situ detection of build defects in additive manufacturing via impedance-based monitoring. In *2016 International Solid Freeform Fabrication Symposium*. University of Texas at Austin, 2016.

[71] H. Vincent, L. Wells, P. Tarazaga, and J. Camelio. Trojan detection and side -channel analyses for cyber -security in cyber -physical manufacturing systems. *Procedia Manufacturing*, 1:77–85, 2015.

[72] M. Wu, Z. Song, and Y. B. Moon. Detecting cyber-physical attacks in cybermanufacturing systems with machine learning methods. *Journal of Intelligent Manufacturing*, 30(3):1111–1123, 2019.

[73] J. Straub. An approach to detecting deliberately introduced defects and micro-defects in 3d printed objects. In *Pattern recognition and tracking XXVIII*, volume 10203, page 102030L. International society for optics and photonics, 2017.

[74] R. F. Babiceanu and R. Seker. Big data and virtualization for manufacturing cyber-physical systems: a survey of the current status and future outlook. *Computers in Industry*, 81:128–137, 2016.

[75] B. Cambou, M. Gowanlock, J. Heynssens, S. Jain, C. Philabaum, D. Booher, I. Burke, J. Garrard, D. Telesca, and L. Njilla. Securing additive manufacturing with blockchains and distributed physically unclonable functions. *Cryptography*, 4(2):17, 2020.

[76] E. C. Balta, D. M. Tilbury, and K. Barton. A digital twin framework for performance monitoring and anomaly detection in fused deposition modeling. In *2019 IEEE 15th International Conference on Automation Science and Engineering (CASE)*, pages 823–829, 2019.

[77] S. Kurpjuweit, C. G. Schmidt, M. Klöckner, and S. M. Wagner. Blockchain in additive manufacturing and its impact on supply chains. *Journal of Business Logistics*, 42(1):46–70, 2021.

[78] C. Mandolla, A. M. Petruzzelli, G. Percoco, and A. Urbinati. Building a digital twin for additive manufacturing through the exploitation of blockchain: a case analysis of the aircraft industry. *Computers in Industry*, 109:134–152, 2019.

[79] X. Zhu. *Consensus- oriented cloud additive manufacturing based on blockchain technology : an exploratory study on system operation efficiency and security*. PhD thesis, University of Cincinnati, 2020.

[80] M. Holland, C. Nigischer, and J. Stjepandic. *Copyright protection in additive manufacturing with blockchain approach*. 2017.

[81] J. Lee, B. Bagheri, and H. Kao. A cyber - physical systems architecture for industry 4.0-based manufacturing systems. *Manufacturing Letters*, 3:18–23, 2015.

[82] M. Linares, N. Aswani, G. Mac, C. Jin, F. Chen, N. Gupta, and R. Karri. hack3d : evaluating cybersecurity of additive manufacturing by crowdsourcing. *Arxiv:2005.04368 [cs]*, 2020.

[83] O. Ivanova, A. Elliott, T. Campbell, and C.B. Williams. Unclonable security features for additive manufacturing. *Additive manufacturing*, 1-4:24–31, 2014.

[84] S. Binard and L. Philips. *Watermarking for additive manufacturing copy control by roughness modification*. PhD thesis, 2018.

[85] M. H.s Rais, Y. Li, and I. Ahmed. Spatiotemporal g-code modeling for secure fdm-based 3d printing. In *Proceedings of the ACM/IEEE 12th International Conference on Cyber-Physical Systems*, pages 177–186, 2021.

[86] S. Yu, A. V. Malawade, S. R. Chhetri, and M. A. Al Faruque. Sabotage attack detection for additive manufacturing systems. *IEEE Access*, 8:27218–27231, 2020.

[87] lulzbot taz 6. `https://lulzbot.com/store/taz-6`. Accessed on 19 October, 2022.

[88] Nema 17 standard hybrid stepper motors. `https://tinyurl.com/vr6xhk9c`. Accessed on October 19, 2022.

[89] J. Gatlin, S. Belikovetsky, S. B. Moore, Y. Solewicz, Y. Elovici, and M. Yampolskiy. Detecting sabotage attacks in additive manufacturing using actuator power signatures. *IEEE Access*, 7:133421–133432, 2019.

[90] Stéphane Mallat. *A wavelet tour of signal processing*. Elsevier, 1999.

[91] Michel Misiti, Yves Misiti, Georges Oppenheim, and Jean-Michel Poggi. *Wavelets and their Applications*. John Wiley & Sons, 2013.

[92] M. Müller. Dynamic time warping. *Information Retrieval for Music and Motion*, pages 69–84, 2007.